Emile Guélard-Ancilotti

Morphodynamics of the Cacela inlet and ebb-tidal delta based on Sentinel 2 images

UNIVERSIDADE DO ALGARVE

FACULDADE DE CIÊNCIAS E TECNOLOGIA

2021

Emile Guélard-Ancilotti

Morphodynamics of the Cacela inlet and ebb-tidal delta based on Sentinel 2 images

Master in Marine and Coastal Systems

Work performed under the supersion of :

Erwan Garel (Universidade do Algarve | UALG · Centro de Investigação Marinha e Ambiental (CIMA))

Óscar Ferreira (Universidade do Algarve | UALG · Centro de Investigação Marinha e Ambiental (CIMA))

UNIVERSIDADE DO ALGARVE

FACULDADE DE CIÊNCIAS E TECNOLOGIA

2021

Morphodynamics of the Cacela inlet and ebb-tidal delta based on Sentinel 2 images

---

Declaração de autoria de trabalho

Declaro ser o autor deste trabalho, que é original e inédito. Autores e trabalhos consultados estão devidamente citados no texto e constam da listagem de referências incluída.

Declaration of authorship of work

I declare to be the author of this work, which is original and unpublished. Authors and works consulted are duly cited in the text and are included in the list of references.

Acknowledgments

First of all, I would like to express my sincere gratitude to my two master thesis supervisors Erwan Garel and Oscar Ferreira. They gave me great support and answered to the different problems I encountered with this topic with great care. I would like to thank them for their patience, their honesty and the last-minute corrections they were able to give me despite their busy schedule. I really felt supported regarding my work during this semester despite my novice knowledge in the field and the fact that we were in distance for most of the time. Their knowledge and comments allowed me to learn a lot about their specialties and greatly improved my scientific method.

I would also like to thank my professors from the Marine and Coastal Systems master's program for their support throughout my training. They always answered my questions and helped me to improve my multidisciplinary knowledge in marine sciences and my scientific methodology.

I thank the members of the Universidade do Algarve for their availability and for the chance to publish this thesis.

I thank the Copernicus program for providing me with the Sentinel-2 images, the GUADELTA program for their tidal data and the state-owned company Puertos del Estado for their wave data.

I thank my family for their constant support and their confidence in my abilities. They have always supported me in my desire to go further and do what I love most. Special attention to Sonia, Jean, Sophie, Félix, Eliott, Justine, Julia, Matthieu, Louis and little Maurice.

Then I would like to thank my friends in Paris for their long-distance support and my friends in Faro for their generosity and presence. A special attention to my friends Anicet, Gabrielle and Marius who followed me in this incredible experience and Alexandre and Ruben who joined it, to whom I show a huge affection and gratitude. Finally, I would like to fully thank my people from Praia do Faro and Briscolina who offered me a huge support, many memories and good vibes.

Abstract

The main objective of this master thesis was to investigate and comprehend the short-term morphologic evolution of Cacela Inlet and ebb-tidal delta, based on Sentinel-2 satellite imagery from September 2015 to September 2020. The different observations made on Cacela inlet and ebb-tidal delta were analyzed and possibly related with computed waves data from SIMAR numerical model in order to observe the influence of prevailing hydrodynamic conditions that can act on it. Through the analysis of its barriers, inlet and ebb tidal delta features morphology and morphodynamics, this study produced a first morphological characterization of the system. Indeed, regarding its general observed morphology, it was characterized as a system with mixed energy influences showing characteristic morphological features produced by both tidal currents (e.g., almost constant well developed margin linear bars) and wave forcing (e.g., swash bars and ebb-tidal delta asymmetry). Moreover, the inlet evolution was related to the barriers morphodynamics, which was strongly influenced by the ebb delta shoals/channel behaviors. Those barriers showed quite unbalanced evolutions due to the shoals preferential welding to the downdrift barrier, and to an updrift barrier more exposed to the waves. Those processes were mostly governed by the combination of eastward longshore drift and mixed waves origins influence. However, the large and unusual morphological variability observed at Cacela ebb tidal delta was hardly related to wave activity, except for some large storm events. Among these, the Emma storm stands out as it was considered to have initiated or aided the present inlet position stability by straightening and shifting the unstable arcuate channel at the center of Cacela Inlet. This stability contrasts with Lacém Inlet's (previous inlet separating Cabanas Island from Cacela Peninsula until its artificial closure and relocation through the opening of Cacela Inlet in 2011) that showed high (downdrift) migration, thus indicating successful inlet management.

Keywords: Inlet, Ebb-tidal delta, Morphodynamics, Shoals, Ebb channel, Cacela-Cabanas system, Hydrodynamics, Sentinel-2

Resumo

O delta de Cacela ebb-tidal, que é a frente a céu aberto da enseada de Cacela, a enseada mais a leste da lagoa da Ria Formosa, situa-se em frente de Cacela Velha no Algarve (Portugal). Esta enseada é bastante recente, pois foi aberta artificialmente em 2011 após o encerramento da instável Enseada Lacém (anteriormente em frente de Fábrica). A dinâmica desta última foi relativamente bem documentada, antes do seu encerramento em 2011, com base em vários estudos sobre a sua evolução a longo prazo. No entanto, não há informação sobre a evolução morfológica da Enseada de Cacela, bem como sobre o seu delta de refluxo desde a sua abertura, incluindo a sua resposta a eventos energéticos. Assim, o principal objectivo desta tese de mestrado foi investigar e compreender a evolução morfológica a curto prazo da Enseada de Cacela e do delta da maré baixa, com base em imagens de satélite Sentinel-2 de Setembro de 2015 a Setembro de 2020. As diferentes observações feitas sobre a entrada de Cacela e o delta da maré baixa foram analisadas e possivelmente relacionadas com dados de ondas computorizadas do modelo numérico SIMAR, a fim de observar a influência das condições hidrodinâmicas prevalecentes que podem actuar sobre ela. Para esse efeito, a morfologia e morfodinâmica deste sistema foram investigadas utilizando as características gerais e deslocamentos horizontais das suas características morfológicas (por exemplo, cardumes, canais e barreiras) visíveis nas imagens durante períodos (meses) de curto prazo. Duas imagens por ano (cerca de cada 6 meses) foram analisadas em Março e Setembro para verificar as características morfológicas gerais dos cardumes e as alterações e revelar possíveis sazonalidades. Além disso, o intervalo de tempo entre as imagens foi reduzido (por exemplo, uma imagem quase de 2 em 2 meses) para acompanhar as alterações morfológicas de curto prazo observadas no intervalo de 6 meses. As características morfológicas do sistema foram anotadas no QGIS para todas as imagens utilizadas (apêndice 1) através de linhas digitalizadas ou posições referenciadas, e foram desenhados diagramas estruturais no QGIS para imagens com intervalo de 6 meses. Esta abordagem permitiu investigar como as condições de ondas de curto prazo e os eventos energéticos (por exemplo, ocorrência de ondas/tempestades orientais ou ocidentais, condições de ondas baixas, períodos altamente energéticos, etc.) estão relacionados com as alterações morfológicas observadas. A evolução morfol ógica do sistema foi então comparada com o

ambiente marinho local, principalmente no que diz respeito à potência das ondas e ao seu maior ângulo de incidência, e a eventos energéticos que poderiam ter influenciado a entrada e a morfologia do delta de maré baixa. Quanto aos resultados, embora este sistema tenha mostrado uma grande variabilidade que não foi descrita noutros deltas de maré baixa (frequentemente maiores), a entrada de Cacela e o delta de maré baixa foram definidos como um sistema com influências energéticas mistas, mostrando características morfológicas características produzidas tanto pelas correntes de maré como pela força das ondas. A sua morfologia geral apresentou um delta de maré baixa quase constantemente composto por barras lineares de margem de canal bem desenvolvidas testemunhando a influência das marés no sistema. Essas barras faziam fronteira com um canal de refluxo principalmente orientado N-S na sua parte superior (terra) e desviado na sua parte inferior (maré) (principalmente NW-SE com uma importante variabilidade das orientações W-E para NE-SW). A influência das ondas foi principalmente expressa por uma assimetria geral no delta de maré baixa composta por barras oscilantes bem desenvolvidas que se formam, agregam e fundem com a barreira de direcção descendente em quase um ano. Esta assimetria, bem como a morfodinâmica dos cardumes, foi explicada pela combinação da deriva de longo curso para leste e da potência normalizada (Pch) das ondas orientais, maior do que para oeste, que também atingem a costa mais frontalmente do que as ondas ocidentais (devido à orientação da linha costeira NE-SW). Foi observada uma sazonalidade de ondas consistente com o desenvolvimento de cardumes grandes e dinâmicos no Inverno devido à influência das ondas; no Verão, estes cardumes estavam mais dispersos no Verão devido ao domínio das marés sob condições de ondas baixas. A posição da parte mais baixa (para o mar) do canal de refluxo principal roda significativamente no sentido horário e anti-horário durante períodos de 2 a 6 meses, à semelhança dos modelos de "desvio de sedimentos" e de "entrada estável" do FitzGerald (2000). A evolução da entrada estava relacionada com a morfodinâmica das barreiras, que é fortemente influenciada pelo comportamento dos cardumes/canais de delta de refluxo. De facto, mostrou uma migração geral para baixo e para terra dentro da bacia da barreira traseira sob a combinação de condições de grandes ondas do Sudeste e do Sudoeste que favorece a soldadura das barras. Inversamente, a sua posição desloca-se à deriva e para o mar em condições de ondas baixas ou quando o canal de refluxo foi inclinado dentro da entrada. Este canal inclinado

foi observado após a tempestade oriental de Abril de 2017, que levou a um longo período de erosão do escarro da barreira de corrente de ar. Depois, o canal endireitou-se e deslocou-se para o centro da entrada larga, devido à tempestade ocidental de Março de 2018 (Emma, a maior tempestade durante o período de estudo). Esta deslocalização natural pareceu ter estabilizado bastante o sistema, que não mostrou grandes alterações morfológicas desde então, incluindo a ocorrência de uma tempestade ocidental em Dezembro de 2019. A excepção é a parte inferior (para o mar) do canal que sofreu rotações mais contínuas e grandes, indicando que o sedimento continua a contornar de acordo com os modelos de "mudança de canal exterior" e "entrada estável". Globalmente, este estudo mostra que a grande e invulgar variabilidade morfológica do delta do refluxo de Cacela está dificilmente relacionada com a actividade das ondas, excepto no caso de alguns grandes eventos de tempestade. Entre estes, a tempestade Emma mantém-se tal como desencadeou ou promoveu a estabilidade actualmente observada da posição de entrada. Esta estabilidade contrasta com a alta (downdrift) migração da entrada de Lacém (a antiga entrada de Cacela antes da sua deslocalização artificial em 2011), e indica uma gestão bem sucedida no que diz respeito à sustentabilidade da entrada. Em estudos futuros, a permanência da posição de entrada deve ser confirmada, e a morfodinâmica do delta do refluxo deve ser avaliada com base em dados adicionais (imagens de satélite, fotografias aéreas, batimetria) um curto intervalo de tempo (todos os meses, por exemplo).

Palavras-chave: Enseada, Delta de maré baixa, Morfodinâmica, Cardumes, Canal de maré baixa, Sistema Cacela-Cabanas, Hidrodinâmica, Sentinel-2

Table of content

List of Figures

List of tables

List of appendices

List of abbreviations and symbols

N : North
E : East
W : West
S : South
Hs : Significant wave height
Tp : Spectral peak period
Θ : Mean direction at peak period
P : Wave power
Pc : Cumulative wave power
Pch : Parameterized wave power

1. Introduction

1.1. Motivation

Tidal inlets are important dynamic systems making the junction between open ocean and back barrier sheltered basins, lagoons or estuaries. They represent key areas for the society as most of them are passages to harbors and permit important nutrients and sediments exchange, highly relevant for the ecology and environment (FitzGerald et al., 2011). Due to their position as a transition area along barrier coasts (or at estuary mouths), they act as feedback systems between the open sea and back barrier (or estuarine) area controlled by the sediment supply, tidal currents and open ocean waves (de Swart and Zimmerman, 2009). The combination of those two hydrodynamic forcings (tides and waves) along with sediment characteristics leads to complex morphodynamic processes governing the formation, maintenance and evolution of inlets and their associated deltas (Petti et al., 2020). Their morphology depends of the hydrodynamic energy that affects the system through time and often displays marked seasonal to decadal patterns that are punctuated by episodes such as storm events (particularly in winter). These energetic events may induce strong perturbations, such as inlet opening or closure, spit breaching, shoal formation or disappearance, closure of primary or secondary channels, etc. (Balouin et al., 2004). The definition and long-term evolution of those systems is well documented and it is known that they tend to return to dominant (pre-storm) morphological conditions after perturbations (when the latter are not too important to exceed the resilience capacity of the system and provoke irreversible changes). However, there is a lack of knowledge about their short-term evolution and post-storm transitional periods, mainly due to the lack of surveys with high temporal resolution (Balouin et al., 2004). This lack of observations makes it difficult to foresee their evolution (Zhang et al., 2020), while the possibility to foresee the morphological ones could be highly relevant for inlet/delta management.

The difficulty on obtaining high-resolution (time and space) monitoring can be minimized by the use of satellite imagery. Satellite imagery constitutes since several decades a good tool to detect coastal morphodynamic features such as coastlines, tidal flats and shallow water topography (Zhang et al., 2020), particularly thanks to the recent improvements in resolution. Since the first record of Landsat images in the 70's, satellite imagery has well developed, increasing its spatial,

temporal, and spectral resolutions (Zhang et al., 2020). Moreover, open data policies developed for remote sensing in United States, Europe and China during the last decade allowed a significant progress in Earth observation and application. The observation and assessment of coastlines (Li and Gong, 2016), salt marsh vegetation (Sun et al., 2018), and coastal aquaculture (Stiller et al., 2019) amongst others were assessed in recent studies thanks to satellite band description. Multiple satellite images allow dense time-series analysis, and have proven to be valuable for the observation and analysis of the long-term changes that occur in coastal zones (Zhang et al., 2020). Satellite imagery offers scientists and coastal engineers' key information to understand detailed large spatial-scale coastal processes, allowing coastal risk prevention (Bergsma and Almar, 2020). Sentinel 2 multi spectral images from the European Copernicus program provide a particularly capable to support morphodynamic studies as they have a wide-swath (290 km width), high-resolution (10 m at best) and a high revisit time (2-3 days at mid-latitudes) (Copernicus.eu).

Nowadays, the management of inlets is no longer limited to the maintenance of channels for navigation, but faces new challenges, such as the stability of coastlines adjacent to the mouths, the renewal and quality of water for aquaculture and the development of touristic activities (Bertin, 2015). The stability, evolution and resilience of inlets are important parameters in coastal management that need to be monitored by coastal practitioners for the environment sustainability and to understand their interaction with surrounding human structures and interventions (Hayes and FitzGerald, 2013).

Cacela ebb-tidal delta, which is the open-ocean front of the Cacela Inlet, the most eastward inlet of the Ria Formosa lagoon, is located in front of Cacela Velha in Algarve (Portugal)(Figure 1.1). This lagoon counts a high variety of diverse habitats (e.g., dunes, salt-mashes, tidal flats…) as well as many anthropogenic activities (e.g., tourism, fisheries, clam harvesting…) making it an important ecological and socio-economic zone of interest subject to important monitoring and managements. As a part of those managements, the Cacela Inlet was artificially opened in 2011 after the closure of the unstable Lacém Inlet (previously in front of Fábrica). The latter's dynamics were relatively well documented, prior to its closure in 2011, based on several studies about its long-term evolution (Vila-Concejo et al., 2002 & 2006; Ferreira et al., 2016; Kombiadou et al., 2018 & 2019). They show that the inlet was prone to important variability in width and migration

rates (Kombiadou et al., 2019). However, there is no information about the morphological evolution of the Cacela Inlet as well as its ebb-tidal delta since its opening, including its response to energetic events.

Figure 1.1 - Photography of the Cacela Inlet in front of the ramparts of Cacela Velha

1.2. Objectives

The main objective of this master thesis was to investigate and comprehend the short-term morphologic evolution of Cacela Inlet and ebb-tidal delta, from September 2015 to September 2020. To this end, the morphology and morphodynamics of this system were analyzed based on the general characteristics and horizontal displacements of its morphological features (e.g., shoals, channel and barriers) observed on Sentinel 2 imagery over the short-term (months). Then, the morphological evolution of the system was compared with the marine climate at the study area, and particularly with energetic events that could have induced major changes on the inlet morphology and ebb-tidal delta. The analysis aims at establishing the morphodynamic interactions between the inlet and ebb-tidal delta features and the morphodynamic response of the system to the prevailing hydrodynamic conditions.

The results of this thesis can be an essential source of information for future coastal planning and management in the study area, providing basic data about the inlet and ebb-tidal delta morphological variability and response to wave climate, including storms. In addition, this study can help to evaluate the success of the artificial opening of the inlet in 2011 through the evaluation of its stability compared to the previous Lacém inlet.

2. Literature review

2.1. General morphology and classification of tidal inlets and deltas

Tidal inlets and their associated deltas represent key environmental sub-systems keeping the dynamic equilibrium of the coastal system (Vila-Concejo et al., 2004). The high dynamics of those areas are induced by the combination of tidal prism, inlet geometry, wave and tidal energy, sediment supply, spatial distribution of back barrier channels, regional stratigraphy, slope of the nearshore, and engineering modifications (FitzGerald et al., 2000).

This combination of environmental conditions rules the direction and magnitude of sediment transport, leading to the erosion or deposition of the sediment that form the coastline and seabed morphology (deSwart and Zimmerman, 2009). Tidal inlets and deltas develop mobile sedimentary forms (e.g., small bedforms and shoals, large swash bars and bar complexes), facilitated by the unconsolidated structures of channel banks and the sand delivery to the inlet (FitzGerald et al., 2011). Their equilibrium state is related to the framework geology of the region and littoral sediment transport trends (FitzGerald et al., 2011).

Most of the time, inlets sides are recurved ridges of sand spits generated from sediment transport to the back barrier by refracted waves and flood-tidal currents (FitzGerald et al., 2011). Constricted to the quite narrow and deep inlet, tidal currents maintain inlet channel, flowing fast at the minimum channel width and losing their velocity and capacity to transport sediment when they cross inlet mouth (Fisher and Simpson, 1982; FitzGerald, 2005). Thus, sediments are removed from the channel floor and accumulated on shoals seaward and landward of the inlet throat mostly according to the tidal regime, respectively ebb and flood dominated (as represented in yellow in Figure 2.1) (Boothroyd, 1985; FitzGerald et al., 2011). Ebb-tidal delta shoals are formed by ebb-tidal currents, fed mostly by littoral transport and modified by wave action, while flood-tidal delta shoals are shaped by flood-tidal currents (Boothroyd, 1985).

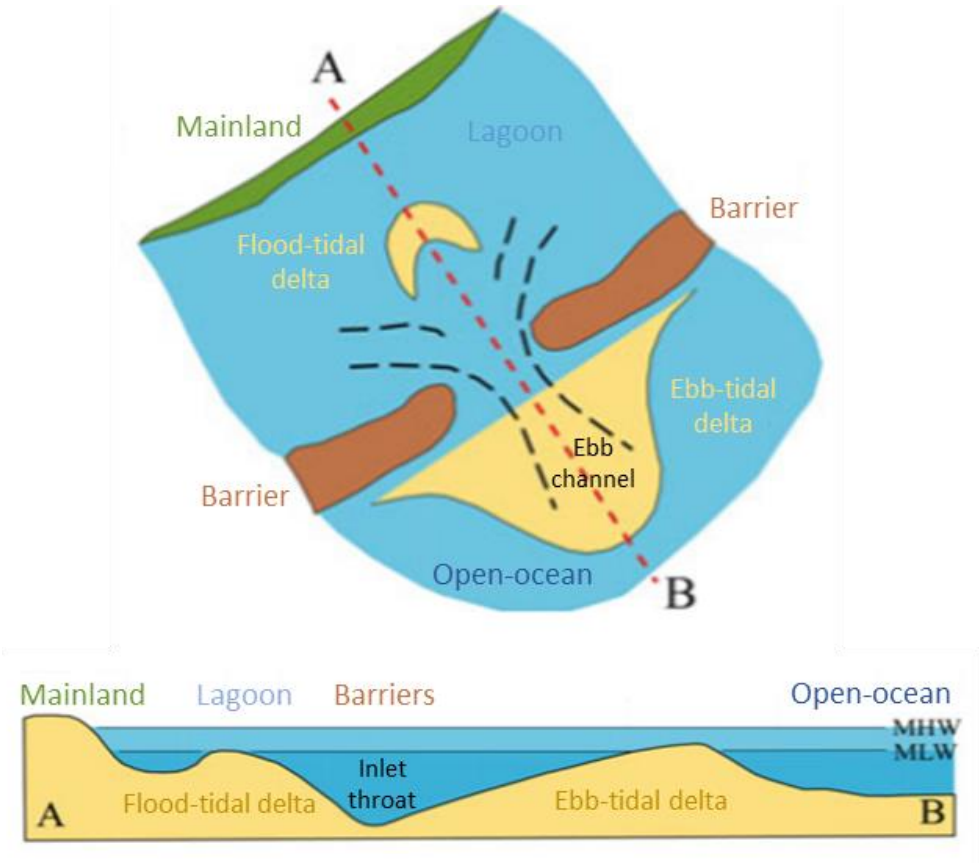

Figure 2.1 - Inlet general morphology with its associated cross-section (adapted from FitzGerald et al., 2011)

Davis and Hayes (1984) founded that the tidal prism, which represents the volume of water that flows through the inlet during the tidal flood (or ebb), has the most important hydrodynamic control on the delta. An increase in tidal range increases the tidal prism leading to the increase of tidal current velocities due to the larger volume of water that must pass through the inlet in the same time period (Boothroyd, 1985).

Several authors (Davies, 1964; Hayes, 1975; Hayes, 1979; Davis and Hayes, 1984; Gibeaut and Davis, 1991) proposed an inlet classification in three main groups according to the dominant energy (tide-dominated, mixed or wave-dominated inlets). Different morphologies are characteristic of those dominant energy and inlet type (as represented in Figure 2.2), such as aligned barriers and extended ebb-tidal delta shoals for tide-dominated inlets, offset barriers, very small ebb-tidal delta shoals and large flood-tidal delta shoals for wave-dominated inlets, and variable features for mixed-energy inlets (Davis, 2013; Kraus, 2009).

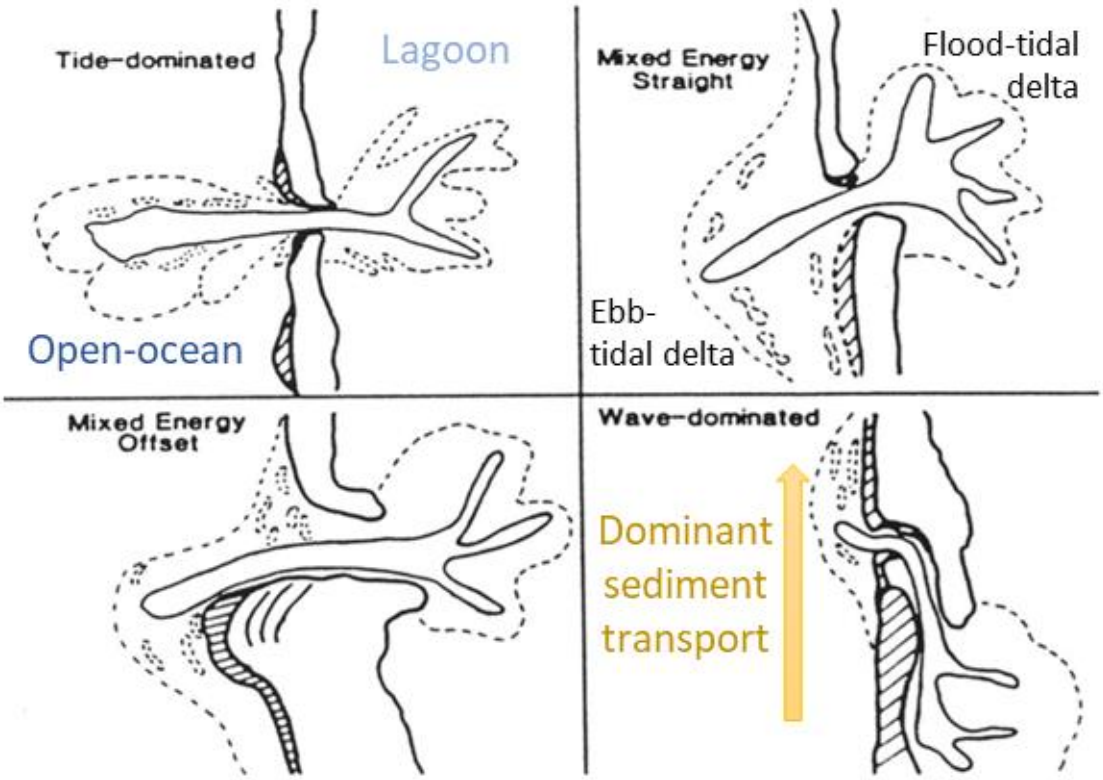

Figure 2.2 - Inlet classification and respective morphologies (adapted from Gibeaut and Davis, 1991)(dashed lines: flood- and ebb-tidal delta extensions and shoals, solid lines: barriers and main channel limits, dashed area: parts of the barriers submitted to larger erosional processes)

2.2. Ebb-tidal deltas morphodynamics

Ebb-tidal deltas are important shoal complexes crossed by tidal channels on the open ocean side of the inlet (FitzGerald et al., 2011). As they constitute the forehead of tidal inlets, they are formed by the combination of nonlinear interactions between waves, tides, sediment supply and possible riverine discharge. The major factors appearing to control the shape of the ebb-tidal deltas investigated by Hicks and Hume (1996) were the tidal prism, shoreline configuration and wave energy. Strong tidal forcing contributes to extend ebb-tidal deltas offshore through the development of several shoals with a lobe shape, crossed by channels; moderate ones form a single shore-normal channel flanked by crescent bars (Styles et al., 2016). Ebb shoals asymmetry (in plan view) results from the larger sand accumulation on the downdrift side rather than updrift side of the inlet due to the predominance of the longshore transport in one direction, deflecting the main ebb channel (FitzGerald et al., 2011; Styles et al., 2016) as represented on the wave-dominated system of the low-right corner of Figure 2.2.

Although ebb-tidal deltas can show various morphologies, they generally present the following features listed by FitzGerald et al. (2011) as below, and represented schematically in Figure 2.3.

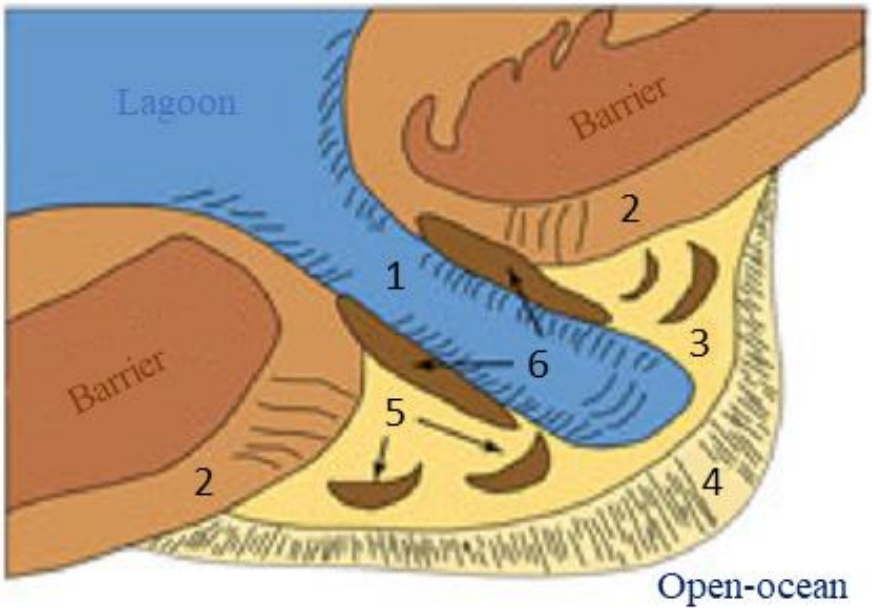

Figure 2.3 - General morphology of an ebb-tidal delta (adapted from FitzGerald et al. 2011) (numbers corresponding to the different morphologies described at the text: 1. Ebb channel, 2. Marginal-flood channels, 3. Swash platform, 4. Terminal lobe, 5. Swash bars and 6. Channel margin linear bars)

1. **Ebb channel**: seaward major channel dominated by ebb-tidal currents and digging in the ebb-tidal delta sand. Levee-like deposits are formed on its flanks due to the interaction between tidal and wave-generated currents.

2. **Marginal-flood channels**: shallow channels dominated by flood-tidal currents located between the channel margin linear bars, the adjacent updrift and downdrift beaches.

3. **Swash platform**: broad shallow sand platform dominated by wave action located on the flanks of the main ebb channel, defining the general extent and symmetry of the ebb-tidal delta.

4. **Terminal lobe** or **outer shoal**: a lobe of sand forming a relatively steep seaward-slope created by sediment from the main ebb channel and by littoral drift (from the updrift beach) transported through the updrift lateral bars. This area thus results from the interaction of both tidal currents and waves. Breaking waves, during storms or important wave swell at low tide, limit the growth of the terminal lobe.

5. **Swash bars**: arcuate-shaped swash bars (around 50-150 m long, 50 m wide, and 0.5-2.0 m in height) that migrate onshore due to waves breaking over the terminal lobe and across the swash platform.

6. **Channel margin linear bars**: low-tide exposed bars that border the main ebb channel and form atop the swash platform, confining the ebb flow.

Acting as important sand sinks and sources, ebb-tidal deltas intercept sediments transported by longshore transport, which are carried seaward by ebb-tidal currents where they deposit. Ebb-tidal deltas constitute primary pathways for terrestrial sediments to the ocean and to downdrift areas (FitzGerald et al., 2011). Thus, they represent major dynamic elements of the littoral sediment budget that can strongly influence surrounding coastal processes (e.g., bypassing of littoral drift and partial wave sheltering of the adjacent shore) (Hicks and Hume, 1996) and disrupt longshore transport pathways with growth, migration and erosion of adjacent shorelines (Styles et al., 2016).

Tide-dominated inlets tend to have larger and extended ebb shoals that include channel margin linear bars parallel to the inlet lateral borders (Davis, 2013; Kraus, 2009). They can be characterized by a sand tidal bypass (Figure 2.4), in which the sediment enters the upstream side of the channel during flood tide and a portion eventually returns downstream during ebb tide (Kraus, 2009). Moreover, break off and onshore migration of portions of the channel margin bars or other features of the ebb shoal can happen during storms (Kraus, 2009).

Wave-dominated inlets tend to have very small ebb shoals (Davis, 2013). Their morphology is dominated by the terminal lobe, a semi-circular ebb shoal parallel to the coast that rings the delta (Figure 2.4) (Kraus, 2009). Sediment is mainly bypassed along the terminal lobe by longshore currents generated by waves breaking on it (Kraus, 2009).

Mixed-energy inlets share the characteristics of the tide and wave dominated inlets with a distinct terminal lobe and some channel-margin linear bars on the ebb-tidal delta (Figure 2.4).

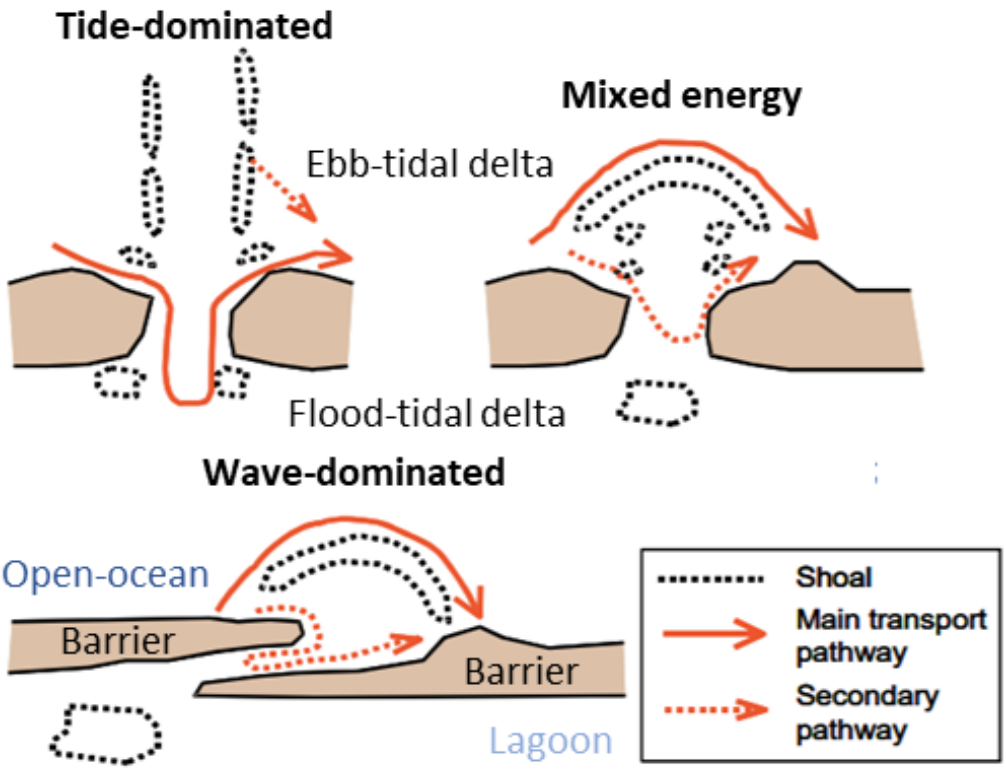

Figure 2.4 - Bypassing dynamics of tidal inlets according to their energy dominance (adapted from Kraus, 2009)

Tidal inlets and their associated ebb-tidal deltas undergo different cyclic behaviors regarding sediment bypassing. FitzGerald (2000) defined several models to describe those mechanisms, including 6 inlets behaviors without artificial jetties (Figure 2.5).

MODEL 1 - INLET MIGRATION AND SPIT BREACHING: The model describes inlets migrate in a dominant longshore drift direction due to updrift spit accretion until the ebb channel becomes hydraulically inefficient and unstable. Then, the updrift barrier breaches and the old inlet fills up, providing a more direct exchange of water between the ocean and basin.

MODEL 2 - STABLE INLET PROCESSES: It presents a system with a main channel and throat at a fixed (stable) position. Swash bars form on the banks of the ebb channel, migrate and coalesce landward due to wave action and finally weld (attach) to the barriers over periods between 4 and 10 years. Moreover, when the inlet increases in size, the size of the shoals and the volume of sand transported onshore often increase.

MODEL 3 - EBB-TIDAL DELTA BREACHING: It concerns a throat that is fixed but a main ebb channel that is progressively, cyclically (6 to 12 months) or catastrophically (storm event) deflected downdrift with shoals migrating landward and downdrift due to wave driven transport. Channel margin linear bars are bisected through a spill-over channel that becomes the main channel when the old one is too unstable and inefficient. Swash bars coalesce particularly downdrift, forming important bars welding with the downdrift barrier. The entire cycle occurs usually over 4 to 10 years.

MODEL 4 - OUTER CHANNEL SHIFTING: It shows a process similar to ebb-tidal delta breaching (model 3) except that the deflection occurs on the outer part of the ebb-tidal delta over comparatively shorter time periods and with smaller shoals migrating toward the downdrift barrier.

MODEL 5 - SPIT PLATFORM BREACHING: It is similar to inlet migration and spit breaching model (model 1) except for the breaching of the spit and swash platform (over a period of 1 to 2 years).

MODEL 6 - WAVE-DOMINATED INLETS: It concerns wave dominated inlets, where the majority of sediment transport occurs around the perimeter of the flattened ebb-tidal delta. Those inlets are often unstable requiring channel dredging and engineering structures to maintain the opening.

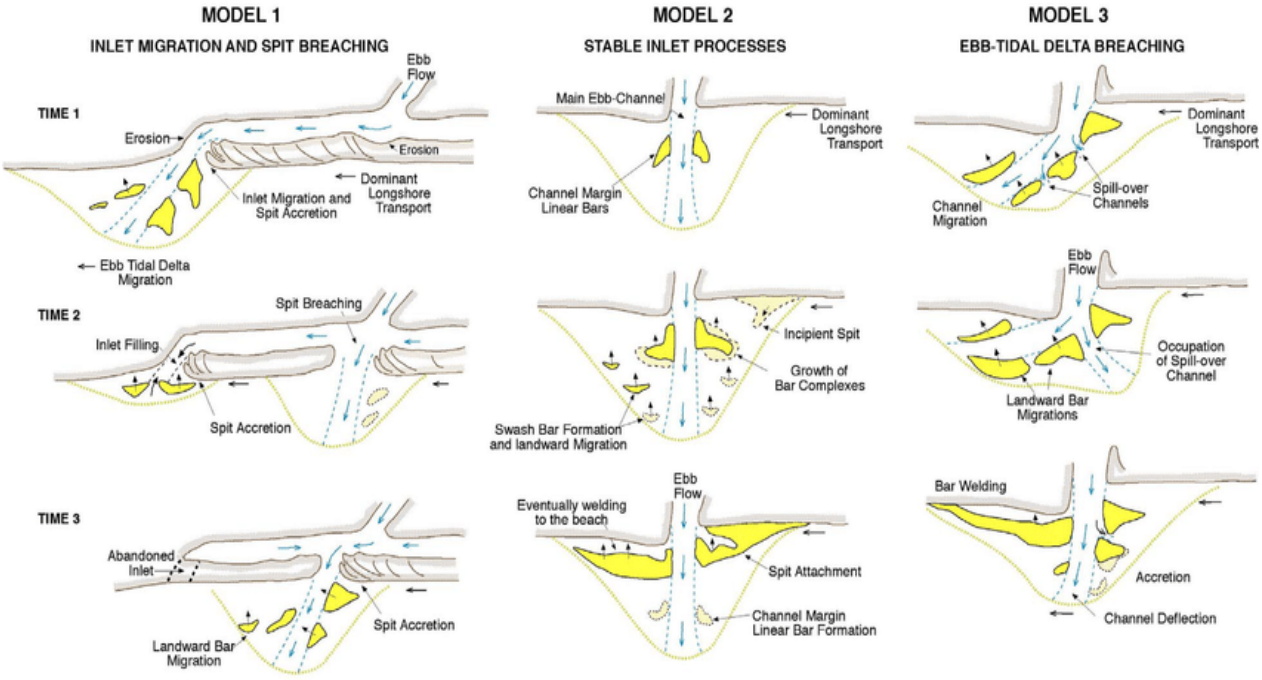

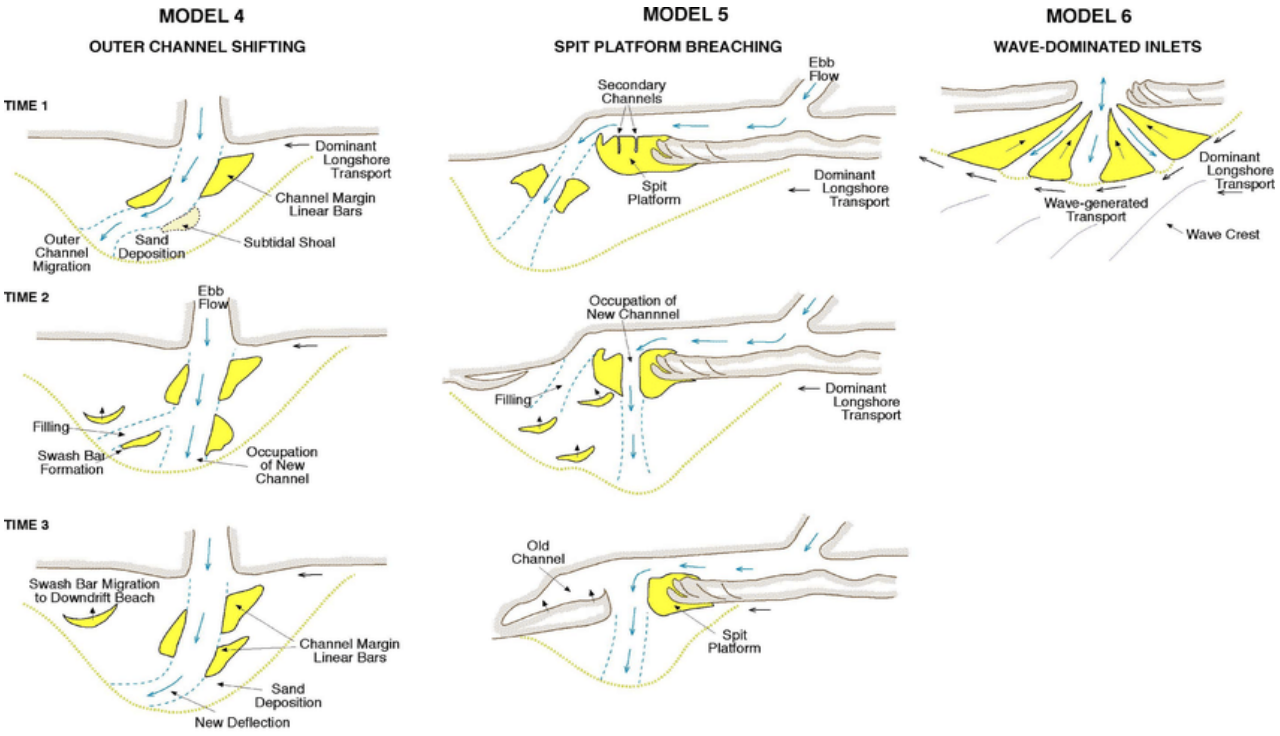

Figure 2.5 - Sediment natural bypassing conceptual models at tidal inlets (FitzGerald, 2000)(grey border : shoreline, yellow areas : underwater sand bodies, blue arrows : ebb flows)

2.3. Cacela-Cabanas system in the Ria Formosa

The Ria Formosa is a multi-inlet barrier islands lagoon system (Figure 2.6) extending over 50 km along the southeastern coast of Portugal. It is composed of two peninsulas, five islands, six tidal inlets and a large back barrier system (8.4×10^7 m^2). As it is strongly influenced by tidal inlets dynamics, Ria Formosa system undergoes various changes on barriers erosion/accretion, onshore sediment transport, barrier islands length, location of tidal flats and salt-marshes, and lagoon current patterns and velocities (Ferreira et al., 2016). By extension, those changes impact navigation routes and accessibility, shell farming location and viability, and houses maintenance/destruction (Ferreira et al., 2016).

This mesotidal system is submitted to semidiurnal tides with ranges between 2.8 m and 1.3 m for mean spring and neap tides, respectively, with a mean of 2.5 m and a maximum of 3.5 m (Ferreira et al., 2016). Waves are of moderate energy and show a mean annual significant wave height (Hs) of about 1 m and a peak period of 8.2 s (Costa et al., 2001).

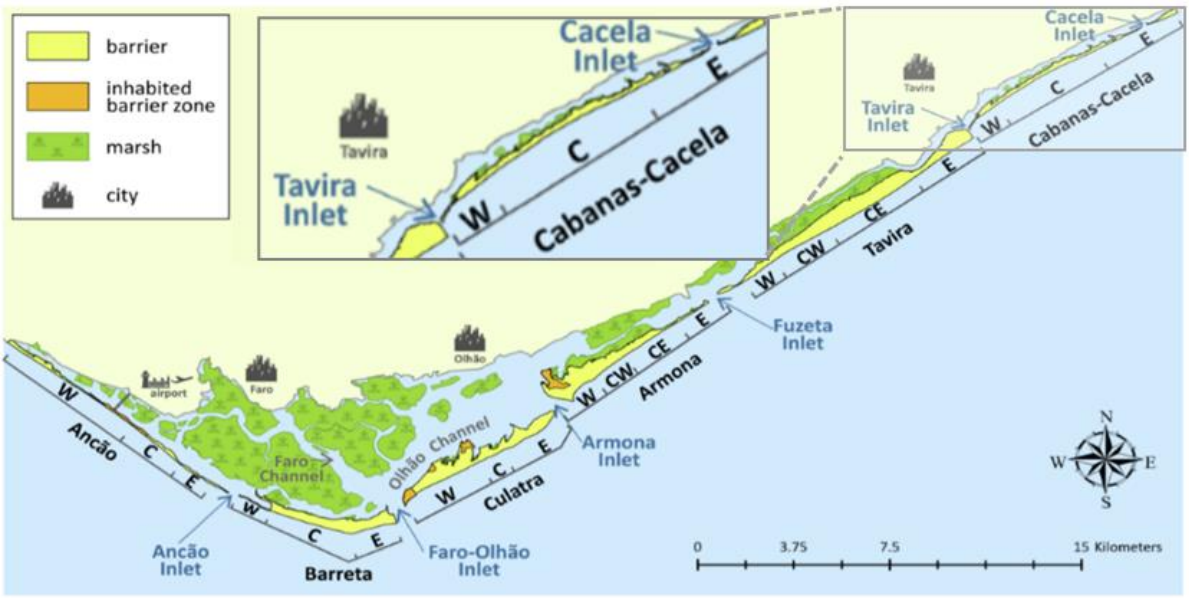

Figure 2.6 - General map of the multiple barrier island system of the Ria Formosa lagoon (adapted from Kombiadou et al., 2020)

The system flanks are subjected to dominant W-SW incident waves (about 71% of the swell occurrence) from Atlantic Ocean and E-SE incident waves (23% occurrence) generally generated by Eastern wind events called Levante (Costa, 1994; Costa et al., 2001). Due to their orientation and the shape of the barrier system, the long eastern flank is more protected from W-SW incident waves while the shorter western flank is more protected from E-SE incident waves. Storms, defined by Pessanha and Pires (1981) as events where offshore Hs are greater than 3 m (or 2.5 m according to Almeida et al., 2012, and Oliveira et al., 2018) on this area and linked to 2% of the offshore wave climate regime, show a general persistence of 2 to 5 days and typical Hs values between 3 m and 5 m (Costa et al., 2001). Moreover, as for dominant waves, SW storms are more energetic than SE ones for the same return period (Pires, 1998). Southwest storm events concentrate between October and March, while southeast storms occur more typically between December and March. Those periods present highest average number of storms per month of 1.17 for SW and 0.67 for SE events (Oliveira et al, 2018). Dominant wave conditions produce general west to east longshore currents and littoral drift (Ferreira et al., 2016). The Ria Formosa system receives limited terrestrial sediments input and riverine outflows due to rare precipitations episodes in the region and few rivers (Kombiadou et al., 2019).

The Cacela Inlet separates the Cacela Peninsula and Cabanas Island. Prior to the Cacela Inlet artificial opening (in 2011), this limit was constituted by Lacém Inlet, which is closed now, characterized by a high variability of widths and migration rates with a narrowing tendency and an eastward "jump" migration (Kombiadou et al., 2019). At East, the Cacela Peninsula is narrow (<150 m), has stabilized vegetated dunes (Ferreira et al., 2016) and a high overwash vulnerability (Kombiadou et al., 2019). At West, Cabanas Island is narrow (about 100 m in width), has low fragile dunes slightly above mean water level (~2.5 m) (Dias et al., 2003), a high overwash vulnerability (Garcia et al., 2010), and a fast recent accretion and eastward elongation (Kombiadou et al., 2019). As those barriers are highly interlinked, the along-shore growth of Cabanas Island leads to the shortening of the Cacela Peninsula (Kombiadou et al., 2019). Then, the position and shape of the Cacela Inlet also depends on this interaction.

The study of aerial photographs and historical maps from 1952 to 2014 realized by Kombiadou et al. (2019) to analyze the morphological evolution of the Ria Formosa barriers regarding natural and artificial modifications of the system, revealed a shift in the long-term evolution of the Cacela-Cabanas barrier system (Figure 2.7). This shift was described as a landward migration (barrier rollover) from 1952 to 1986 and a seaward progradation from 1986 to 2008 (Kombiadou et al., 2019). Since 2008, the Cacela-Cabanas system tends to migrate landward again due to the relocation of the inlet in 2011 and several storms that affected the region (Kombiadou et al., 2019).

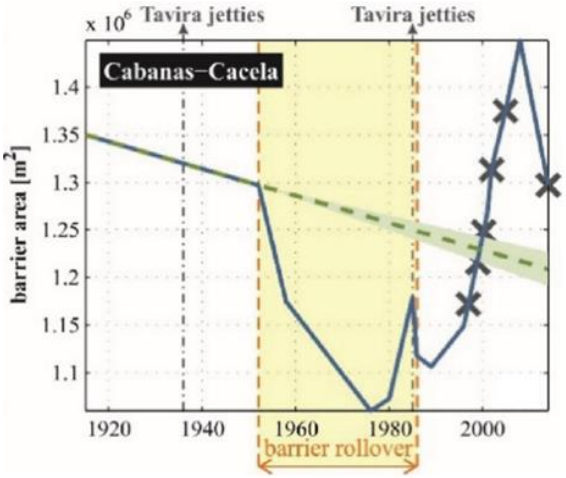

Figure 2.7 - Evolution of the Cacela-Cabanas barrier system (Kombiadou et al., 2019)(green dashed-lines: projected natural barrier area; blue solid lines: actual barrier areas; yellow shaded area: barrier rollover; crosses: nourishments; arrows: Tavira jetties construction and extension)

This long-term evolution of the Cacela-Cabanas barrier system (and its associated inlet by extension) is governed by both natural and anthropogenic factors that inhibited or promoted barrier growth and stability. Sediment from the shallow back barrier lagoon, overwash and longshore transport contributed to barrier growth, while inlet breaching, following multiple overwash as in the winter of 1995/1996 (Matias et al., 1999), inhibited barrier growth and stability (Kombiadou et al., 2019). In addition, some hard engineering works were performed such as Tavira jetties construction (1936) and extension (1977) impacting the barrier growth due to their upstream position as an obstacle to the eastward littoral transport. However, several soft coastal works like nourishments of the barrier Cacela-Cabanas system were done (1997, 1999, 2000, 2002, 2005, 2014) to promote its growth and stability (Dias et al., 2003; Kombiadou et al., 2019). The eastward relocation of the inlet in 2011 (Figure 2.8), that increased Cabanas Island length and shortened Cacela Peninsula, acted as a promotor of Cabanas Island growth and an inhibitor of Cacela Peninsula growth (Kombiadou et al., 2019).

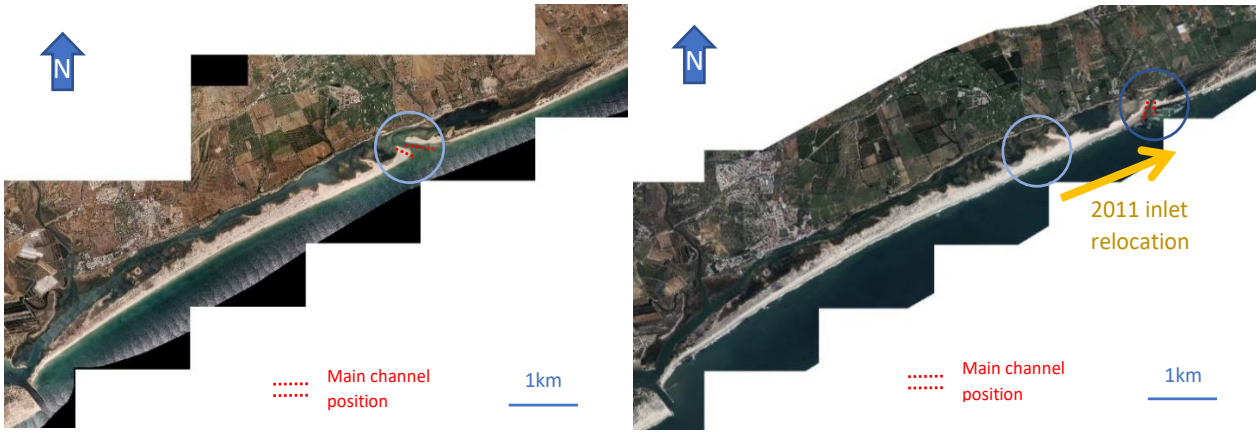

Figure 2.8 - Orthophotographs of Cacela-Cabanas barrier system in 2008 and 2014 (Direção-Geral do Território of Portugal)(Cacela Inlet position is represented before and after its relocation in 2011 respectively by the light blue circle and the dark blue circle)

Lacém Inlet was characterized by a continuous eastward migration (Figure 2.9) with highly variable widths (165 to 2000 m) and migration rates (3 to 215 m/yr) from 1952 until its closure in the 2011 and relocation of about 2 km eastward (Figure 2.8)(Kombiadou et al., 2019). It is a part of the low-energy eastern flank inlets of the Ria Formosa and its natural opening (before its artificial relocation) was due to barrier breaching induced by storm events (Vila-Concejo et al.,

2002). This type of inlets shows significant widths at the initial state that generally decrease with their migration, as the updrift barrier undergoes important accretions (Vila-Concejo et al., 2002). Due to the existing low dunes, the high overwash susceptibility of their margins can contribute to increase inlet width during important storm events (Vila-Concejo et al., 2002).

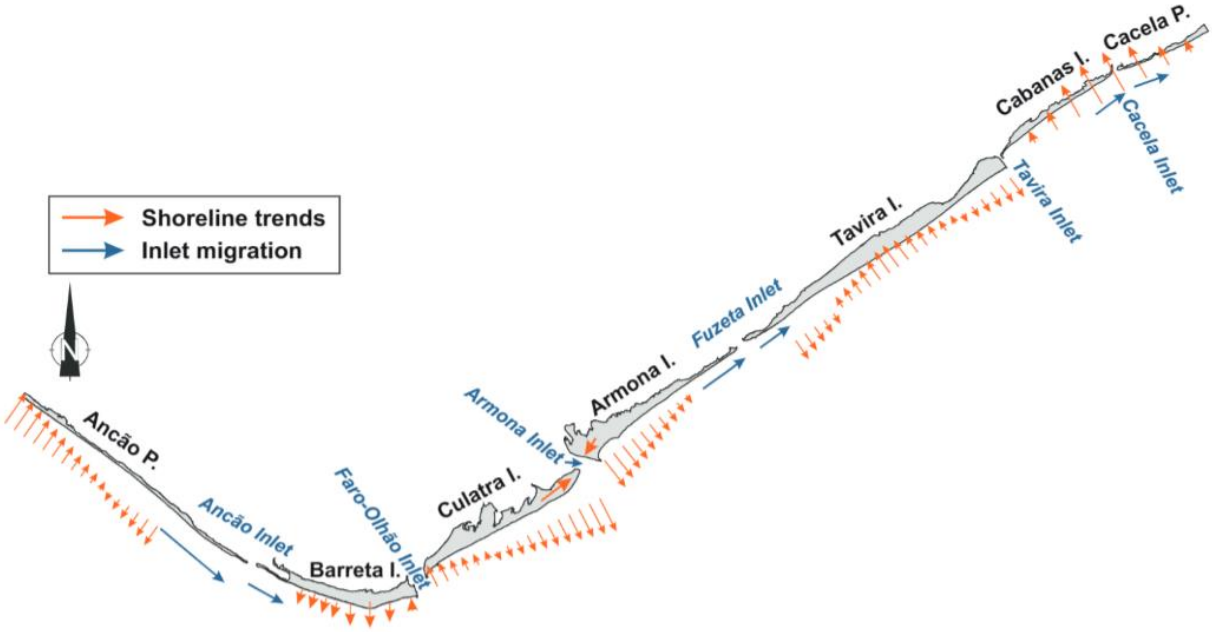

Figure 2.9 - Shoreline trends and inlet migration from 1952 to 2014 in the multi-barrier system of Ria Formosa lagoon (Kombiadou et al., 2019)

3. Materials and Methods

3.1. Satellite images

In the present study, Sentinel 2 imagery was chosen as it provides free high-resolution optical bands for land and water observations such as vegetation, soil and water cover, inland waterways and coastal areas (its 10 m of resolution being the appropriate one to observe the evolution of the small scale Cacela Inlet and ebb-tidal delta). Marine environments near the world's coasts are actively monitored using Sentinel 2 data as they allow high frequency monitoring from which coastal parameters (coastline position, intertidal structures, water depths, etc.) can be derived (Bergsma and Almar, 2020).

The Sentinel-2 data coverage along a single orbit is composed by a set of Granules (minimum indivisible partitions of the coverage grid), which are called Tiles (100 km x 100 km squared ortho-images in cartographic reference frame Universal Transverse Mercator / World Geodetic System 1984 projection) for ortho-rectified products (Gatti and Galoppo, 2018). The tile T29SPB was selected as it is the only granule that records images of Cacela-Cabanas barrier system. It covers from longitude -6.72° to -7.88° and from latitude 37.02° to 37.94° (Figure 3.1), including the eastern flank of the Ria Formosa.

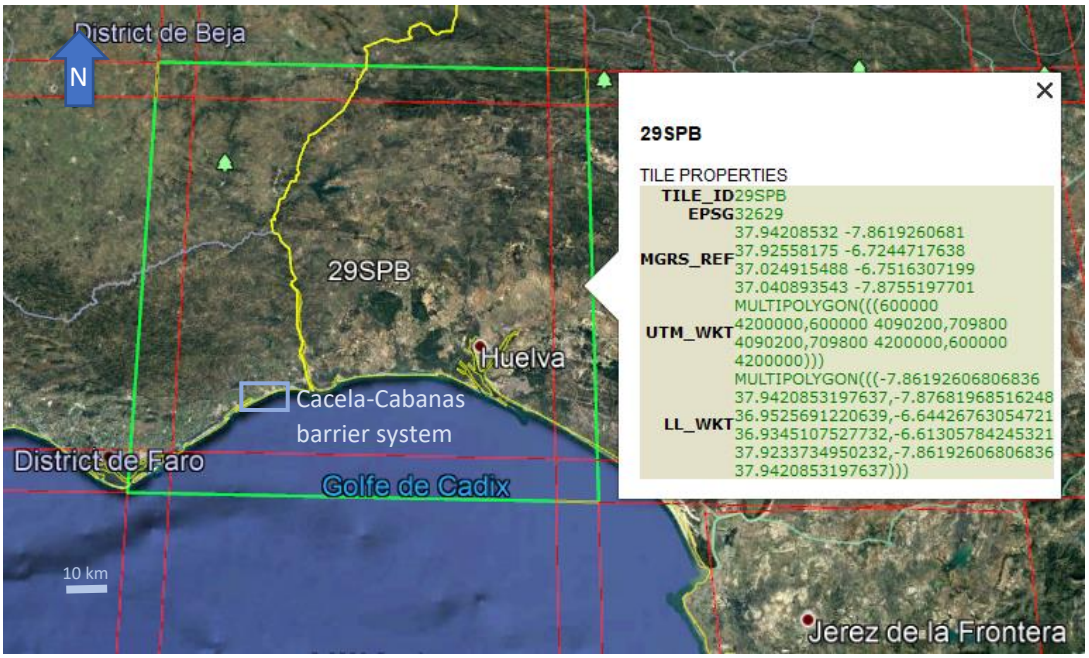

Figure 3.1 - Tile 29SPB properties and definition from Sentinel-2 tiles raw (sentinel.esa.int) on Google Earth

Each image file, downloaded from the ESA Copernicus datahub (scihub.copernicus.eu), included 13 spectral bands of different spectrum that range from 433 to 2280 nm penetrating aquatic environment to assess various environmental properties. The blue spectrum (450-520 nm) of B02-Blue band can show adapted characteristics for clear water bathymetry with a low electromagnetic radiation attenuation and strong penetration capabilities (Gao, 2009). However, as inlets embody highly turbid water masses, longer radiation would better fit to study these systems. Warne (1978) and Kumar et al. (1997) recommended the spectrum of 500-600 nm and 770-800 nm, respectively covered by bands B03-Green and B07-RedEdge. The first one, sensible to wavelength ranging between 543 and 578 nm, is used for clear and turbid waters and vegetation study with a 10 m resolution, while the second one, with a wavelength range of 773 to 793 nm, is used for vegetation classification and has a 20 m resolution. Thus, as the highest resolution is required to delineate the submerged structures in the turbid environment of Cacela Inlet and ebb-tidal delta, bands B03-Green were used to study its morphodynamics.

As the first Sentinel-2 satellite was launched on the 22th of June 2015, a timeframe from September 2015 (first image available with good weather and low tidal level) to September 2020 (last image available with good weather and low tidal level at the beginning of the thesis) was defined to study the short-term morphologic evolution of Cacela Inlet and ebb-tidal delta. Two images per year (about every 6 months) were analyzed in March and September (except for March 2017 which had no usable image and is replaced by an image from early April 2017) to check for general shoals' morphological characteristics and changes and reveal possible seasonality. Moreover, the time interval between the images was reduced (e.g., one image almost every 2 months) to track the short-term morphological changes observed at 6 months interval. This approach allowed investigating how short-term wave conditions and energetic events (e.g., eastern or western wave/storm occurrence, low wave conditions, highly energetic periods, etc.) were related to the observed morphological changes.

Each image file was selected according to their quality (low cloud coverage and light reflection) at the position of the Cacela-Cabanas system and according to low tide periods (table 3.1), as those are the ideal conditions to distinguish submerged structures. The quality of the images was ranked from 1 to 5 for their selection (1 being the highest quality and 5 the lowest). When no

high-quality images were available, an inferior quality class was chosen if usable or alternatively another image from the previous/next month. For a total of 619 images from 2015 to 2020, 287 presented no cloud coverage and no light reflection (Quality 1 in dark green in Figure 3.2), 84 no cloud coverage but light reflection (Quality 2 in light green in Figure 3.2), 46 a low cloud coverage (Quality 3 in yellow in Figure 3.2), 47 a medium one (Quality 4 in orange in Figure 3.2) and 155 a high one (Quality 5 in red in Figure 3.2). Images of quality 1 were selected for most of the periods with some time interval shifts (several images not selected precisely every 2 months), except the images of March 2016 and September 2020 that had a quality index of 3 due to a medium cloud coverage (that do not disturb the observation of the study area).

Figure 3.2 - Number of 29SPB Tile Sentinel-2 images according to their quality per month

Tidal level data from 2015 to 2020 were computed using the T_TIDE function (Pawlowicz et al.,2002) in MATLAB from tidal harmonics obtained at the Guadiana mouth (37° 10' 1.2'' N) from long-term water level observations (Garel and Ferreira, 2015). The tidal level time series (Figure 3.3), calculated from the tidal harmonics, indicated a maximum spring tide level of 1.85 m and a minimum spring tide level of -1.79 m, referred to mean sea level (MSL). All the selected images were taken at tide levels ranging from -0.65 m to -1.45 m (table 3.1). The averaged tidal level was -1.04 m MSL.

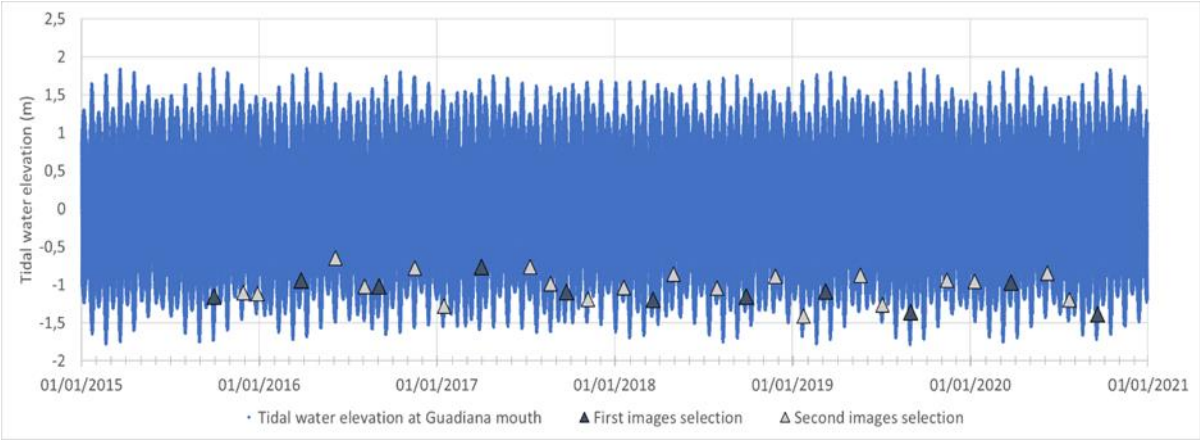

Figure 3.3 - Tidal water elevation at Guadiana's mouth from 2015 to 2020 with the selected images dates and levels (triangles)

Table 3.1 - Tidal water elevation values at the time of selected images acquisition from September 2015 to September 2020

Date	Tidal elevation (m)	Date	Tidal elevation (m)
30/09/2015	-1,15	02/05/2018	-0,86
29/11/2015	-1,11	31/07/2018	-1,04
29/12/2015	-1,12	29/09/2018	-1,15
28/03/2016	-0,94	28/11/2018	-0,89
06/06/2016	-0,65	25/01/2019	-1,41
05/08/2016	-1,02	11/03/2019	-1,09
04/09/2016	-1,02	22/05/2019	-0,88
16/11/2016	-0,78	06/07/2019	-1,27
15/01/2017	-1,28	02/09/2019	-1,36
02/04/2017	-0,77	16/11/2019	-0,94
11/07/2017	-0,76	12/01/2020	-0,96
23/08/2017	-0,98	27/03/2020	-0,97
24/09/2017	-1,09	10/06/2020	-0,84
08/11/2017	-1,19	25/07/2020	-1,20
20/01/2018	-1,04	21/09/2020	-1,39
21/03/2018	-1,20		

3.2. Morphologic parameters definition

Quantum GIS 3.16 'Hannover' software was used for the visualization of the morphologies of the Cacela Inlet and ebb-tidal delta through the testing and variation of image properties (e.g., clarity, saturation, lighting…). This Geographic Information System (GIS) is a free, open-source and easy tool to assess the morphological parameters that can be measured on satellite imagery or defined on maps. This software supports viewing, editing, and analysis of geospatial data using raster and vector layers and allows the composition and export of graphical maps (Azizian, 2017).

As the tile 29SPB covers a large area, the satellite images were clipped according to the zone of interest between 628 800 m and 630 500 m on x-axis and between 4 112 300 m and 4 113 500 m on y-axis in the UTM29N coordinate system (-7.54964184° to -7.53029529° of longitude and 37.14822305° to 37.15880075° of latitude).

In order to study their evolution and to delimit the Cacela inlet and ebb-tidal delta, the barriers were digitized through a line (orange line represented in Figure 3.4) drawn at the boundary between the emerged (white) and submerged (grey) domain of the sandy strip. As the barriers included vegetation that was partially underwater on the back-barrier basin side and visible in black, the limit at the back of the barrier was partially interpreted from Google Earth images. From the barriers spits boundaries, the width of the inlet (grey line in Figure 3.4) was measured as the minimum width between the two barrier spits boundaries. The mean position of this inlet (white dot in the center of the grey line in Figure 3.4) was defined at the center of this minimum width in order to inform about the inlet migration during the study period.

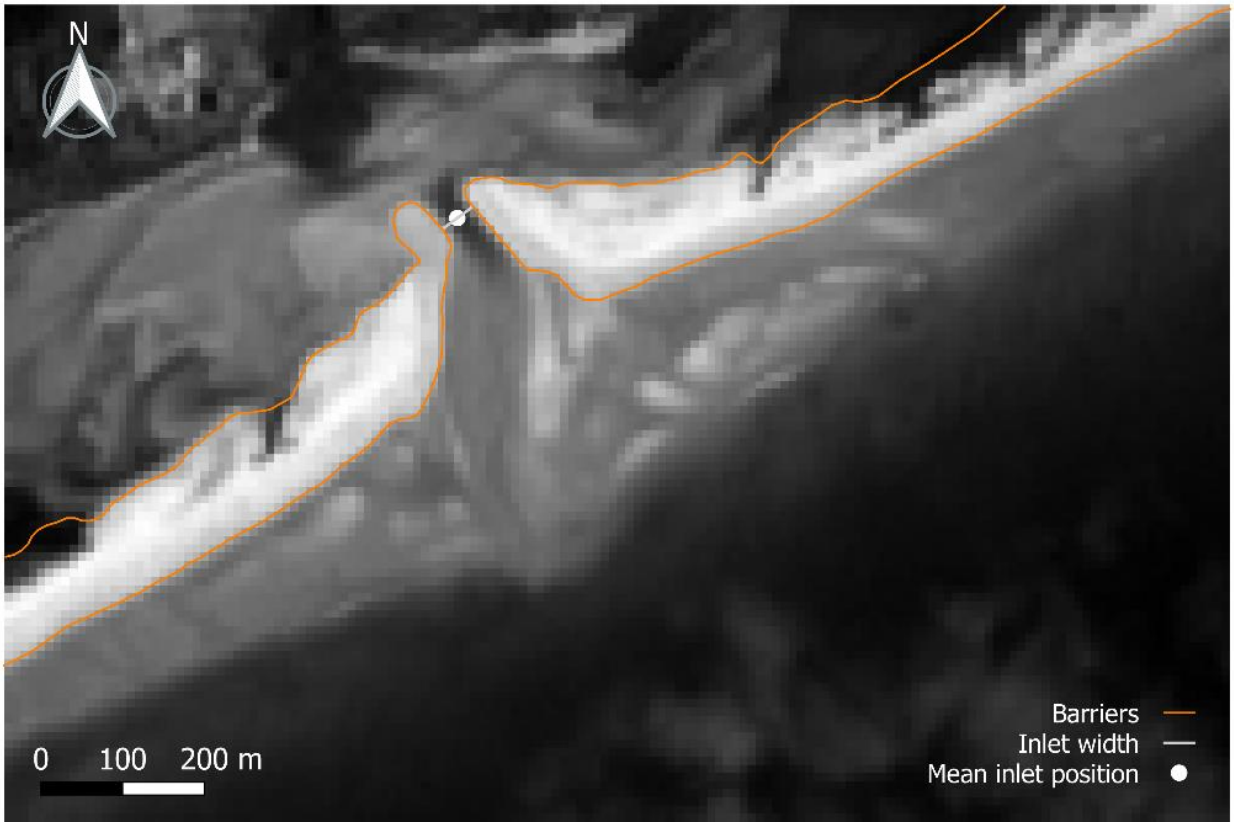

Figure 3.4 - Example of parameters definition for barriers (limits) and inlet (width and position)(image of the 21/09/2020)

To limit the ebb-tidal delta of Cacela, its extension was delimited morphologically (as represented by the pink dashed line in Figure 3.5) up to the barriers in the continuity of the outer shoal/tip, visible at the delta front, and where the shoals were almost parallel to the barriers, belonging to the platform in front of the beach. This ambiguous parameter, due to the lack of a clear boundary, was defined by morphological interpretation and was used to get an idea of the general shape of the delta. Furthermore, the position of the tip of the outer shoal, and by extension of the delta, was defined as the most extreme position in front of the seaward end of the main ebb channel (as represented by the pink dot in Figure 3.5).

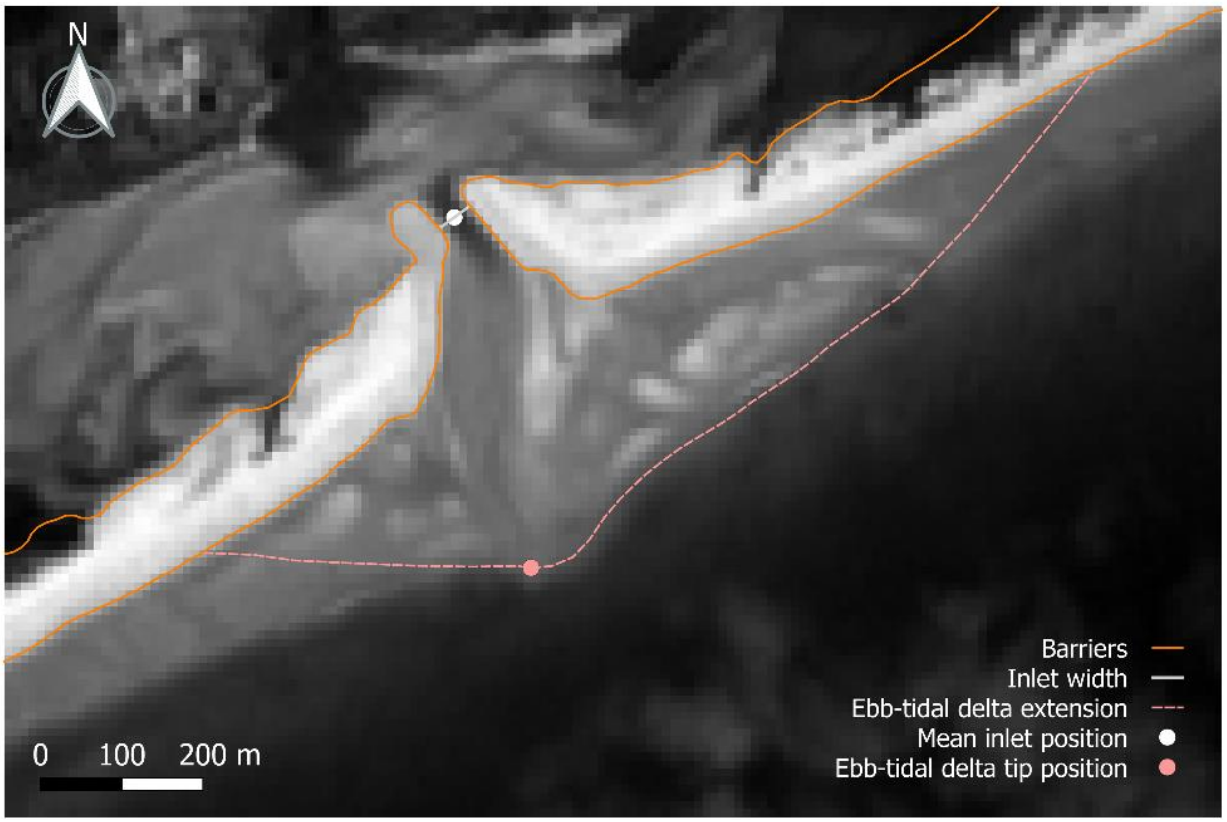

Figure 3.5 - Example of parameters definition for barriers (limits), inlet (width and position) and ebb-tidal delta (tip and extension)(image of the 21/09/2020)

The various submerged shoals of the ebb-tidal delta were delimited and digitized with demarcation lines (red line in Figure 3.6) at the location of highest contrast between light grey (shallow water) and dark grey (deeper water). The orientation of barely visible shoals was noted as doubled dashed lines.

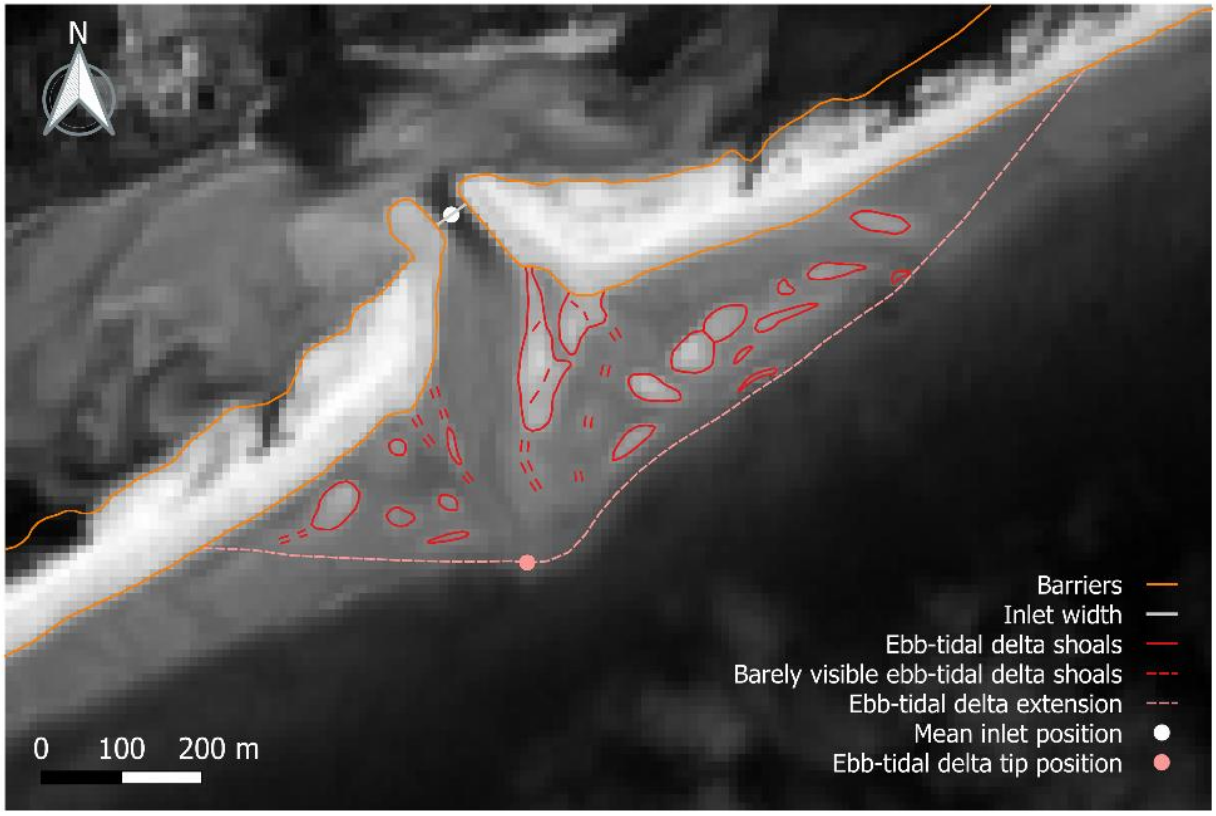

Figure 3.6 - Example of parameters definition for barriers (limits), inlet (width and position), and ebb-tidal delta (tip, extension and shoals)(image of the 21/09/2020)

The main ebb channel position was digitized as a line along the maximum depth (thalweg) corresponding to the darkest path from the inlet minimum width to the ebb-tidal delta tip (blue line in Figure 3.7). The position of the ebb channel at inlet was defined at the intersection between the main ebb channel and the minimum inlet width (as represented by the blue dot in Figure 3.7). As the channel was often deflected updrift or downdrift over the ebb delta, it was split in two sections: the upper ebb channel corresponding to the landward part (from its position at the inlet to its position at the maximum delta width) and the lower ebb channel corresponding to the seaward part across the ebb-tidal delta (from its position at the maximum delta width to the delta tip). The orientations of the lower and upper channels were collected (in degrees from the North, positive clockwise) considering straight lines between those positions.

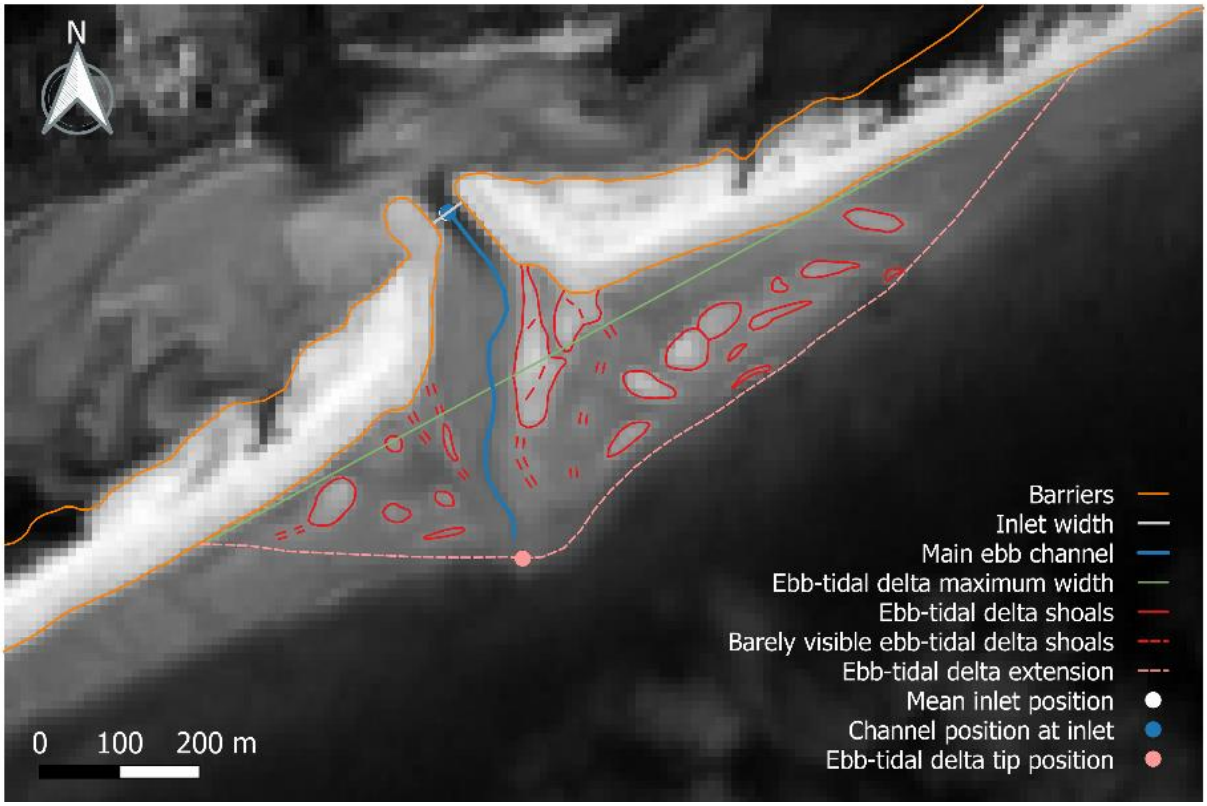

Figure 3.7 - Example of parameters definition for barriers, inlet, ebb-tidal delta (tip, extension, shoals and maximum width) and ebb channel (track and position at inlet)(image of the 21/09/2020)

These morphological features of the system were noted for all used images (appendix 1), and structural diagrams were drawn in QGIS for images with 6 months interval to reveal shoals' general characteristics and possible seasonality. The extracted different positions (channel position at inlet, ebb-tidal delta tip position and mean inlet position), which had coordinates stated in the UTM29N coordinate system in QGIS, were extracted and computed according to a new reference frame (Figure 3.8) rotated 27.65° anticlockwise to get the along-shore and cross-shore positions referring respectively to x and y axis parallel and perpendicular to the mean barriers orientation. The origin of this new reference frame was fixed at a position (northing of 629 556 m, easting of 4 112 947 m) which correspond approximately to the center between the inlet and ebb-tidal delta interpreted from the barrier, inlet, ebb-tidal delta extension and channel envelopes. Positive alongshore values were eastward (or downdrift as the main longshore transport was eastward) and negative were westward (updrift) with respect to the origin. Likewise, positive cross-shore values were landward and negative values were seaward.

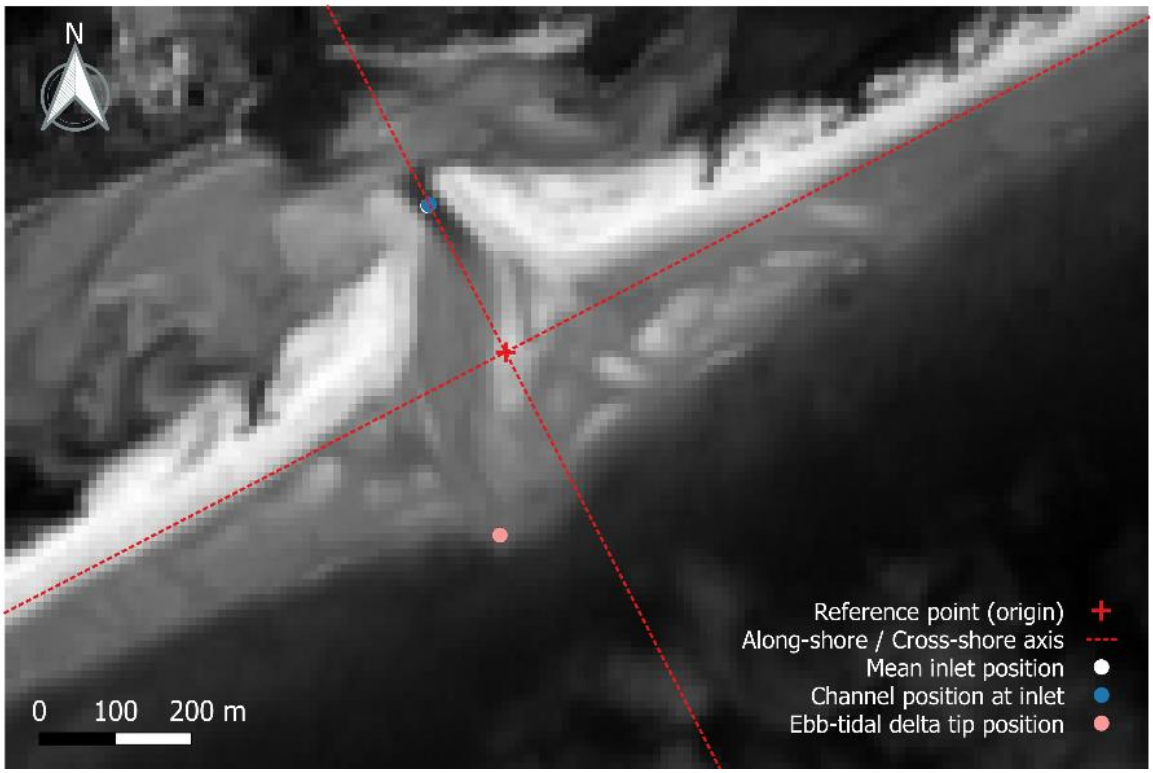

Figure 3.8 - Example of selected positions with the new reference frame (image of the 21/09/2020)

3.3. Morphology and morphodynamics analysis

The morphological analysis of the Cacela inlet and ebb-tidal delta was performed through the morphological interpretation of the structural diagrams of the images with 6 months interval to reveal shoals' general characteristics and possible seasonality. Moreover, the mean and extreme values of the studied parameters were computed and different envelopes of variability were made for the barriers, the inlet, the channel and the delta extension to get the general morphology and variability of those features.

The analysis of the morphodynamics of the inlet and ebb-tidal delta was based on the temporal evolution and the changes in shape, orientation, position and length of the selected features between the almost 2-months interval images. Rates of change per day were computed between the images to quantify those temporal evolutions and periods of trends or typical behaviors were analyzed for each parameter. From those periods, general periods of interest with similar and/or simultaneous behaviors were selected to see the overall evolution of the studied system and look for the relationships between the different parameters.

3.4. Hydrodynamic forcing

Wave's characteristics from 2015 to 2020 were obtained from the Puertos del Estado SIMAR44 dataset at point 5024022 (37.08° N, 7.50° W, as represented in Figure 3.9), about 9 km southeast off the Cacela Inlet. The SIMAR44 ensemble results from high-resolution numerical models of the atmosphere, providing sea level and waves covering the entire Iberian coastal environment since 1958, and generated by Puerto del Estado in the framework of the European project HIPOCAS. It models, among others, hourly values of significant wave height (Hs, in meters), spectral peak wave period (Tp, in seconds) and mean wave direction at peak frequency (θ, in degrees) that were used for the characterization of the wave climate from 2015 to 2020. Most of the values computed were lower than those found in the literature. For example, the portion of waves with Hs > 2.5 m should be 5% (definition for storms at this area according to Almeida et al., 2012, and Oliveira et al., 2018), while it represented only 1% in the dataset. This is probably due to the fact that the selected point is at shallow depth (about 20m), sheltered from southwest waves and that the model included wave refraction processes.

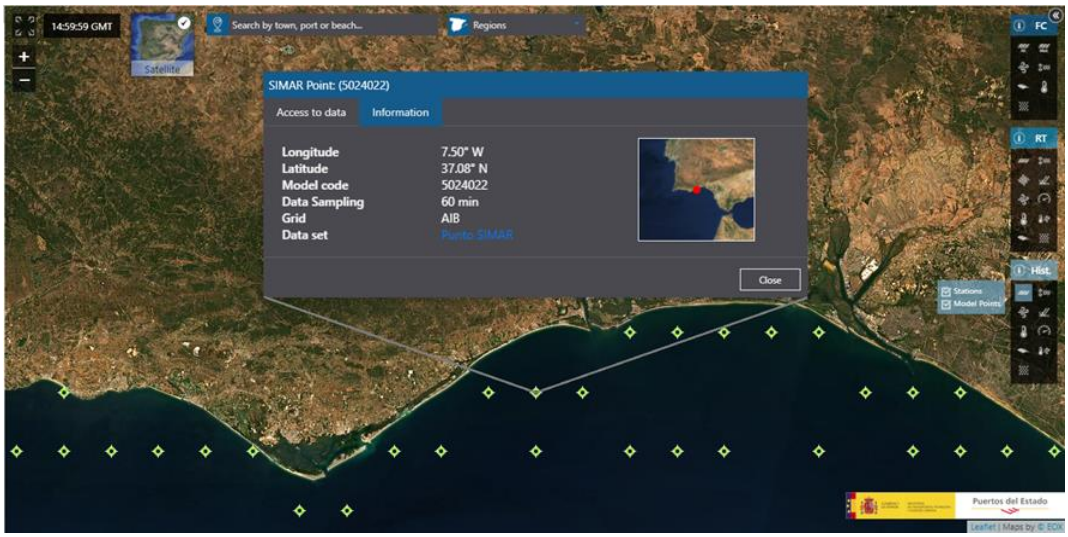

Figure 3.9 - Position and characteristics of the SIMAR point 5024022 (Puertos del Estado, screenshot from puertos.es)

Hs values were computed from 2015 to 2020 to evaluate their evolution according to their western or eastern orientation θ and to identify periods of storms. Moreover, they were separated by considering small waves lower than 0.5 m (as the mean Hs was 0.6 m for the whole dataset and they represented almost 55% of it), medium ones between 0.5 and 1.5 m (40% of the dataset), high ones between 1.5 and 2.5 m (4% of the dataset) and very high ones above 2.5 m

(offshore storm threshold, representing almost 1% of the dataset). This separation was defined in order to clarify the potential influence of Hs on the system and three major storms (most important and representatives) were selected to analyze their impact.

Due to the strong bidirectionality of the wave climate in this region, waves were also separated in two main directions to verify how the origin of the waves influences the morphology. Eastern waves were defined as $0° < \theta < 180°$ and western ones as $180° < \theta < 360°$.

The wave power (P, in W/m) was computed based on Hs and Tp (equation 1) to evaluate the energy that was delivered to the system (i.e., the energy flux per unit of crest). This equation was developed (appendix 10) from the different equations of the Linear (Uniform) Wave Theory depicted by Holmes (2001), where P is equal to the product between the energy (E) and the group velocity (Cg) of the waves.

$$P = E \times Cg = \frac{1.56 \rho g Hs^2 Tp}{16} \quad (1)$$

The number of hours of eastern or western waves was also computed between the images and for the previously mentioned periods of interest in order to have an idea of their temporal dominance.

To get the total wave power received by the system from an image to the next one, the cumulative power (Pc, in W/m) of western and eastern waves was computed, expressed by the sum of the P values between the acquisition times of the images. As the duration between the selected images and for the periods of interest varies, the parameterized power per hour (Pch, in W/m/h) of western and eastern waves between images was also computed between the images and for the periods of interest to complement the analysis. This parameter was computed by dividing the cumulative power between images by the number of hours between their acquisition times.

The power timeseries were analyzed according to western or eastern waves from 2015 to 2020 in order to characterize their temporal evolutions and maximum values.

From those parameters, relationships can be stated with the observed morphodynamic changes of the Cacela Inlet and ebb-tidal delta in function of wave power and direction.

4. Results

4.1. Cacela ebb-tidal delta shoals

4.1.1. Morphology

Through the morphological analysis of the shoals, what was observed at first sight is the important variability of their sizes, shapes and orientations. Indeed, these shoals were almost constantly evolving from image to image and did not reveal clear trends or repeated cyclicities. However, some characteristics, behaviors and seasonality were perceived.

The downdrift part of the ebb-tidal delta was often more developed than the updrift part with large sandbars on its swash platform (as represented in most of the morphological diagrams of Figure 4.1, except diagrams f-g of the year 2018). Its more or less elongated bars were mostly sub-parallel and attached to the downdrift barrier (Figure 4.1b,c) or not (Figure 4.1a,d,f,g,h,i,j). They were particularly well-developed and elongated in winter and dispersed across the ebb-tidal delta in summer, especially for the years 2019 and 2020 (represented in Figure 4.1h,j at the end of winter and Figure 4.1i,k at the end of summer). The downdrift channel margin linear bar was mostly well-developed and sub-parallel to the ebb channel and it was mostly attached or partially attached to the barrier (as represented in most of the diagrams of the Figure 4.1). However, it did not reveal seasonal trend as the swash shoals.

The updrift part was more restricted (smaller area) than the downdrift one and composed of medium or small shoals oriented differently between images: mostly subparallel to the barriers (Figure 4.1c,e,i,j) and/or to the ebb channel (Figure 4.1b,d,f,g). It also showed sometimes a spit-shaped shoal attached especially to the updrift barrier close to the inlet mouth (Figure 4.1b,c,d,e,g,h,i) that can act as channel margin linear bar in some cases (Figure 4.1d,e,i). However, this part of the ebb-tidal delta was more difficult to analyze as the shoals were not as well developed as the downdrift ones and were not often visible. Moreover, the features of this part of the delta showed no obvious trends, cyclicity and seasonality.

An important change in the general morphology of the Cacela inlet and ebb-tidal delta was noted in March 2018 showing important shoals and spit platforms inside the wide inlet (Figure 4.1f). Even though they were underwater, they seemed to be part of the old spits of the barriers. The

ebb-tidal delta and the inlet returned to their original state in September 2018 (Figure 4.1g), or even July 2018 (image 18 in appendix 1).

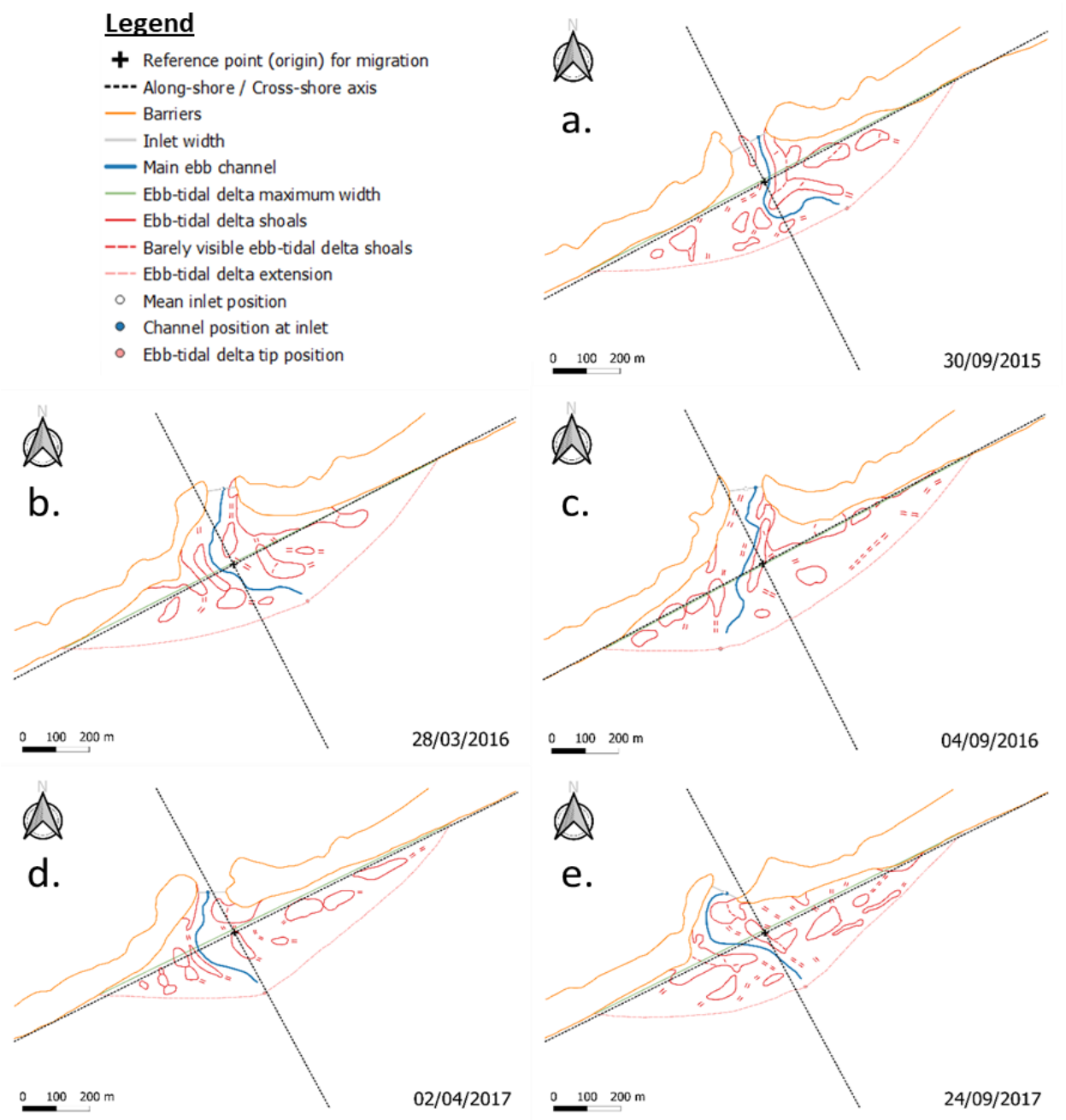

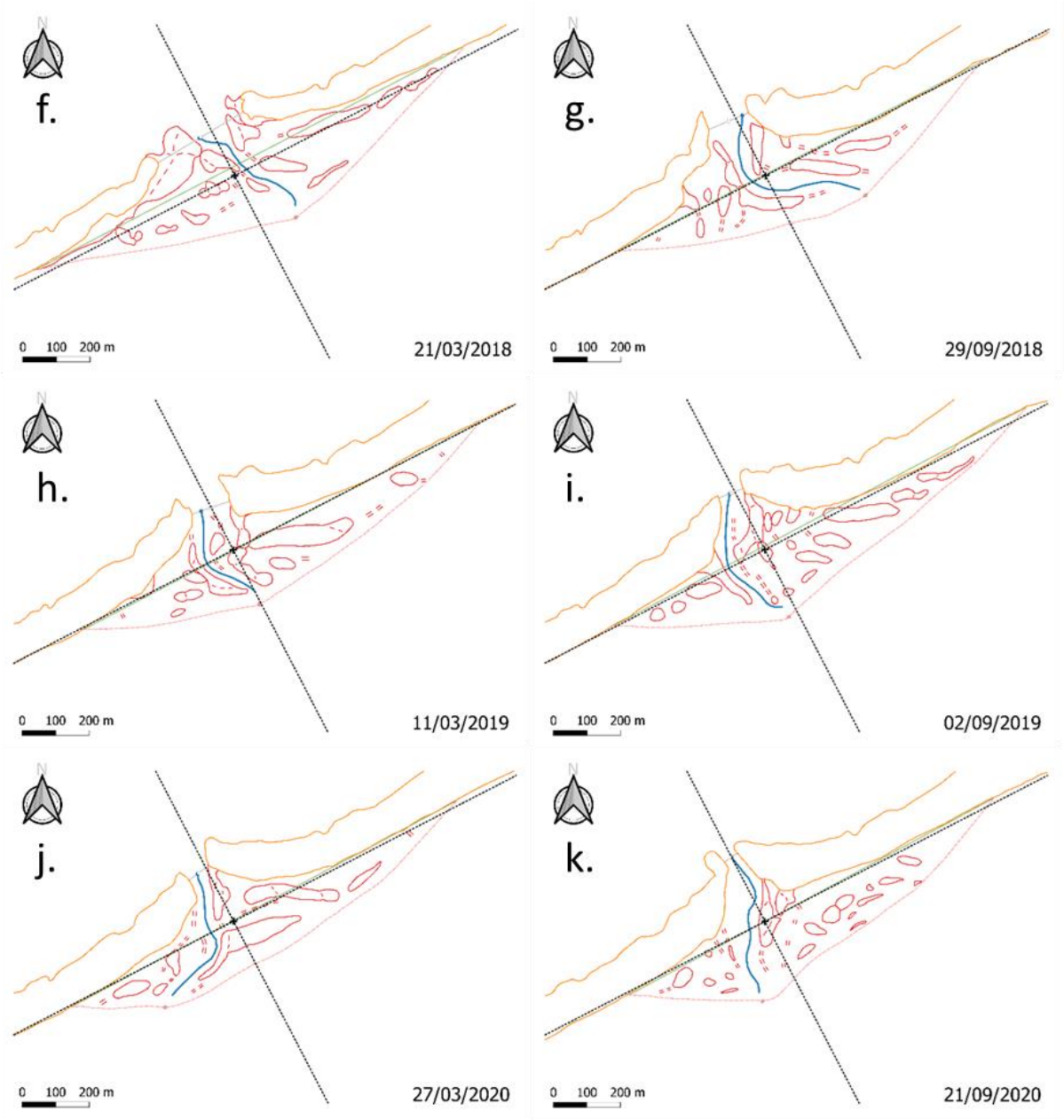

Figure 4.1 - Morphological diagrams of Cacela inlet and ebb-tidal delta system from September 2015 to September 2020

4.1.2. Morphodynamics

The position of the shoals was highly variable, with shoals sometimes close to the barriers, close to the sea front, close to the center/ebb channel, close to the sides of the ebb-tidal delta or even scattered across the swash platform. From those various positions, some notable displacements were observed with shoals migrating to the barriers, especially on the downdrift part of the ebb-tidal delta. Such migrations lasted about 1 year (when they were clearly visible) from the

formation of the shoals to their attachment to the barrier. As an example, the Figure 4.2 showed a shoal forming around December 2015 on the downdrift side of the tip, transforming into a large crescent shoal in March 2016, then into a bright triangular shoal visible from June to August 2016, to a long bar close to the downdrift barrier in September 2016 and finally attaching to the downdrift barrier in November 2016. By analyzing the shoal's evolution at all the different images in appendix 1, those shoals formed and migrated almost all along the year but formed and migrated faster in winter.

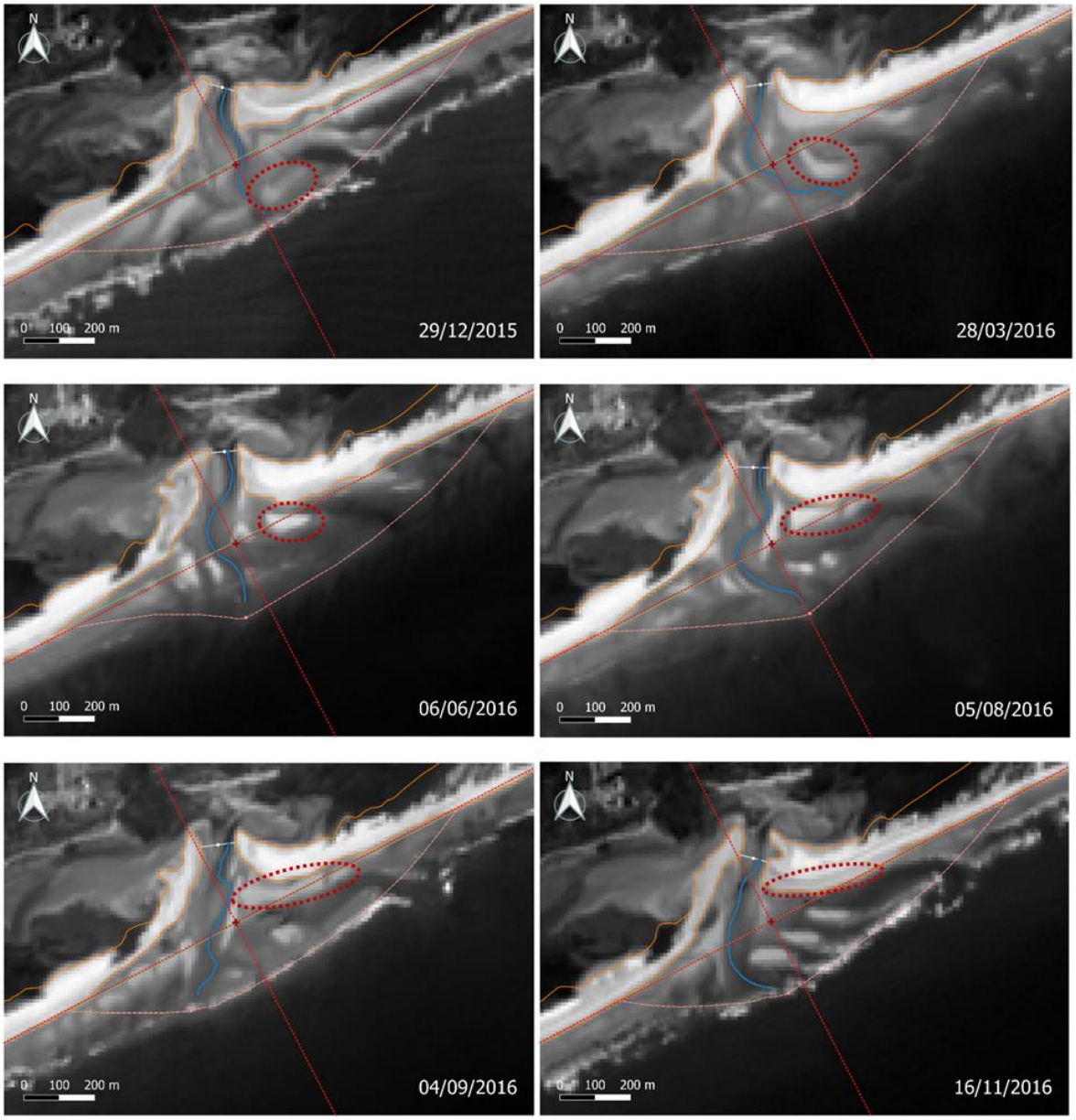

Figure 4.2- Example of shoal migration and welding to the barriers (red dashed circle: approximate shoal position and extension)

4.2. Cacela ebb channel and ebb-tidal delta tip

4.2.1. General morphology

The analysis of the approximately 2-monthly spaced parameters of the main ebb channel (orientation and extremities migration) revealed a clearly visible aspect of the significant short time scale variability of the Cacela ebb-tidal delta. The envelope obtained from the digitized main ebb channels, the one obtained from the ebb-tidal delta extension but also the positions of the ebb channel at inlet and the ebb-tidal delta tip (Figure 4.3) showed a high variation of the main ebb channel across the ebb-tidal delta, especially seaward, from September 2015 to September 2020. The ebb channel, which was deflected most of the time from a North-South (N-S) orientation landward toward the South-East (SE) seaward, showed different orientation evolutions regarding its upper part and its lower part (Figure 4.3 and appendix 2). Moreover, it showed a quite stable position at the inlet with few shifts (mainly downdrift but larger updrift) and a highly variable tip position (Figure 4.3).

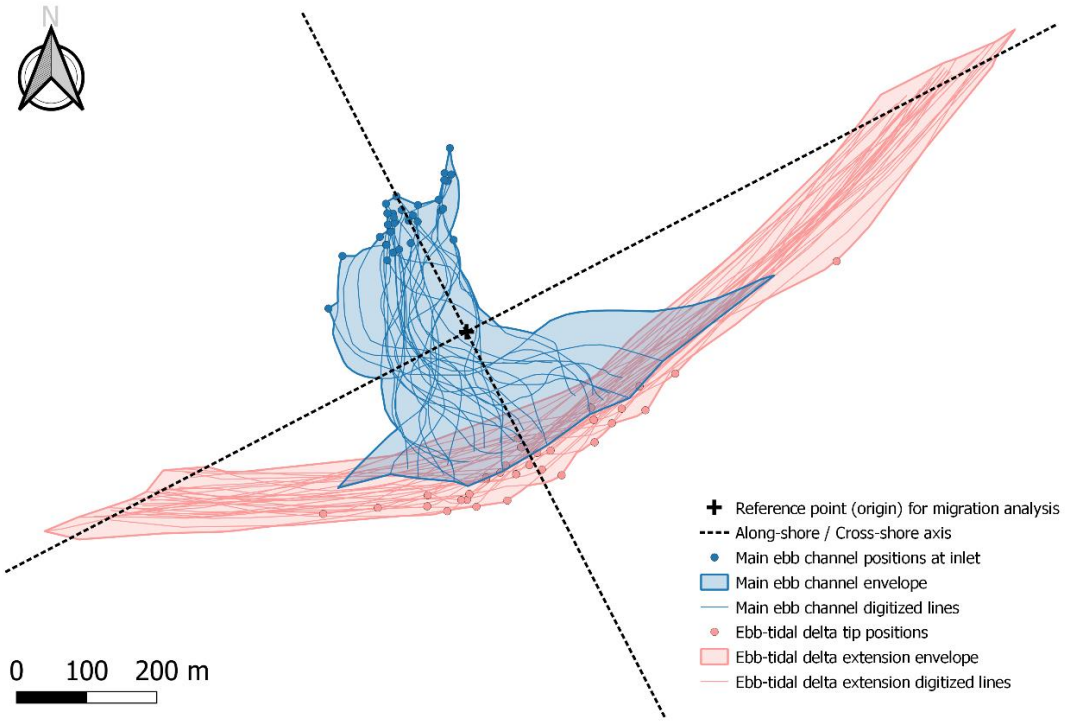

Figure 4.3 - Main ebb channel and ebb-tidal delta extension envelopes and digitized lines (for all analyzed images) associated with main ebb channel positions at inlet and tip positions of Cacela ebb-tidal delta from September 2015 to September 2020

4.2.2. Upper ebb channel morphodynamics

The upper part of the ebb channel had mainly a N-S orientation with a mean value of 170° along the timeframe, a mean rate of change of + 0.01 °/day between the images, and maximum and minimum values of 200° (N-S) and 122° (NW-SE) (corresponding respectively to images 8 of November 2016 and 15-16 of January-March 2018 in appendix 1)(statistic values in appendix 6). From its temporal evolution (Figure 4.4 with values in appendix 2 and change and rate of change values in appendix 4), a first trend was observed from September 2015 to November 2016 with an upper channel that rotated anticlockwise from an orientation of 163° (N-S) to an orientation of 200° (N-S) with a mean rate of change of + 0.07 °/day (Figure 4.4a). From November 2016 to March 2018, a second one revealed an upper channel that rotated clockwise from an orientation of 200° (N-S) to an orientation of 122° (NW-SE) with a mean rate of change of - 0.12 °/day and an attenuation during summer 2017 (Figure 4.4b). Then, it undergone no change from March to May 2018 (0° of change)(Figure 4.4c) and started again an anticlockwise rotation from May until November 2018 with a mean rate of change of + 0.18°/day, returning close to its mean N-S orientation with a value of 177° in November 2018 (Figure 4.4d). From November 2018 to September 2020, it showed no important rotations and evolved meanly around 172° with no mean rate of change (0.00 °/day) (Figure 4.4e).

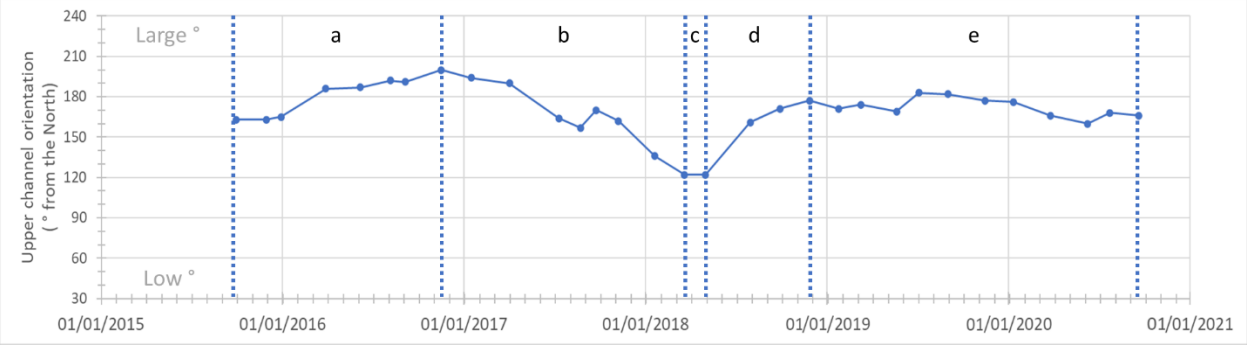

Figure 4.4 - Cacela upper ebb channel orientation evolution with its associated different periods (a,b,c,d,e) from September 2015 to September 2020

The upper channel alongshore position at inlet showed a mean value at - 1 m along the timeframe, a mean rate of change of - 0.01 m/day between the images, and maximum and minimum values at 100 m and -159 m (corresponding respectively to images 5 of June 2016 and 15 of January 2018 in appendix 1)(statistic values in appendix 6). From its temporal evolution (Figure 4.5 with values

in appendix 3 and change and rate of change values in appendix 4), a first trend was observed from September 2015 to June 2016 with a position that migrated downdrift from + 44 m to + 100 m with a mean rate of change of + 0.33 m/day (Figure 4.5a). From June 2016 to January 2018, it migrated updrift from a position at + 100 m to a position at - 159 m with a mean rate of change of - 0.37 m/day and an attenuation during summer 2017 (Figure 4.5b). Then, it migrated downdrift again from January 2018 to September 2018 from a position at - 159 m to a position at + 22 m with a mean rate of change of + 0.65 m/day and a notable jump of + 118 m from January to March 2018 (Figure 4.5c). From September 2018 to September 2020, it showed no notable variations, going from a position at + 22 m to a position at + 1 m with a mean rate of change of - 0.03 m/day (Figure 4.5d).

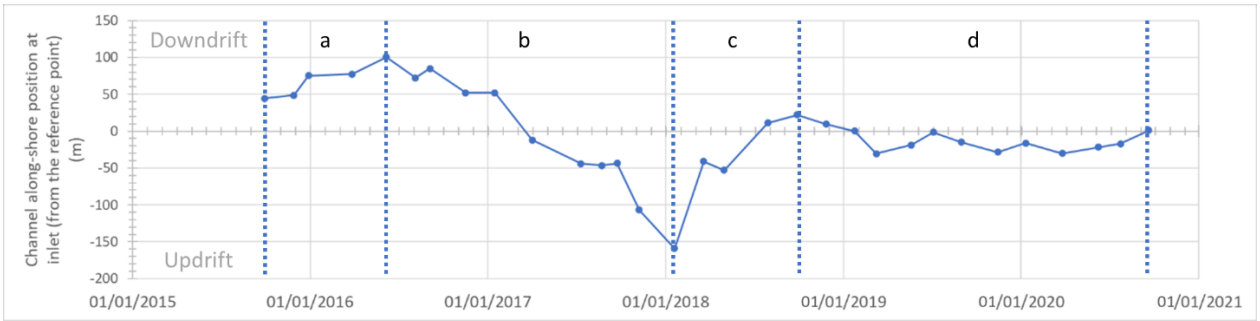

Figure 4.5 - Cacela ebb channel along-shore position evolution at the inlet with its associated different periods (a,b,c,d) from September 2015 to September 2020

The upper channel cross-shore position at inlet showed a mean value at + 181 m along the timeframe, a mean rate of change of + 0.07 m/day between the images, and maximum and minimum values at + 243 m and + 121 m (corresponding respectively to images 5 of June 2016 and 15 of January 2018 in appendix 1)(statistic values in appendix 6). From its temporal evolution (Figure 4.6 with values in appendix 3 and change and rate of change values in appendix 4), a first trend was observed from September 2015 to June 2016 with a position that migrated landward from a position at + 125 m to a position at + 243 m with a mean rate of change of + 0.60 m/day (Figure 4.6a). From June 2016 to January 2018, it migrated seaward from a position at + 243 m to a position at + 121 m with a mean rate of change of - 0.17 m/day and an attenuation in summer 2017 (Figure 4.6b). Then, from January 2018 to September 2020 it showed a slight landward migration from a position at + 121 m to a position at + 218 m with a mean rate of change of + 0.08 m/day (Figure 4.6c). During this last period, the upper channel cross-shore position at inlet

showed a notable seasonality with a position that migrated landward in summer (March to September here) and seaward in winter (September to March)(Figure 4.6c).

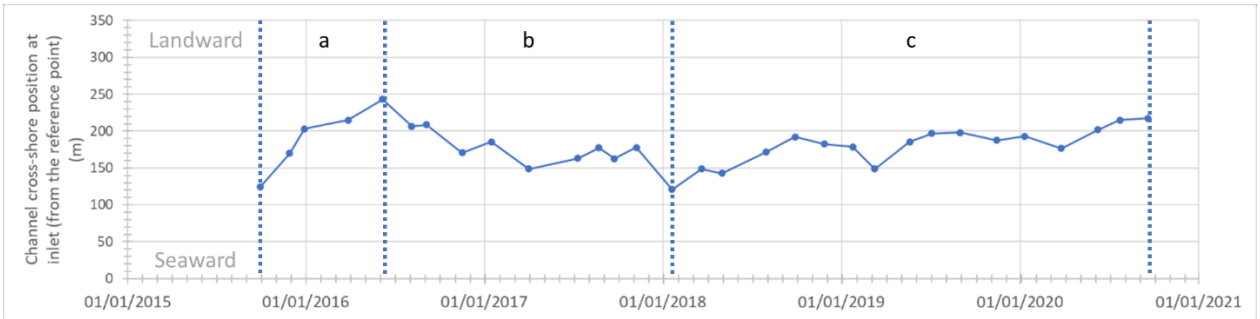

Figure 4.6 - Cacela ebb channel cross-shore position evolution at the inlet with its associated different periods (a,b,c) from September 2015 to September 2020

4.2.3. Lower ebb channel morphodynamics

The lower part of the main ebb channel had much more variable orientations than the upper part, mostly in the NW-SE (or often in the N-S axis) with a mean value of 139° (NW-SE) along the timeframe, a mean rate of change of + 0.07 °/day between the images and maximum and minimum values of 313° (NE-SW) and 77° (E-W)(corresponding respectively to image 28 of March 2020 and image 20 of November 2018 in appendix 1)(statistic values in appendix 6). From its temporal evolution (Figure 4.7 with values in appendix 2 and change and rate of change values in appendix 4), first period, from September 2015 to November 2016, was characterized by a sawtooth evolution in the lower ebb channel orientations evolving from 110° (E-W) to 132° (NW-SE) with a mean rate of change of + 0.24 °/day and maximum and minimum values of 191° (N-S) in August 2016 and 108° (E-W) in March 2016 respectively (Figure 4.7a). This highly variable evolution was characterized by short-term periods of 4 to 6 months marked by inverse shifts of this part of the channel (Figures 4.7a). From November 2016 to March 2018, the variations were attenuated, going from an orientation of 132° (NW-SE) to an orientation of 129° (NW-SE) with a mean rate of change of - 0.05 °/day and maximum and minimum values of 171° (N-S) in August 2017 and 104° (E-W) in January 2018 (Figure 4.7b). From March 2018 to November 2018, the lower channel started to show clearer trends through a first clockwise rotation from an orientation at 129° (NW-SE) to an orientation at 77° (E-W) with a mean rate of change of - 0.20 °/day (Figure 4.7c). Then, from November 2018 to March 2020, it undergone an anticlockwise rotation from an orientation of 77° (N-S) to an orientation of 213° (NE-SW) with a mean rate of

change of + 0.28 °/day and an attenuation in summer 2019 (Figure 4.7d). From March 2020 to September 2020, it rotated clockwise from an orientation of 213° (NE-SW) to an orientation of 171° (N-S) with a mean rate of change of - 0.19 °/day (Figure 4.7e).

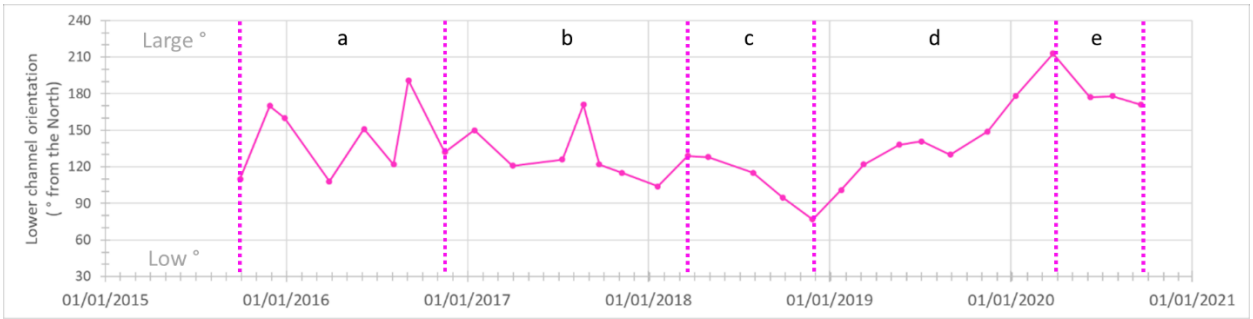

Figure 4.7 - Cacela lower ebb channel orientation evolution with its associated different periods (a,b,c,d,e) from September 2015 to September 2020

The ebb-tidal tip alongshore position showed a mean value of - 1 m along the timeframe, a mean rate of change of - 0.30 °/day between the images and maximum and minimum values of + 514 and - 301 (corresponding respectively to image 28 of March 2020 and image 20 of November 2018 in appendix 1)(statistic values in appendix 6). From its temporal evolution (Figure 4.8 with values in appendix 3 and change and rate of change values in appendix 4), a first period, from September 2015 to November 2016, was also characterized by a sawtooth evolution evolving from + 183 m to + 48 m with a mean rate of change of - 1. 03 m/day and maximum and minimum values of + 183 m in September 2015 and - 228 m in September 2016 respectively (Figure 4.8a). This highly variable evolution was characterized by short-term periods of 2 to 4 months marked by consecutives inverse shifts of this position (Figures 4.8a). From November 2016 to January 2018, the variation was attenuated, going from a value of - 50 m to a value of + 89 m with a mean rate of change of + 0.63 m/day and maximum and minimum values of + 89 m in January 2018 and - 143 in August 2017 (Figure 4.8b). From January 2018 to November 2018, the position migrated downdrift from a value of + 103 m to a value of + 514 m with a mean rate of change of + 1.70 m/day (Figure 4.8c). Then, from November 2018 to March 2020, it undergone a migration from + 514 m to - 301 m with a mean rate of change of - 1.77 m/day and an attenuation in summer 2019 (Figure 4.8d). From March 2020 to September 2020, it evolved from a position of - 301 m to a position of - 118 m with a mean rate of change of + 0.70 m/day (Figure 4.8e).

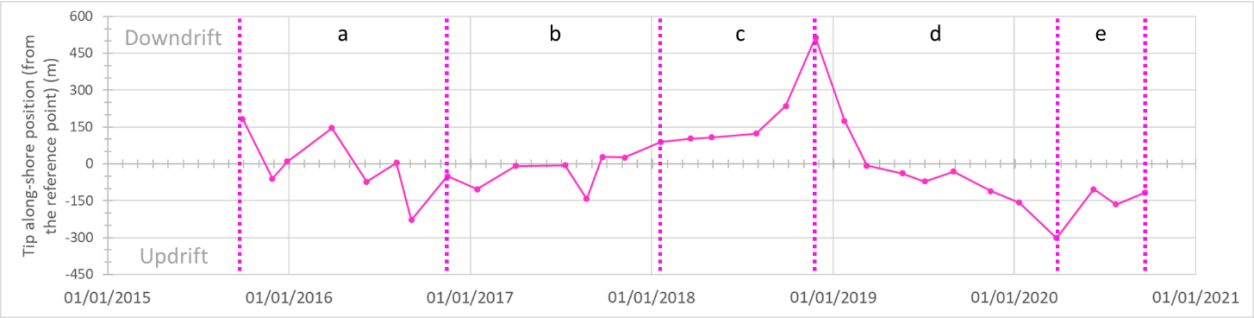

Figure 4.8 - Cacela ebb-tidal delta tip along-shore position evolution with its associated different periods (a,b,c,d,e) from September 2015 to September 2020

The ebb-tidal delta tip cross-shore migration showed too much variations along the timeframe to reveal any periods, trends, cyclicities or seasonality (Figure 4.9 with values in appendix 3 and change and rate of change values in appendix 4). Indeed, there is an unclear and inconstant sawtooth evolution ranging between cross-shore positions at - 135 m and - 244 m with a mean position at - 199 m and a mean rate of change of + 0.04 m/day (Figure 4.9)(statistic values in appendix 6).

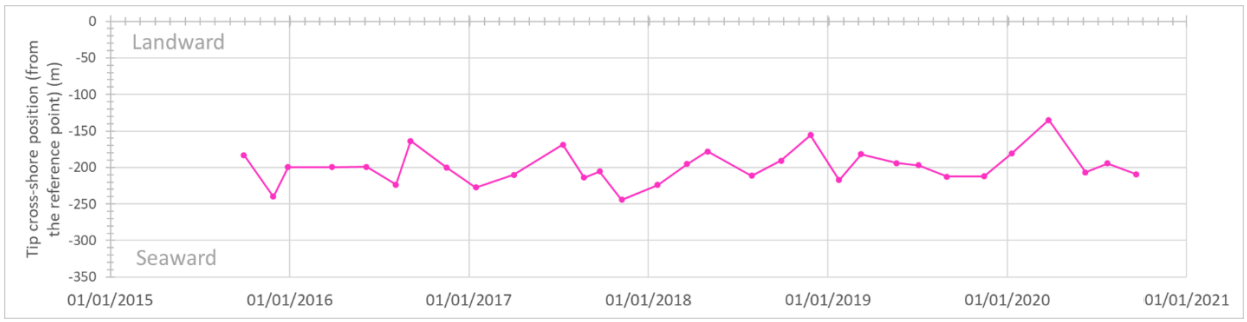

Figure 4.9 - Cacela ebb-tidal delta tip cross-shore position evolution from September 2015 to September 2020

4.3. Barriers and inlet

4.3.1. General morphology

By observing the envelope defined from the various limits of the barriers (Figure 4.10), an important variability of the development of these barriers close to the inlet was noticed. Indeed, the updrift barrier evolved more or less uniformly from a reduced spit, aligned with the mean orientation of the barriers, to a more elongated spit towards the North inside the basin. The downdrift barrier also showed a high variability but less uniform and important than the updrift one. It went from a reduced spit, aligned with the mean orientation of the barriers, to a less extended spit than the updrift barrier towards the interior of the basin or in the alignment of the

barriers. Thus, regarding this barriers' variability (Figure 4.10), the inlet defined by the extremity of the two barriers rotated/migrated, increased in length and decreased in width when it migrated towards the North inside the basin.

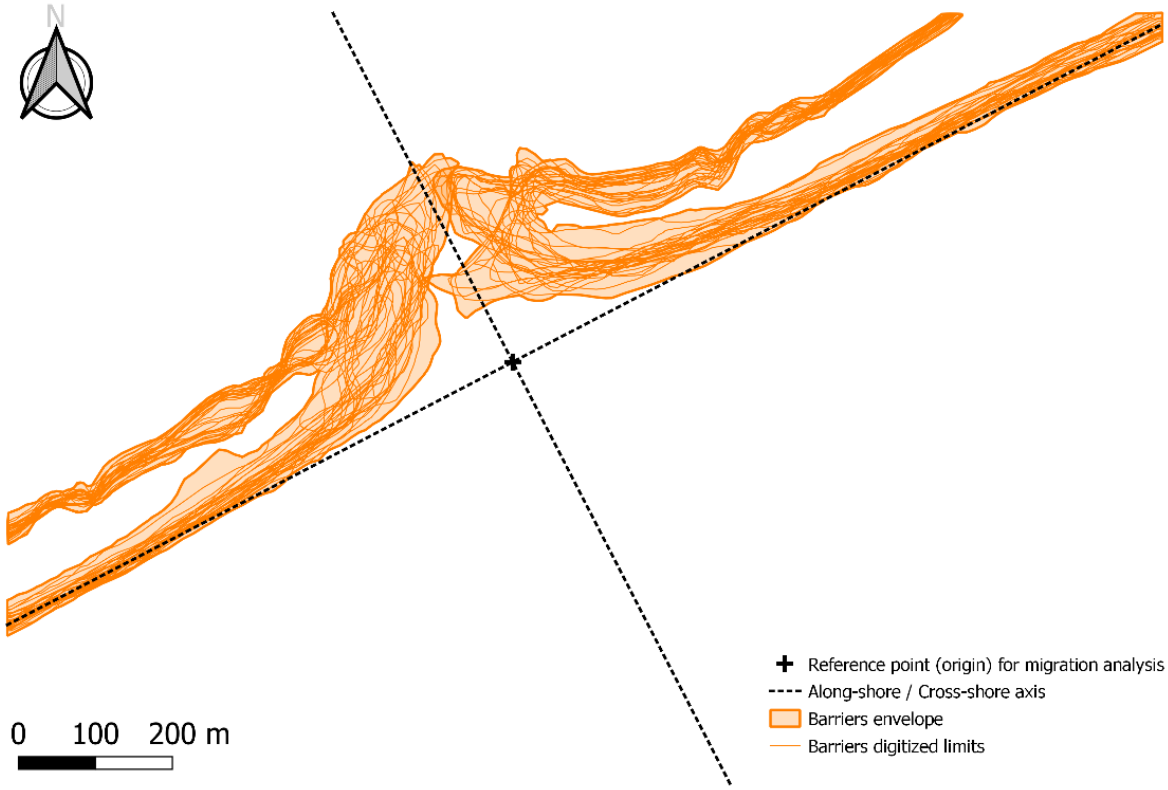

Figure 4.10 - Barriers' envelope and digitized limits (for all images) of Cacela-Cabanas system from September 2015 to September 2020

The envelope as well as the associated average positions and widths of the inlet were showing an inlet that remains relatively stable to its position but with a variable width (Figure 4.11). It was noticed that the minimum inlet widths were smaller and the segments they formed were oriented mostly W-E when they were landward while they became more important and oriented NE-SW (in the alignment with the barriers) seaward. The inlet rotated and reduced in size when it migrated towards the interior of the basin (Figure 4.11).

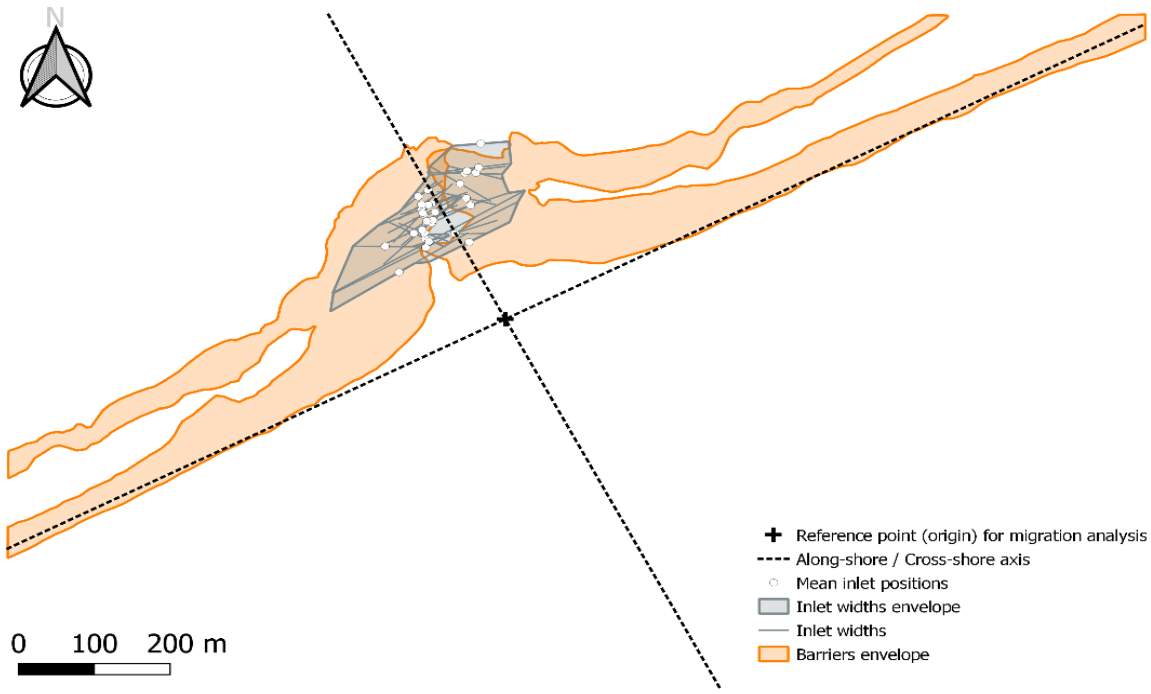

Figure 4.11 - Cacela inlet's envelope, widths and mean positions in Cacela-Cabanas system associated with barriers envelope from September 2015 to September 2020

4.3.2. Barriers general morphodynamics

The barriers limits, based on the morphological interpretation of the images of the appendix 1, revealed different development periods for the barriers. A first migration and extension of their extremities (particularly updrift) to the North (downdrift and landward migrations) inside the basin was clearly visible from September 2015 to June 2016 (images 1 to 5 in appendix 1). A second one, from June 2016 to January 2017 (images 5 to 9 in appendix 1) showed an inverse slight migration (updrift and seaward) of the extremities with barriers that tended to reduce (particularly in length for the downdrift one, and in width for the updrift one). Then, the barriers aggregated between January and April 2017 and the inlet rotated anticlockwise with downdrift barrier spit growing in the barriers mean orientation between April and July 2017 (images 9 to 11 in appendix 1). The updrift barrier spit decreased with a seaward migration from July to November 2017 to reach the main barriers orientation (NW-SE) and decreased even more until March 2018 associated with an important updrift migration of the inlet and a slight reduction of the downdrift barrier spit (images 11 to 16 in appendix 1). From this period began a period of recovery for the barriers (images 16 to 23 in appendix 1) where they grew, especially updrift. The recovery seemed

to end in May 2019 where they stopped their migrations but still grew both with a kind of equilibrium for the rest of the timeframe (images 23 to 31 in appendix 1).

4.3.3. Inlet morphodynamics

The mean inlet alongshore position at inlet showed a mean value of - 5 m along the timeframe, a mean rate of change of + 0.01 m/day between the images, and maximum and minimum values of + 92 m and - 92 m (corresponding respectively to images 15 of January 2018 and 5 of June 2016 in appendix 1)(statistic values in appendix 6). From its temporal evolution (Figure 4.12 with values in appendix 3 and change and rate of change values in appendix 4), a first trend was observed from September 2015 to June 2016 with a position that migrated downdrift from + 11 m to + 92 m with a mean rate of change of + 0.44 m/day (Figure 4.12a). From June 2016 to January 2018, it migrated updrift from a position at + 92 m to a position at - 92 m with a mean rate of change of - 0.30 m/day (Figure 4.12b). Then, it migrated downdrift again from January 2018 to March 2019 from a position at - 92 m to a position at 0 m with a mean rate of change of + 0.18 m/day and a notable jump of + 56 m from January to March 2018 (Figure 4.12c). From September 2018 to September 2020, it showed no notable variations, going from a position at 0 m to a position at - 1 m with a mean rate of change of + 0.04 m/day (Figure 4.12d).

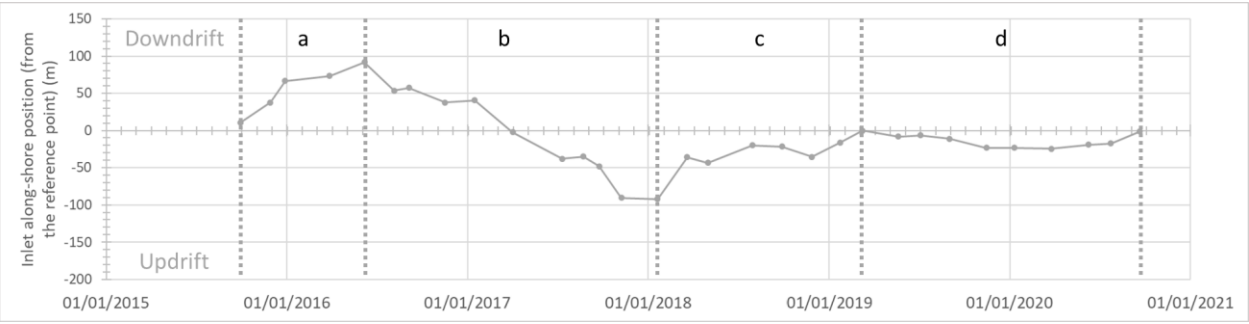

Figure 4.12 - Cacela mean inlet along-shore position evolution with its associated different periods (a,b,c,d) from September 2015 to September 2020

The mean inlet cross-shore position at inlet showed a mean value of + 182 m along the timeframe, a mean rate of change of + 0.08 m/day between the images, and maximum and minimum values of + 246 m and + 124 m (corresponding respectively to images 5 of June 2016 and 15 of January 2018 in appendix 1)(statistic values in appendix 6). From its temporal evolution (Figure 4.13 with values in appendix 3 and change and rate of change values in appendix 4), a first trend was

observed from September 2015 to June 2016 with a position that migrated landward from a position at + 124 m to a position at + 246 m with a mean rate of change of + 0.65 m/day (Figure 4.13a). From June 2016 to January 2018, it migrated seaward from a position at + 246 m to a position at + 127 m with a mean rate of change of - 0.17 m/day and an attenuation in summer 2017 (Figure 4.13b). Then, from January 2018 to September 2020 it showed a slight landward migration from a position at + 127 m to a position at + 217 m with a mean rate of change of + 0.08 m/day (Figure 4.13c). During this last period, the upper channel cross-shore position at inlet showed a notable seasonality with a position that migrated landward from winter to summer and seaward from summer to winter (Figure 4.13c).

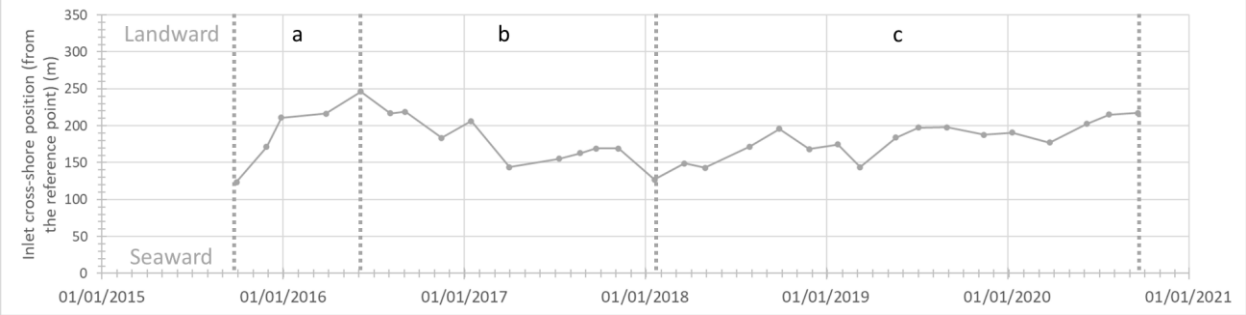

Figure 4.13 - Cacela mean inlet cross-shore position evolution with its associated different periods (a,b,c) from September 2015 to September 2020

The inlet width showed a mean value around 108 m, a mean rate of change of -0.03 m/day between images, and maximum and minimum at 295 m and 45 m (corresponding respectively to image 16 of March 2018 and image 31 of September 2020 in appendix 1)(statistic values in appendix 6). From its temporal evolution (Figure 4.14 with values in appendix 3 and change and rate of change values in appendix 4), a first trend was observed from September 2015 to November 2017 with a variable inlet that evolved from a width of 123 m to a width of 85 m with a mean rate of change of - 0.05 m/day (Figure 4.14a). From November 2017 to March 2018, an important opening was observed from a width of 85 m to a width of 295 m with a mean rate of change of + 1.56 m/day (Figure 4.14b). Then, from March 2018 to May 2019 it showed an important gradual reduction from a width of 295 m to a width of 60 m with a mean rate of change of - 0.45 m/day (Figure 4.14c). From May 2019 to January 2020, it started again to open from a width of 60 m to a width of 115 m with a mean rate of change of + 0.22 m/day (Figure 4.14d). A

reduction is observed from January 2020 to September 2020 evolving from a width of 115 m to a width of 45 m with a rate of change of - 0.27 m/day (Figure 4.14e).

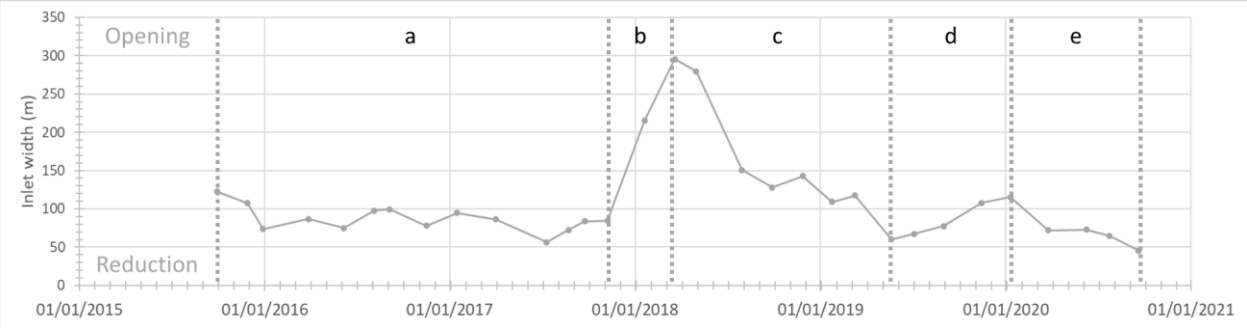

Figure 4.14 - Cacela mean inlet width evolution with its associated different periods (a,b,c,d,e) from September 2015 to September 2020

4.4. Integrated morphological evolution

From all those previous temporal evolutions and their associated defined periods, but also from the images' morphologic evolutions, five major periods were defined with quite coincident typical behaviors and changes observed from the overall studied parameters evolution (Figure 4.21).

The first period (period I), from September 2015 to June 2016, was characterized by a general downdrift and landward migration of most of the inlet features, mostly associated with barriers that grew and lengthened inside the basin. Indeed, they showed an unbalanced evolution to the North with an updrift barrier that lengthened more than the downdrift one, which increased more in width (orange arrow in Figure 4.15). Those barriers developments coincided with downdrift and landward migrations at the inlet (Figure 4.21a,b,c,f,g) that were observed for the previous defined periods of alongshore and cross-shore positions evolutions (as in period a of Figures 4.5, 4.6, 4.12 and 4.13). Indeed, the mean migrations of the channel position at inlet and the mean inlet positions showed rates of change respectively of + 0.33 m/day and + 0.44 m/day along-shore, and + 0.65 m/day and + 0.44 m/day cross-shore (Figure 4.21b,c,f,g with values in appendix 5). The upper ebb channel also showed a quite coincident anticlockwise rotation (as a subperiod of period a in Figure 4.4) with a rate of change of + 0.08 °/day during period I (Figure 4.21a with values in appendix 5). At the same time, a clear downdrift and landward migration of the shoals was also observed and associated to this unbalanced development of the barriers (red dashed circles in Figure 4.15). Then, the lower channel undergone several shifts during this period (pink arrows in

Figure 4.15) regarding its orientation associated with the alongshore tip migration (Figure 4.21d-e) and representing a first subperiod of period a in Figure 4.7 and 4.8. Moreover, the inlet width did not show typical behavior (Figure 4.21h) as it was observed in period a of Figure 4.14.

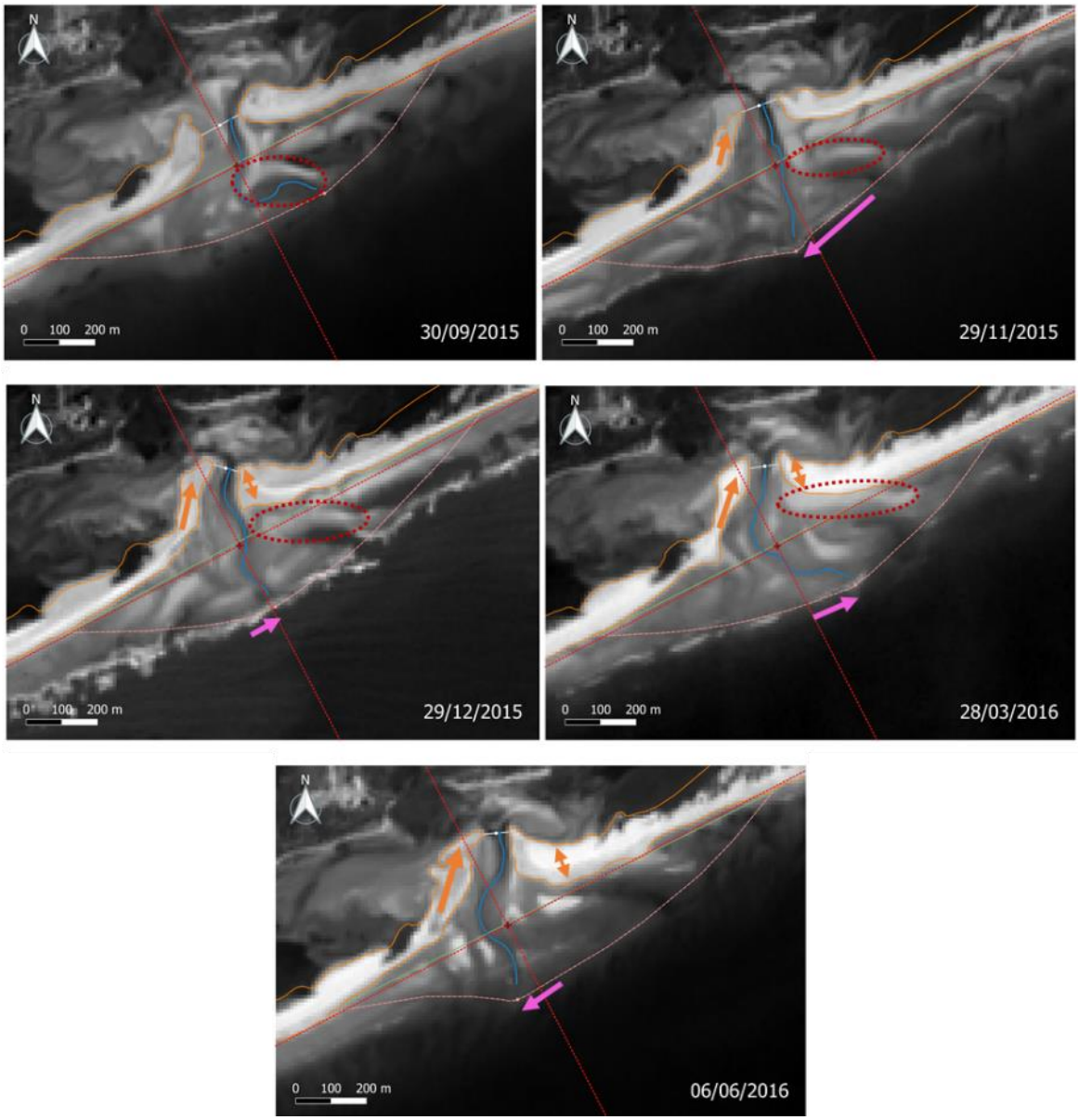

Figure 4.15 - Schematic representation of the changes observed for period I (orange arrow: barrier growing, pink arrow: lower channel rotation / tip migration, red dashed circle: approximate shoal position and extension)

The period II from June 2016 to January 2017, was characterized by various parameters showing an inlet system that stood inside the basin, associated with a slight migration inversion (updrift and seaward) for most of the parameters. Indeed, this period showed an updrift barrier that decreased slightly in length and mostly in width, while the downdrift one decreased slightly in

length and increased in width (orange arrows for increase and triangles for reduction/erosion in Figure 4.16). It coincided again with the change in the evolutions of the positions at inlet showing an inverse slight updrift and seaward migrations (as in periods b of Figures 4.5, 4.6, 4.12 and 4.13). Indeed, the mean migrations of the channel position at inlet and the mean inlet position showed rates of change respectively of - 0.12 m/day and - 0.18 m/day alongshore, and - 0.20 m/day and - 0.13 m/day cross-shore during this period II (Figure 4.21b-c-f-g with values in appendix 5). Meanwhile, the upper ebb channel continued its slight anticlockwise rotation (as in period a of Figure 4.4) but with a lower mean rate of change of + 0.02 °/day during this period II (Figure 4.21a with value appendix 5). Moreover, shoals continued also to form and migrate landward and downdrift (red dashed circles in Figure 4.16). Regarding the lower ebb channel, its variable shifts happening in periods a of Figures 4.7 and 4.8 were still observed as period II represented its second subpart, even though it seemed to shift more on the outer ebb-tidal delta (pink arrows in Figure 4.16). The inlet width still did not show particular behavior (Figure 4.21h), showing also highly variable and without clear evolutions all along the period a of Figure 4.14.

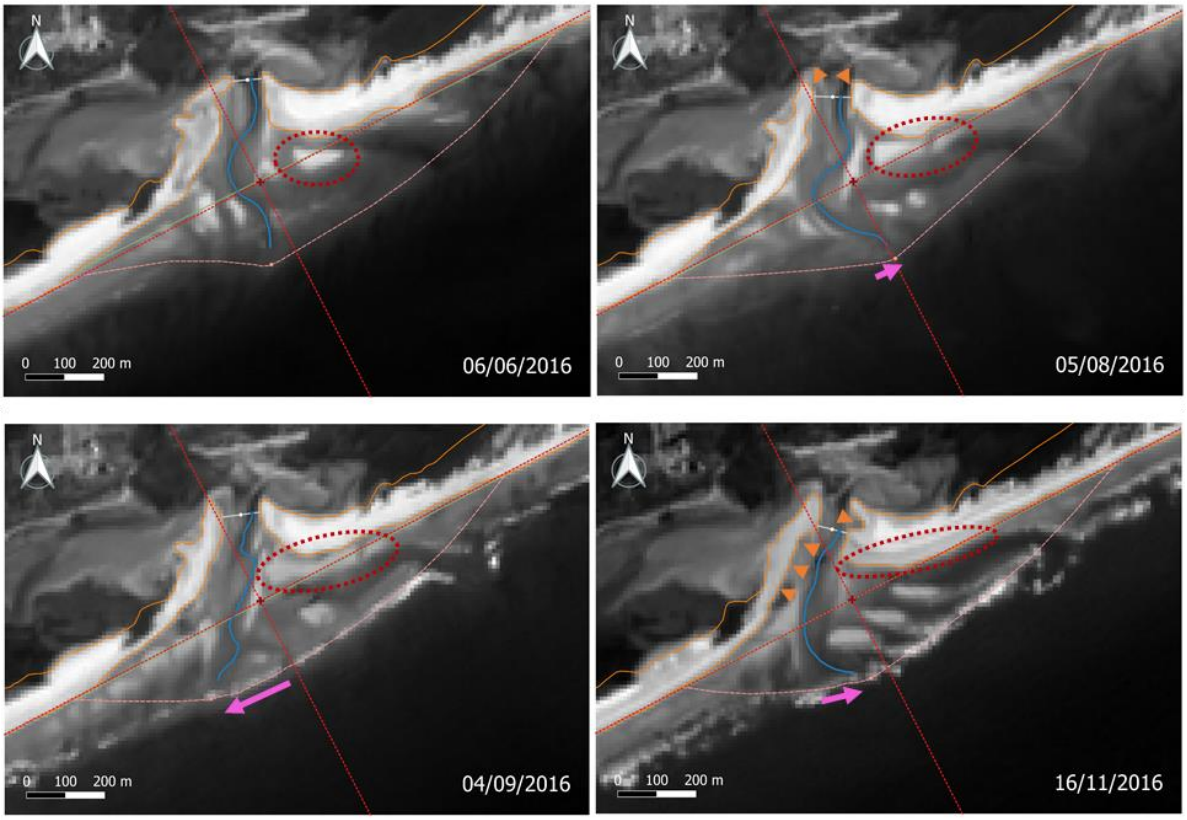

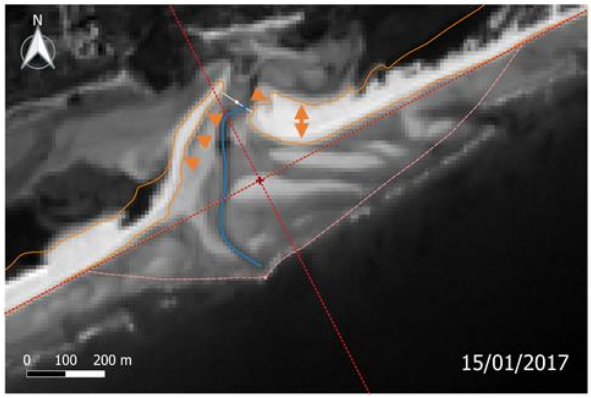

Figure 4.16 - Schematic representation of the changes observed for period II (orange arrow: barrier growing, orange triangle: barrier erosion, pink arrow: lower channel rotation / tip migration, red dashed circle: approximate shoal position and extension)

The period III, from January 2017 to January 2018, was characterized by an important updrift and seaward migration of the inlet system associated with an unusually observed circular ebb channel. During this period, the barriers migrated (orange arrows in the image of April 2017 in Figure 4.17) then reduced (orange triangles in Figure 4.17) until they reached their main barrier alignment. This reduction was mainly observed for the updrift barrier and associated to the circular ebb channel orientated toward updrift side from July 2017. At this time, the inlet seemed to be tilted updrift with the updrift barrier and the downdrift one lengthened to an offset position in the alignment of the barriers (orange arrows in the image of July 2017 in Figure 4.17). This unbalanced reduction of the barriers coincided with the updrift and seaward migrations that continued at inlet with a larger rate of alongshore migration and a lower rate of cross-shore one compared to the previous period II. Indeed, the mean migrations of the channel position at inlet and the mean inlet position showed rates of change respectively of - 0.54 m/day and - 0.37 m/day alongshore and of - 0.15 m/day and - 0.15 m/day cross-shore during this period III (Figure 4.21b-c-f-g with values in appendix 5). Furthermore, this reduction of the barrier is associated with an inverse clockwise rotation of the upper ebb channel with a rate of change of - 0.10 °/day during period III (Figure 4.21a with value in appendix 5). During this period, the ebb channel undergone also less migration and shifting (pink arrows in Figure 4.17) regarding its orientation associated with the alongshore tip migration (Figure 4.21d-e) as it was observed in periods b of Figure 4.7 and 4.8. The landward migration of the shoals was not visible anymore for period III (Figure 4.17). The inlet width started to show less variations with a mean rate of change of + 0.35 m/day for period III (Figure 4.21h with value in appendix 5) and an important opening of + 130 m (Figure

4.21h with value in appendix 4) between November 2017 and January 2018, at the end of the period (as it was also observed in period b of Figure 4.14).

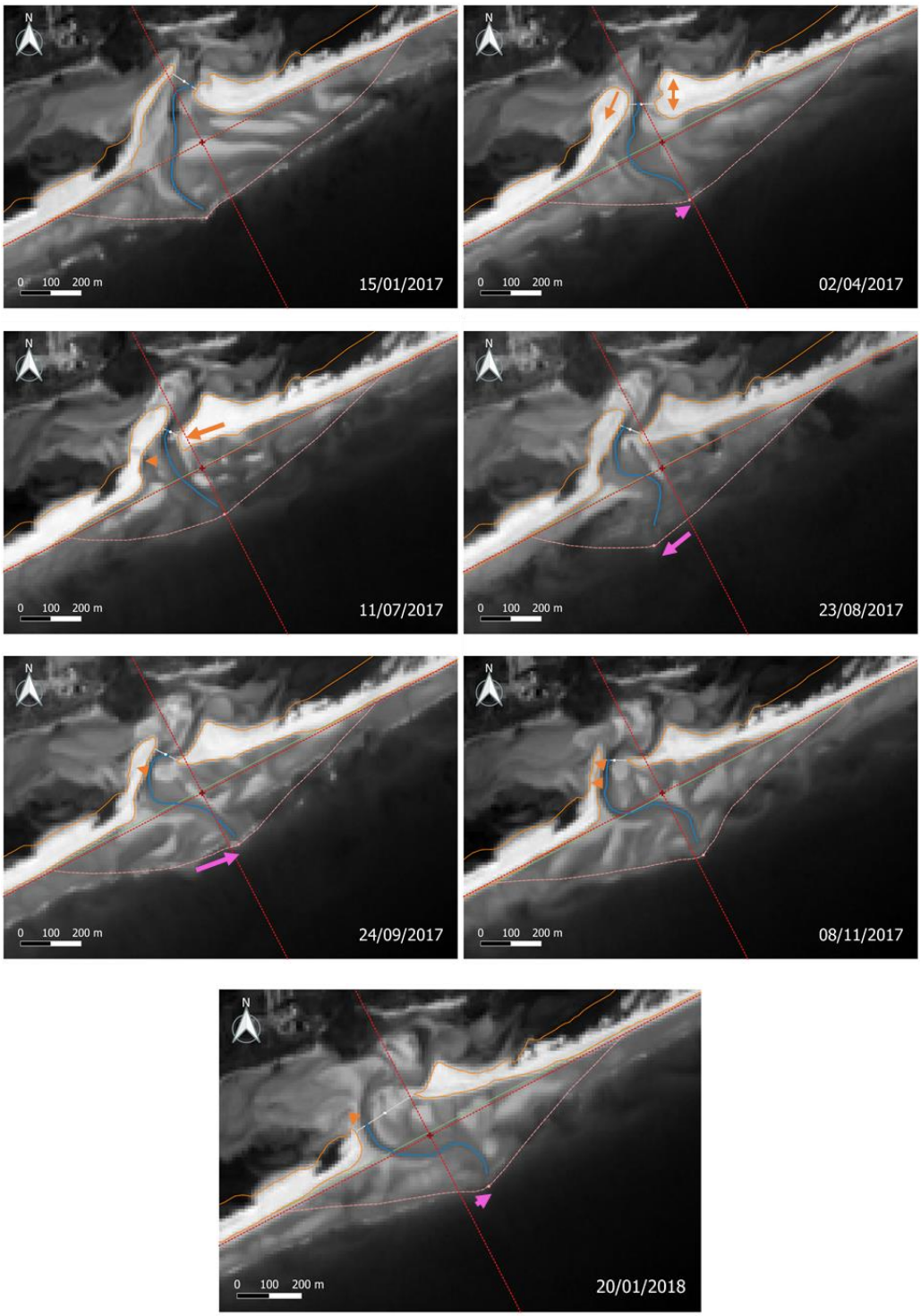

Figure 4.17 - Schematic representation of the changes observed for period III (orange arrow: barrier growing, orange triangle: barrier erosion, pink arrow: lower channel rotation / tip migration)

The period J (for "Jump"), from January to March 2018, was marked as a new period as several notable changes were observed in the studied parameters during this short time interval, especially at the inlet. This period showed reductions of the width of the updrift barrier and the spit of the downdrift one (orange triangles in Figure 4.18). All the shoals seemed to have been pushed downdrift and landward, mostly inside the inlet, leading to an inlet composed by important shoals and developed spit platforms (Figure 4.18). Moreover, it showed an ebb channel position at inlet and a mean inlet position that migrated drastically downdrift and quite landward (as it was observed in Figure 30b-e and at the beginning of period c in Figures 4.5 and 4.12 with downdrift jumps of + 118 m and + 56 m respectively regarding ebb channel and inlet) to a centered position and straight NW-SE ebb channel orientation (appendix 2) inside the inlet and across the ebb-tidal delta (blue arrow in Figure 4.18). Regarding the cross-shore positions, they slightly jumped landward with values of + 28 m for the ebb-channel position at inlet and + 22 m for the mean inlet position (Figure 4.21c-g with values in appendix 4). Moreover, the inlet width undergone a notable change of + 80 m during this period (Figure 4.21h with value in appendix 4).

Then, this period J was followed by another small period S (for "Standing"), with no notable change observed in most of the parameters (Figure 4.21) and a system that stood almost with the same morphology until May 2018 with a very slight recovery of the barriers and the shoals (Figure 4.18).

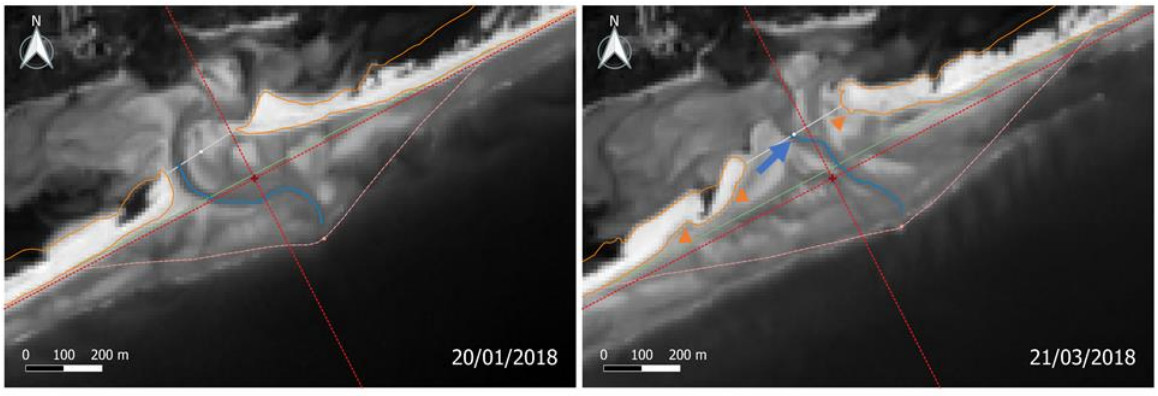

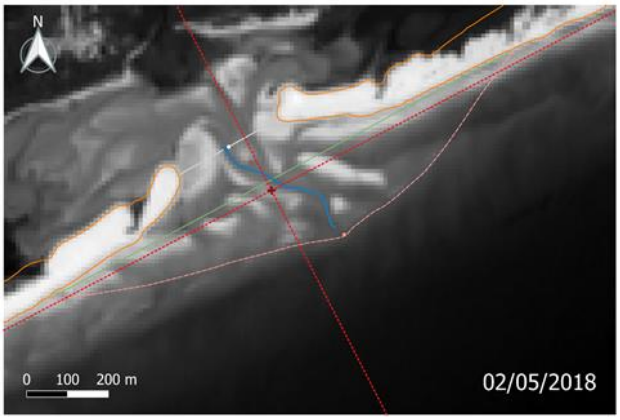

Figure 4.18 - Schematic representation of the changes observed for periods J and S (orange arrow: barrier growing, orange triangle: barrier erosion, blue arrow: upper channel shift)

Afterwards, the period IV was characterized as a period of stabilization for the system from May 2018 to May 2019 where most of the parameters varied to finally reach a certain stability associated sometimes with a trend and/or a seasonality (Figure 4.21). Indeed, the barriers seemed to have drastically recovered from May to July 2018 and continued to slightly recover until March 2019 (orange arrows in Figure 4.19). This evolution coincided with inlet width that reduced drastically from May to July 2018, then slightly until March 2019, with a mean rate of change of - 0.46 m/day (Figure 4.21h with value in appendix 5). The along-shore position of the channel at the inlet varied from a position to the downdrift side of the inlet to position on the updrift side, and finally almost merged with the mean inlet position in May 2019 (Figure 4.19) associated with the inlet width reduction (Figure 4.21b-f-h). The upper ebb channel orientation rotated anticlockwise until November 2018 and stood meanly around 174° (N-S) until May 2019 (appendix 2) with a mean rate of change of + 0.10 °/day for the period IV (Figure 4.21a with value in appendix 5). The lower ebb channel rotated clockwise until November 2018 (reaching its timeframe minimum value of 77°) then anticlockwise until May 2019 (pink arrows in Figure 4.19 observed also for period c and d until May 2019 in Figures 4.7 and 4.8) with a mean rate of change of + 0.05 °/day (Figure 4.21d with value in appendix 5). The landward migration of the shoals was once again quite visible but more difficult to analyzed than the previous periods due to the highly deflected lower ebb channel.

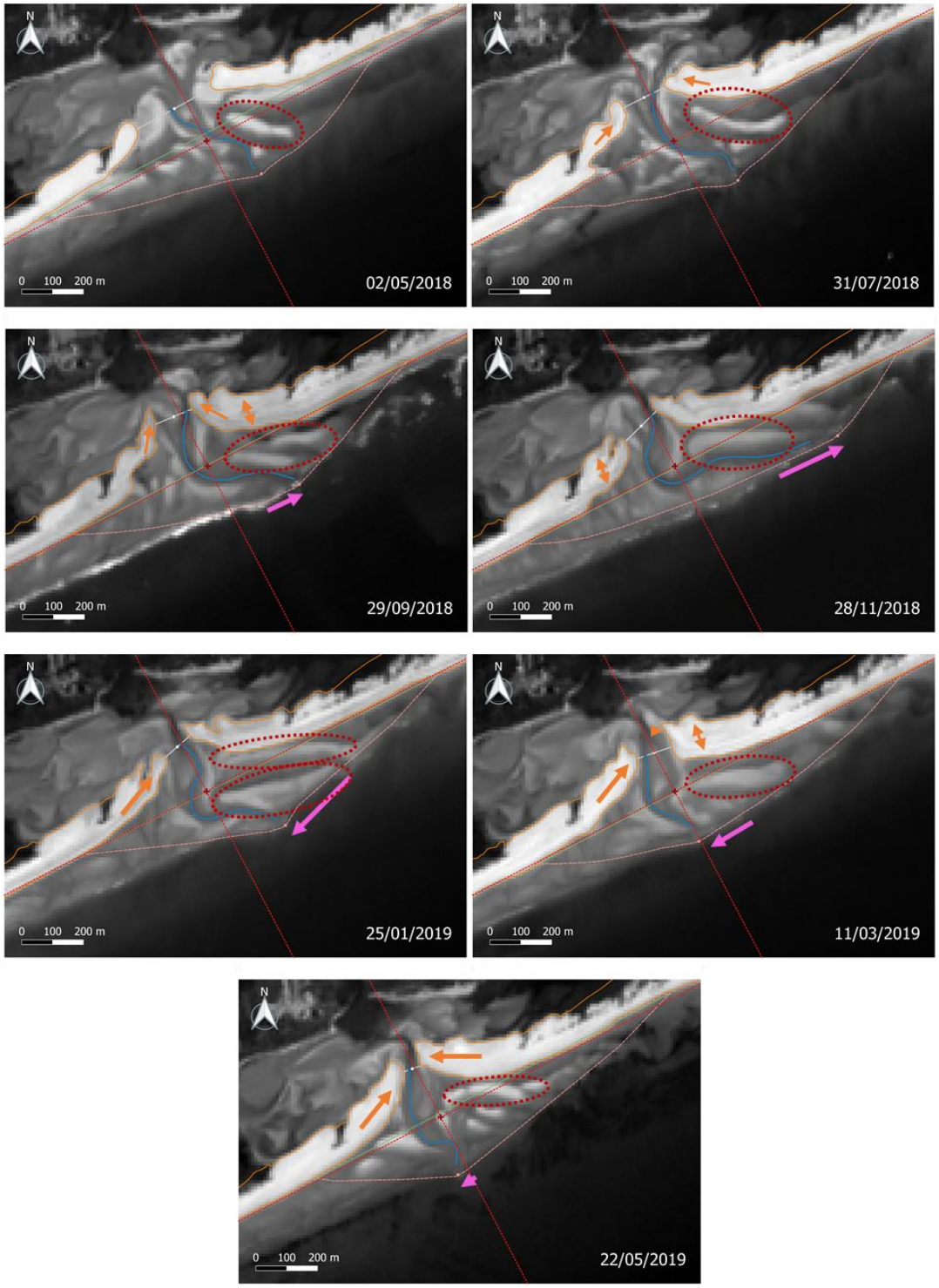

Figure 4.19 - Schematic representation of the changes observed for period IV (orange arrow: barrier growing, orange triangle: barrier erosion, pink arrow: lower channel rotation / tip migration, red dashed circle: approximate shoal position and extension)

For the rest of the time frame, from May 2019 to September 2020 (period V), the system seemed to be in a certain equilibrium with barriers that evolved more uniformly and quite proportionally

from each other, giving a landward hoof shape to the spits that seem to be in equilibrium with the ebb channel (e.g., last image September 2020 in Figure 4.20). They seemed to present a seasonality with an inlet width that grows until January 2020 then reduces after (Figure 4.21h). A cross-shore seasonality was also visible during this period but shows also a very slight landward migration trend of + 0.09 m/day (Figure 4.21c-g with values in appendix 5). During this period V, the inlet showed an almost fixed mean along-shore position as well as the ebb channel position at inlet, meaning that the upper ebb channel now remains in the center of the inlet (Figures 4.20 and 4.21). Moreover, the upper channel orientation stood in a N-S orientation for this period with a mean rate of change of + 0.02 °/day (Figure 4.21a with value in appendix 5). The lower ebb channel continued its anticlockwise rotation until March 2020 (reaching its timeframe maximum value of 213°) to finally rotated clockwise and stand in a N-S orientation (pink arrows in Figure 4.20) with a mean rate of change of + 0.12 °/day for the period V (Figure 4.21d with value in appendix 5). The shoal's landward migration was visible with a clear shoal's development seasonality (better developed in winter and scattered in summer due to ebb-tidal)(red quadruple arrows in Figure 4.20).

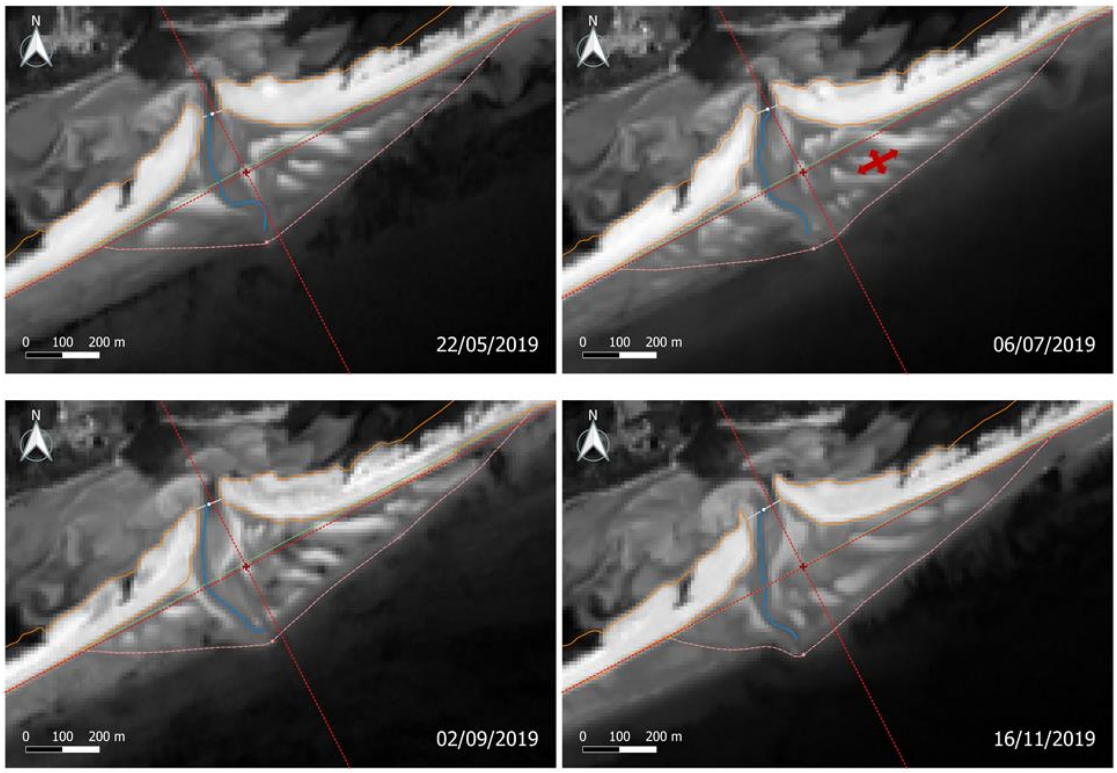

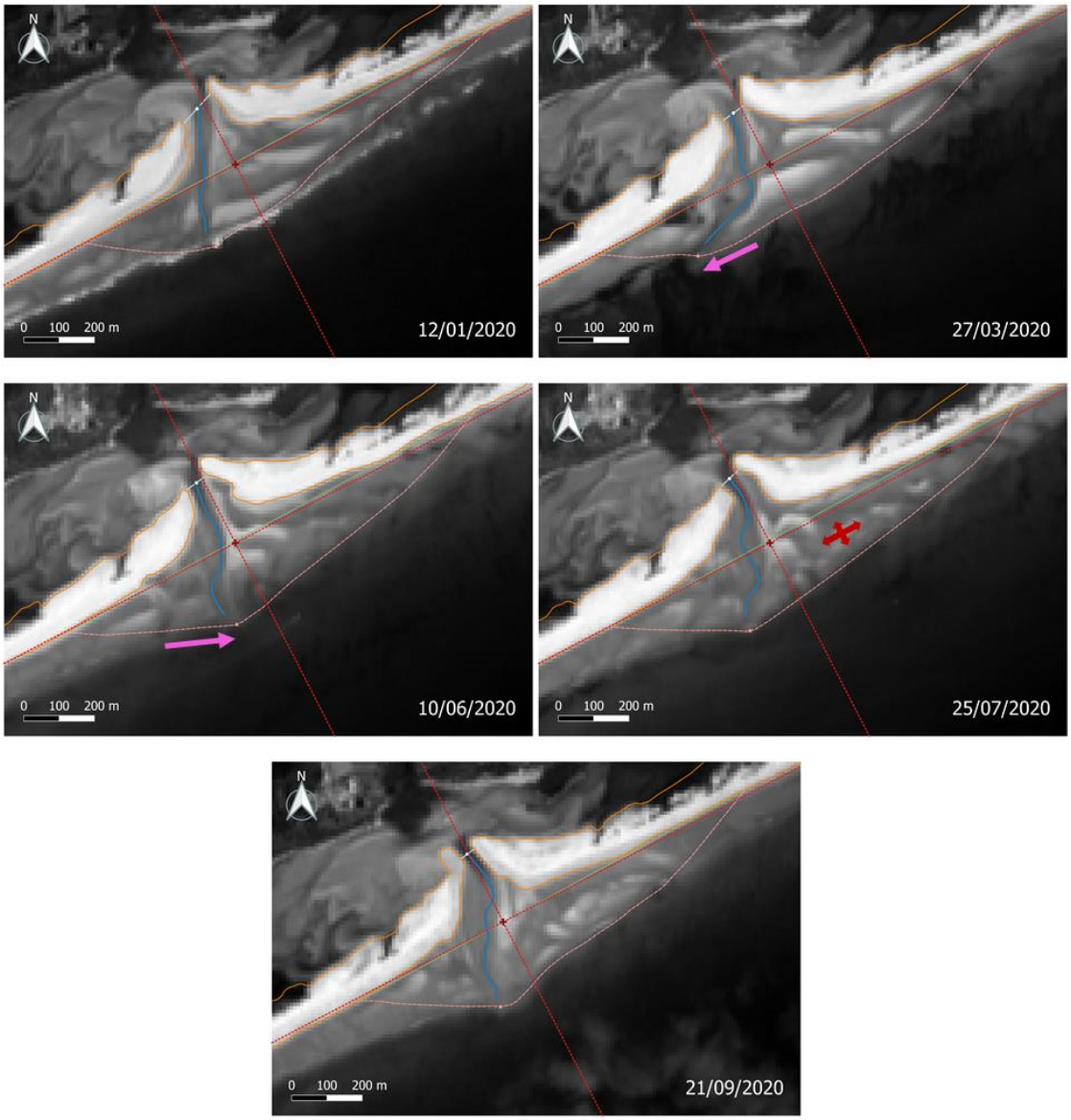

Figure 4.20 - Schematic representation of the changes observed for period V (pink arrow: lower channel rotation / tip migration, red quadruple arrows: shoals disruption)

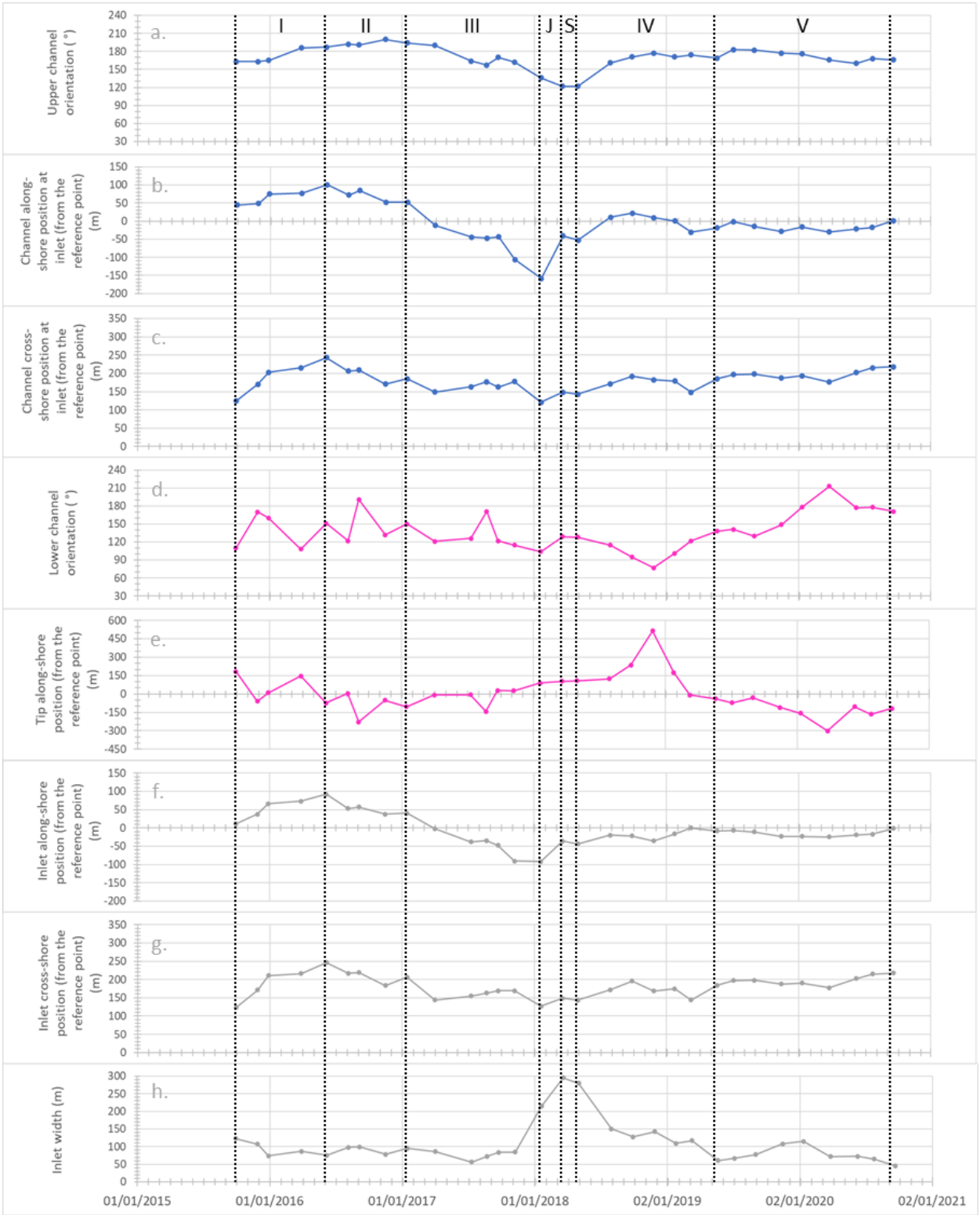

Figure 4.21 - Bundle of the different quantified parameters evolution from September 2015 to September 2020 delimited by the periods of interest (I,II,III,J,S,IV,V)

4.5. Hydrodynamic conditions

Regarding the wave conditions, the time series showed a Hs ranging from 0.02 m to 5.12 m with a mean of 0.60 m (appendix 9) and an important seasonality with waves generally higher in winter (October-March) (Figures 4.22 and 4.23). The Tp ranges from 1.80 s to 25.97 s with an average of 6.23 s (appendix 9). θ values showed a mean value of 195° (N-S)(appendix 9).

Among these wave data, there was an occurrence of nearly 59% from the West (mostly SW with a mean θ value of 244° in appendix 9) and 41% from the East (mostly SE with a mean θ value of 123° in appendix 9) from 2015 to 2020. This western wave major occurrence was observed regarding the proportion of hours of western and eastern waves between the images (Figure 4.24 with values in appendix 7). The Eastern conditions had a significant wave height between 0.02 and 3.99 m averaged around 0.73 m and a peak period between 1.80 s and 23.61 s averaged around 5.78 s (Figure 4.22 with statistic values in appendix 9). The conditions from the West had a significant wave height between 0.02 m and 5.12 m averaged around 0.51 m and a peak period between 1.80 s and 25.97 s averaged around 6.53 s (Figure 4.23 with statistic values in appendix 9).

Eastern waves were mostly comprised between 0.5 m and 1.5 m height and showed very high heights for some periods (e.g., May to July 2017), while western ones seemed to be dominated by waves below 0.5 m and showed very high values during some episodes (e.g., January to March 2018 marked by Emma storm that happened at the end of February and beginning of March 2019)(Figures 4.22 and 4.23).

Three important peaks of wave heights higher than 2.5 m were noted and considered as notable storms from Figures 4.22 and 4.23. The first one came from the East and reached a maximum of 3.99 m in April 2017 (Figure 4.22). The second, and highest one (representing Emma storm), came from the West and reached a maximum height of 5.12 m in March 2018 (Figure 4.23). The lasts one came from the West and reached a maximum height of 4.36 m in December 2019 (Figure 4.23).

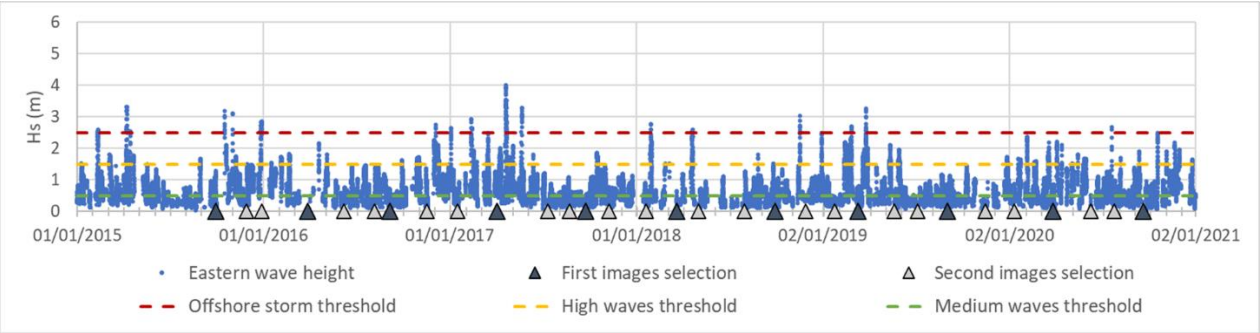

Figure 4.22 - Significant eastern wave height (Hs) off Cacela-Cabanas system from 2015 to 2020 associated with the selected images markers and the study area storm threshold

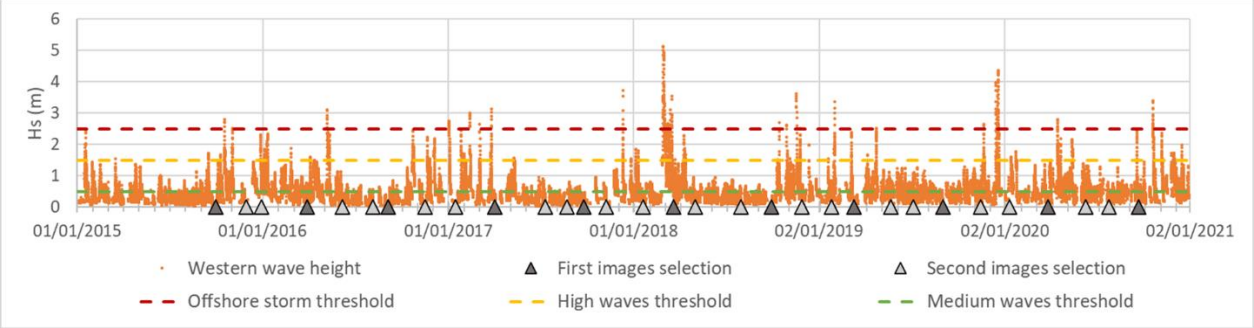

Figure 4.23 - Significant western wave height (Hs) off Cacela-Cabanas system from 2015 to 2020 associated with the selected images markers and the study area storm threshold

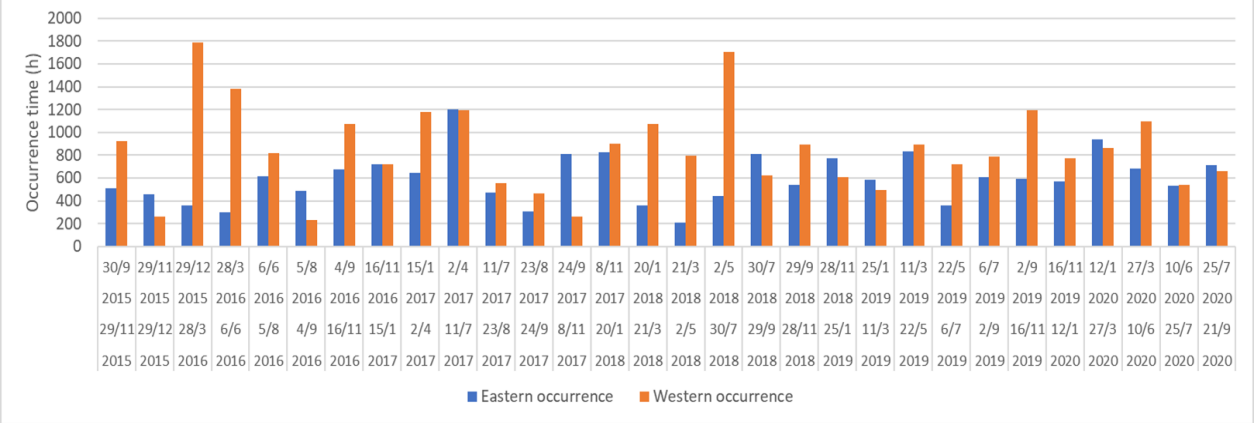

Figure 4.24 - Number of hours of eastern or western occurrence between the selected images off Cacela-Cabanas system from September 2015 to September 2020

From these wave height data and their associated peak periods, the wave power was computed for the entire time frame (Figures 4.25 and 4.26) depicting in a more visible way the periods that could impact the Cacela inlet and ebb-tidal delta. There was a strong and clear seasonality with larger power in winter, and three important peaks were notes as previously, showing respectively maximum powers of 1.60 x10^5 W/m, 2.87 x10^5 W/m and 1.87 x10^5 W/m (Figures 4.25 and 4.26).

Some other smaller peaks that were generally briefer were also observed from Figures 4.25 and 4.26. Most of those peaks of significant P were detached from the overall (low) wave power behavior and mostly represented single independent events, particularly western ones (Figures 4.25 and 4.26).

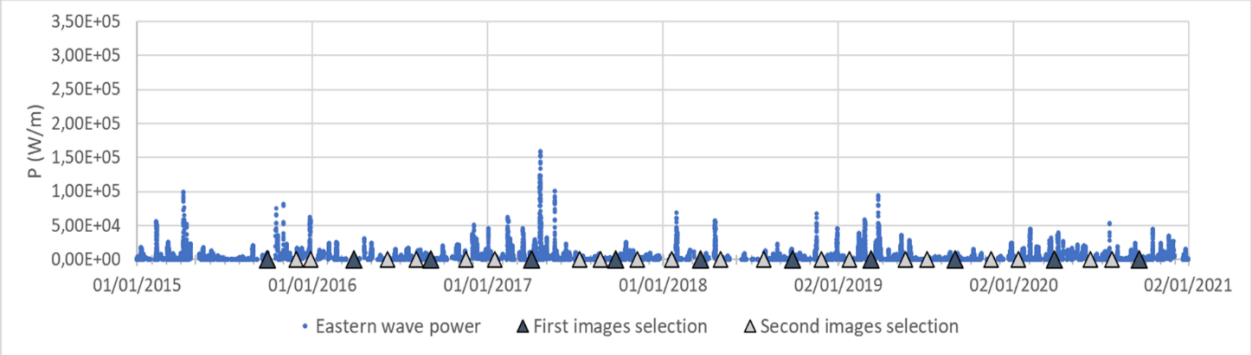

Figure 4.25 - Eastern wave power off Cacela-Cabanas system from 2015 to 2020 associated with the selected images markers

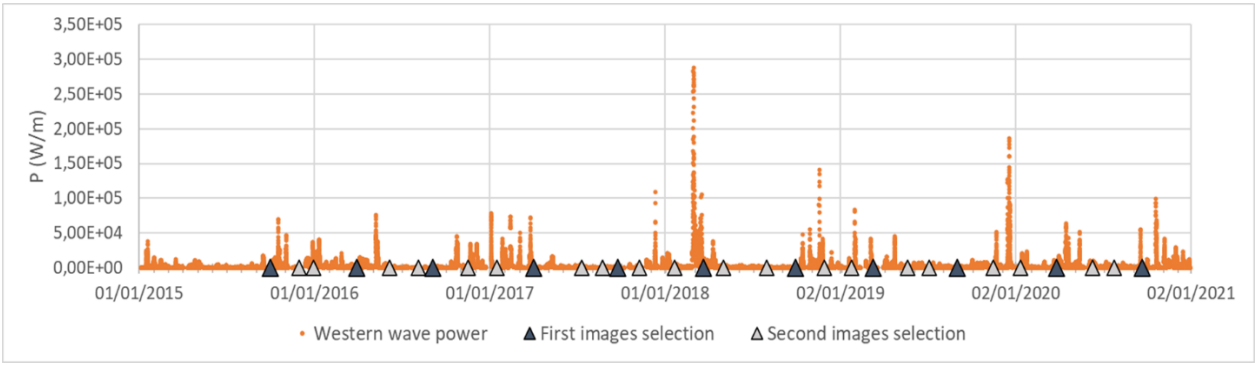

Figure 4.26 - Western wave power off Cacela-Cabanas system from 2015 to 2020 associated with the selected images markers

The cumulative wave power between the selected images (Figure 4.27 with values in appendix 7) provided information on the direction and total power of the waves that the system has experienced between two images with known hydrological and morphological characteristics. This total power was dominated either by large wave power over short powerful periods like storms (such from January to March 2018 in Figure 4.27 marked by the very powerful waves of Emma storm from the West) or by a multitude of medium wave power values dominating over one direction during longer periods (such as from January 2019 to March 2019 in Figure 4.27 where eastern Pc was higher than western while their independent events showed almost the same P but not during the same period in Figures 4.25 and 4.26).

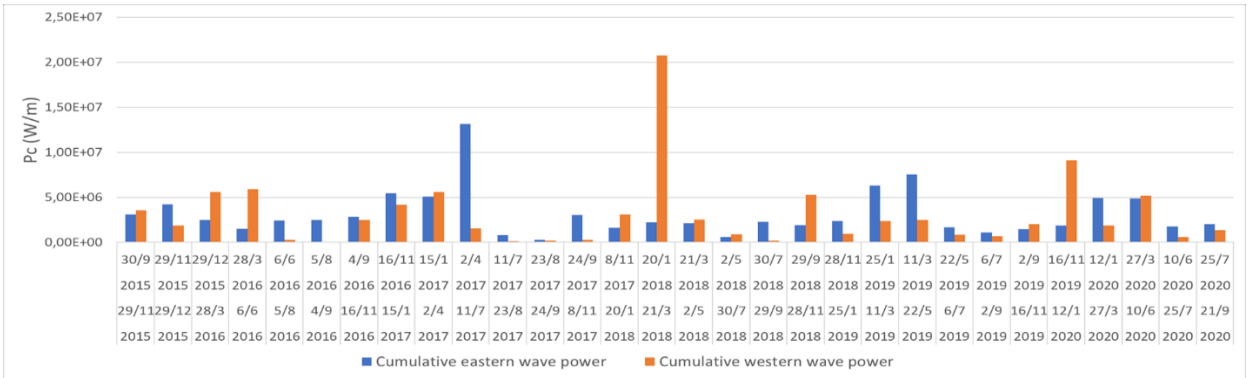

Figure 4.27 - Cumulative wave power between the selected images off Cacela-Cabanas system from September 2015 to September 2020

Pch values (presented in Figure 4.28 with values in appendix 7) highlighted the facts that eastern waves were meanly more energetic than Western ones and that the latter showed variable powers sometime larger than Eastern ones during single events (as during between January and March 2018 marked by Emma storm). In fact, eastern waves showed a mean wave power of 5.14 x10^3 W/m while western waves showed a mean power of 3.34 x10^3 W/m (mean of 4.08 x10^3 W/m in total)(appendix 9). Eastern waves were dominant in term of Pch over most of the timeframe (higher bars between most of the images in Figure 4.28 with values in appendix 7).

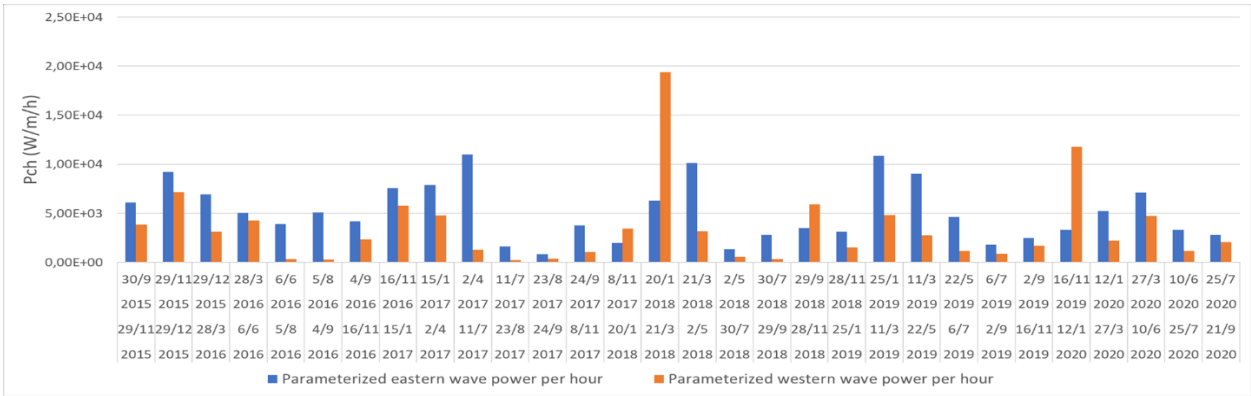

Figure 4.28 - Parameterized wave power per hour between the selected images off Cacela-Cabanas system from September 2015 to September 2020

Considering the previously defined periods of interest, the period I was characterized by mixed waves of notable Pch higher than most of the other periods of interest, particularly for western waves (Figure 4.29 with values in appendix 8). Those mixed waves were dominated by western occurrences in terms of number of hours (as in most of the periods)(Figures 4.30 with values in appendix 8) but they were quite dominated by eastern occurrences in terms of Pch (as in most of

the periods)(Figure 4.29 with values in appendix 8). Periods II and III shared almost the same Pch (Figure 4.29 with values in appendix 8) and number of hours (Figure 31 with values in appendix 8), with values of Pch dominated by eastern waves and lower than period I, and number of hours quite similar proportional regarding the two occurrences. Period J, marked my Emma western storm, showed an obvious dominance of western Pch for a small period dominated by western waves, while period S showed a dominance of eastern Pch for a small period also dominated by western waves (Figures 4.29 and 4.30 with values in appendix 8). Then, periods IV and V were characterized by the same proportionality in terms of number of hours of the occurrence origins. However, period IV showed a higher eastern Pch regarding its western Pch and period V, while the latter showed quite the same Pch according to waves origins (Figures 4.29 and 4.30 with values in appendix 8).

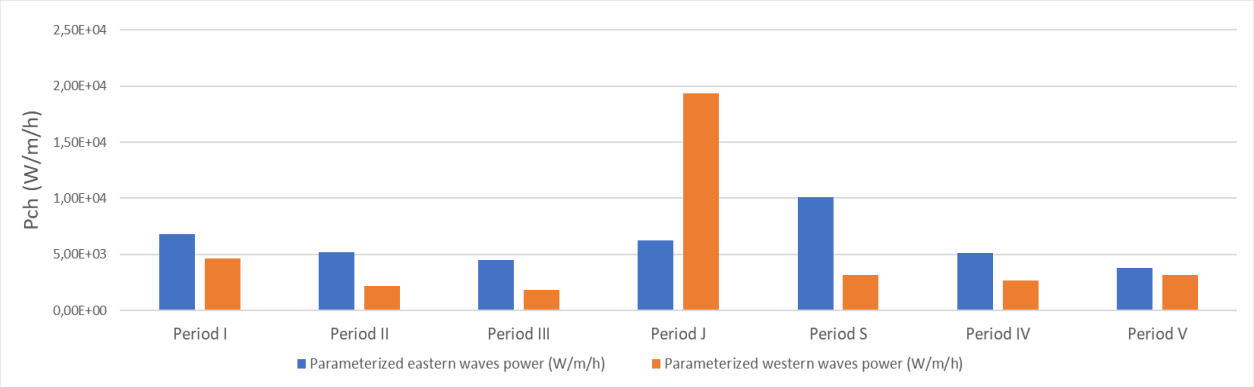

Figure 4.29 - Parameterized wave power per hour for the periods of interest (I,II,III,J,S,IV,V) off Cacela-Cabanas system from September 2015 to September 2020

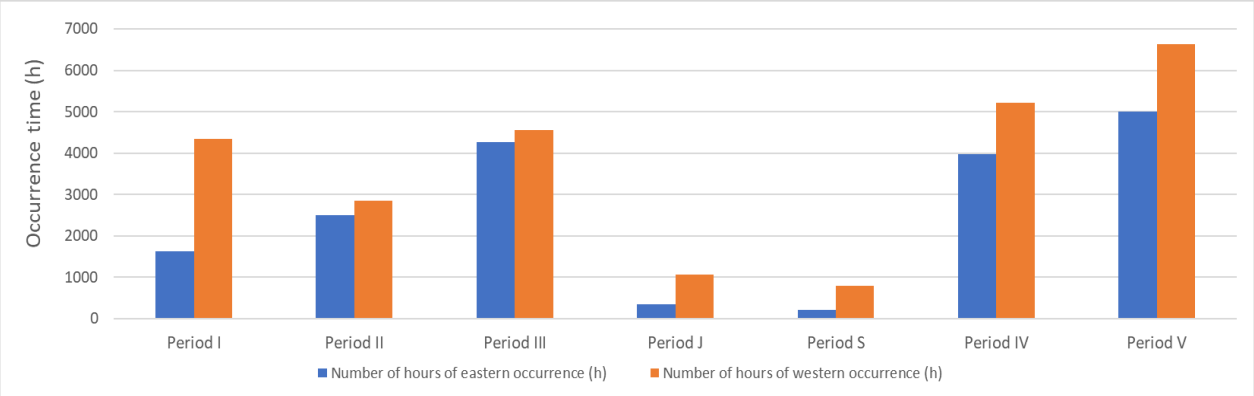

Figure 4.30 - Occurrence time in hours for the periods of interest off Cacela-Cabanas system from September 2015 to September 2020

5. Discussion

5.1. Cacela inlet and ebb-tidal delta system classification

The first general observation that can be made on Cacela inlet and ebb-tidal delta system is that the ebb-tidal delta appeared to be more developed (e.g., green arrow in Figure 5.1) than the flood-tidal delta (e.g., yellow arrow in Figure 5.1), indicating a notable tide influence on this system (Davis, 2013; Kraus, 2009). This larger size can be explained by the combination of littoral drift sediment trapping and ebb-tidal currents that could transport more sediments than flood ones and deposit them on the maritime front of the system where their velocity decrease (FitzGerald et al., 2011). Indeed, according to Kraus (2009), this tide influence can be characterized by a bypass dominated by tides in which sediments enter the upstream side of the channel during the flood tide and returns downstream during the ebb tide, keeping most of the sediment in the sea front of the inlet due to the tidal difference (Figure 2.4). Moreover, the almost constant presence of well-developed channel margin linear bars bordering the main ebb channel (e.g., dark blue dashed circles in Figure 5.1) supported this tidal influence in accordance with previous studies (Davis, 2013; Kraus, 2009). Those bars were mostly sub-perpendicular to the barriers close to the inlet and followed the ebb channel deflection on the ebb-tidal delta (Figure 4.1). They were due to the ebb-tidal currents, that most probably dominated over others currents, and formed where the velocity decreases on the sides of the confined ebb flow (where the sediment is able to settle)(FitzGerald et al., 2011).

Although tidal influence in Cacela ebb-tidal delta could be quite important, its morphology was also highly influenced by a mixed waves occurrence. Indeed, the ebb-tidal delta had a general shape more similar to a mixed energy morphology than a tide-dominated symmetric and elongated seaward morphology (Figures 2.2 and 2.4)(Kraus, 2009). Cacela ebb-tidal delta showed a general asymmetry with a longer downdrift side (e.g., light pink arrows in Figure 5.1) and downdrift shoals better developed (e.g., red dashed circle in Figure 5.1) in most of the images (Figures 4.1 and 4.3). According to FitzGerald (2000), it is on the updrift part of the ebb-tidal delta that the accumulation of sediment is preferential due to the longshore drift, causing a deflection of the ebb channel and giving an asymmetry to the ebb-tidal delta whose tip is rather directed towards the downdrift part (FitzGerald et al., 2011; Styles et al., 2016). In the case of Cacela ebb-

tidal delta, the dominant eastward longshore drift (Ferreira et al., 2016) was expressed through the higher presence of spit-shaped shoals on the updrift barrier than on the downdrift barrier (Figure 4.1b,c,d,e,g,h,i)(FitzGerald, 2000). However, even though the Cacela main ebb channel was generally deflected slightly downdrift (Figure 4.3), the expected downdrift asymmetry of the ebb-tidal delta, as described by Sha and Van den Berg (1993) and FitzGerald (2000), was rarely visible. In fact, this downdrift asymmetry was only clearly visible in September and November 2018 (images 19 and 20 in appendix 1) when the lower channel was highly deflected downdrift (Figures 4.7 and 4.8). The general updrift asymmetry of the Cacela ebb-tidal delta could be justified by the mixed waves regime, having different angles of incidence from the West (mostly SW) and the East (mostly SE)(subchapter 4.5.) facing the NE-SW Cacela-Cabanas system. Moreover, even though the occurrence of the waves was mixed (Figure 4.21), the waves from the East showed larger values of Pch almost all along the time frame (Figure 4.22). Thus, even though the system was characterized by a dominant eastward longshore drift, the ebb-tidal delta tip was mainly pushed updrift by the more powerful and sub perpendicular waves from the East, giving this general updrift asymmetry.

Finally, all those observations made on the morphology of the ebb-tidal delta have made it possible to characterize the Cacela inlet and ebb-tidal delta system in a general way as a system with mixed hydrological influences (tides and waves).

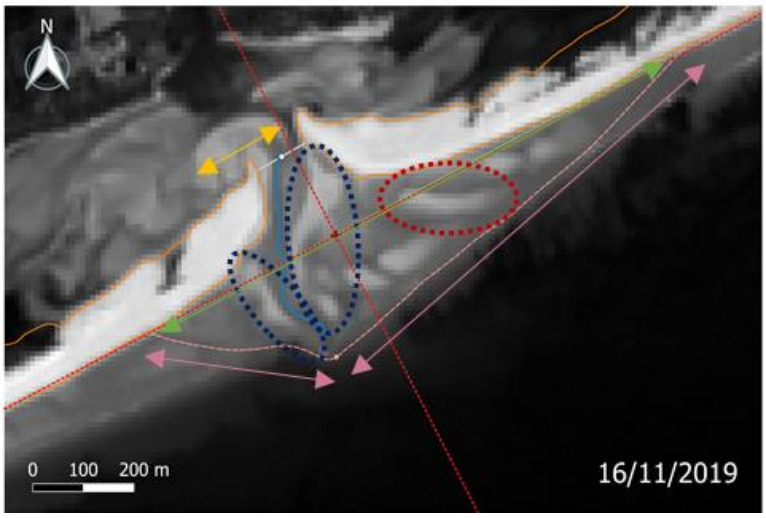

Figure 5.1 - Schematic representation of a typical example of the Cacela ebb-tidal delta general morphology (yellow arrows: flood-tidal delta width, green arrows: ebb-tidal delta width, light pink arrows: sides length of the ebb-tidal delta, dark blue dashed circles: channel margin linear bars, red dashed circles: swash bar)

5.2. Ebb-tidal delta morphodynamics

Cacela ebb-tidal delta showed several periods of shoal's formation, landward migration and attachment to the downdrift barrier (Figures 4.15, 4.16, 4.19 and 4.20). These downdrift shoals' formation and landward migration were generally described in FitzGerald bypass models "ebb-tidal breaching" / "outer channel shifting" (also called "outer delta breaching" by Lenstra, 2019) / "stable inlet" (2000)(Figure 2.5) as cycles between four and ten years of shoals growing and migrating to the barrier due to the wave's occurrence. The observations from the images in appendix 1 revealed shoals that formed and migrated almost all the year and reached the barrier almost in one year (e.g., Figures 4.2 and 5.2) and not in four to ten years as stated by FitzGerald (2000). However, this shorter period might come from the fact that the systems he studied were much larger than Cacela Inlet, involving longer ebb-tidal delta processes (e.g., Willapa Bay Inlet showing an approximate width of 9 km in Google Earth against a mean Cacela inlet width of 108m from September 2015 to September 2020). Moreover, the downdrift and landward shoals' migrations directions observed at Cacela ebb-tidal delta (happening during periods I, II, IV and V in 4.4.) were in accordance with the description of those models. Indeed, these migrations can be associated with the general eastward longshore transport (Ferreira et al., 2016) and with the mixed SW and SE waves angles of incidence. This combination of waves subparallel (SW) and subperpendicular (SE) to the barriers leads to shoals' migration with a mean direction almost to the North and thus toward the downdrift barrier (e.g., Figure 5.2). Furthermore, the shoals grew and migrated quite faster in winter and dispersed in small shoals across the ebb-tidal delta in summer (e.g., Figure 5.2). This seasonality was quite consistent with the seasonality associated with waves occurrence. In fact, it showed higher and more powerful waves in winter and lower and less powerful waves in summer (Figures 4.22, 4.23, 4.25 and 4.26). Those low summer wave conditions induce a tidal dominance on the ebb-tidal delta where ebb-tidal currents disrupt the well-developed winter bars (e.g., Figure 5.2).

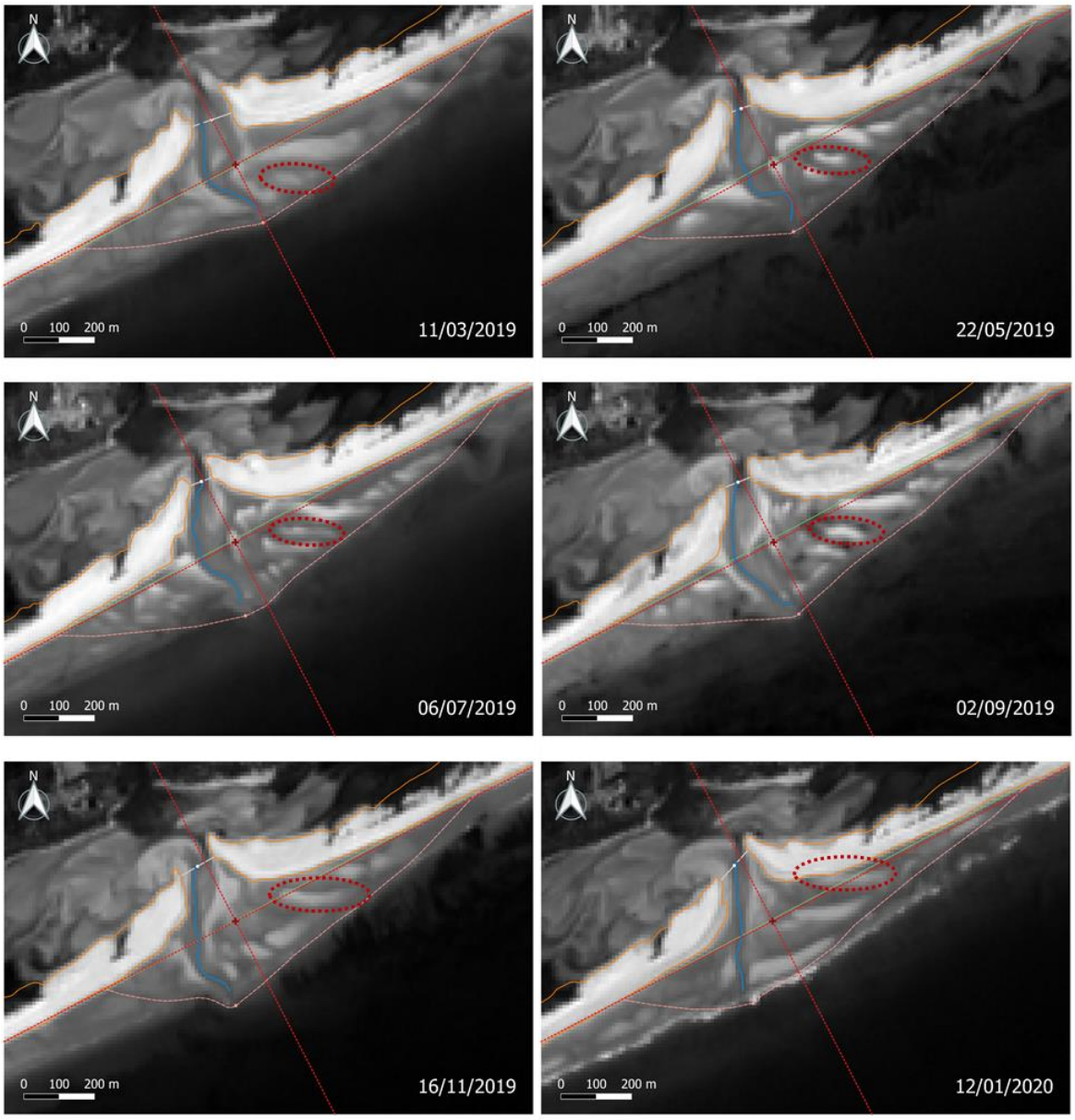

Figure 5.2 - Schematic representation of an example of shoals' seasonality and landward migration to the downdrift barrier (red dashed circles: approximate shoal position and extension)

According to the previous studies and models of FitzGerald et al. (2000) and Lenstra et al. (2019), the shoals/channel behaviors (as represented in Figure 4.17) occur in mixed energy system where the downdrift deflection of the ebb channel is generated by waves occurrence and punctuated by updrift shifts of the ebb channel. Those behaviors are defined by cycles with periods between 6 and 12 months for the "ebb-tidal delta breaching" model, and smaller ones for the quite similar "outer channel shifting" model (FitzGerald et al., 2000). In the case of the Cacela ebb-tidal delta, different periods of variations in the lower channel rotations and ebb-tidal delta tip migrations

were observed (Figures 4.19 and 4.20) without showing clear cycles and without obvious consistency with the computed wave parameters (Figures 4.22 to 4.30). Indeed, the sawtooth important variation observed for the lower channel orientation and ebb-tidal delta tip position in period I and II (Figure 4.21d,e) showed many notable successive inverse shifts with a time interval of 2 to 4 months that cannot be related to wave occurrence (Figures 4.22 to 4.30). Moreover, during periods IV and V, others more continuous evolutions about 4 to 6 months were noted. However, those evolutions showed inverse behaviors between the two periods while they do not show important differences in Pch (Figures 4.29 and 4.30). Indeed, period IV showed a lower channel and an ebb-tidal delta tip that rotated and migrated to the downdrift side of the ebb-tidal delta to finally come back to a centered position of the delta with quite similar inverse rates of changes (Figure 4.21d,e). Then, period V showed a rotation and a migration to the updrift side of the ebb-tidal delta to finally come back to a centered position of the delta with quite similar inverse rates of changes (Figure 4.21d,e). Those short-term variations could be in accordance with the models described by FitzGerald (2000) regarding their short-term periods of variations but they were not consistent with the computed waves parameters. According to Sha and Van den Berg (1993), when the channel is deflected mainly due to wave occurrence, it is the hydraulically inefficiency of the deflected tidal flow that force the shifting of the ebb channel to a preferential and more direct updrift seaward pathway. Moreover, according to Lenstra et al. (2019), the rotation of the channel could be supported by an optimum wave height leading to shear bed stress that allows the sediment to be transported. Thus, as the mixed influence is not constant over time and the hydrological conditions (especially waves) evolve over the years and seasonally, the short-term and highly variable evolution of the ebb channel could be justified by periods of wave- or tide-dominated hydrodynamic conditions combined with different waves parameters (like the height) an/or particular morphological features (like the inlet morphology or channel meanders inside the inlet). This raises several questions that could be analyzed for further study: For which wave conditions the channel is controlled by the tides and/or by the waves? What are the wave heights that control those dominances? Does the origin of the waves have an influence on these dominances? What does this represent in terms of percentage of the year? Do the other morphological features of the system have an influence on this variability?

5.3. Cacela inlet and barriers spit morphodynamics

The first general observation that can be made on the morphodynamic evolution of the Cacela inlet from September 2015 to September 2020 is that this inlet showed a quite stable position evolving mostly with unbalanced growing and reduction of the barrier's spits, downdrift and landward inside the back-barrier basin (Figure 4.11). This unbalanced growing inside the basin was consistent with the landward migration and welding to the downdrift barrier of the ebb-tidal delta shoals (Figure 4.15). Indeed, according to FitzGerald (1984) this migration generates a preferential progradation along the downdrift side of the inlet shoreline mainly due to the general littoral drift combined with the short-term wave's occurrence. To illustrate this, period I of the integrated morphological evolution (4.4) was the only period of the timeframe that showed a clear downdrift and landward spits and inlet important migration (Figure 4.21f,g) reflecting this imbalance in their development (Figure 5.3). This period was associated with mixed origins waves with a larger Pch than the rest of the timeframe (except periods J and S representing smaller particular periods) and with a particular notable proportion of western waves (Figures 4.29 and 4.30). During this period, the downdrift barrier widens (orange arrow in Figure 5.3) due to the welding of well-developed shoals in the downdrift part of the ebb-tidal delta (red dashed circle in Figure 5.3). At the same time, due to its greater exposure to powerful waves as well as the lack of sand input from landward bar migrations, the opposite updrift shoreline erodes (FitzGerald, 1984). Indeed, the updrift barrier eroded during period I facing the western waves, and thus thinning and lengthening northward into the basin (orange arrow in Figure 5.3).

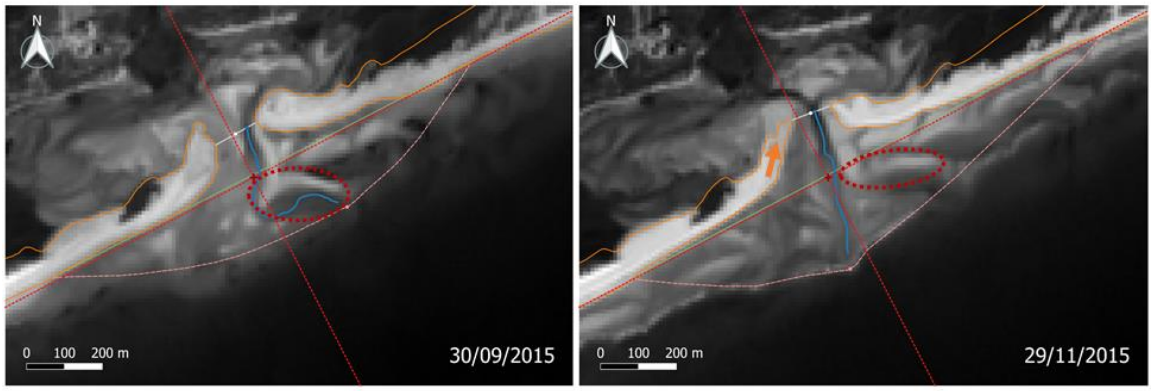

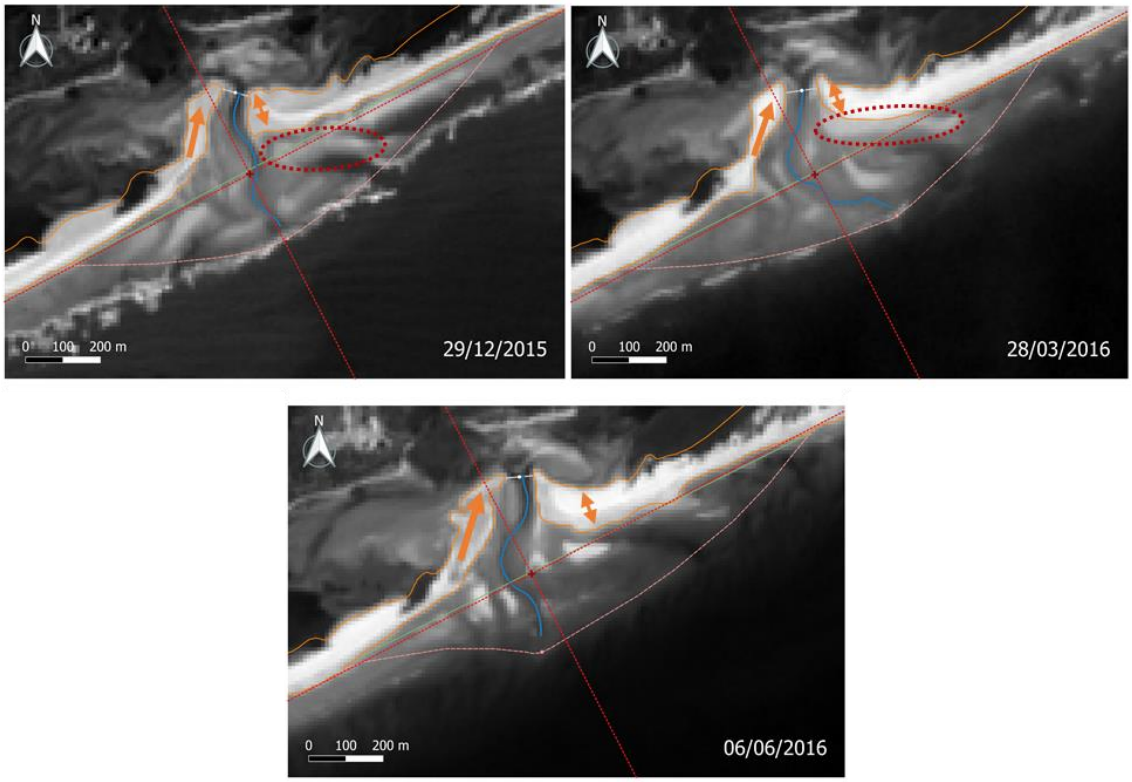

Figure 5.3 - Schematic representation of an example of barriers unbalanced development (orange arrows: barrier growing, red dashed circles: approximate shoal position and extension)

According to FitzGerald (1984) the symmetry of the ebb tidal delta around the inlet shoreline and the wave climate control also the long-term trends of barrier accretion or erosion. This symmetry was primarily determined by the orientation of the main ebb channel, which is induced by the alignment of the inlet shoreline and the meandering characteristics of the channel thalweg (FitzGerald, 1984). When accretion along one side of the inlet interacts with erosion along the opposite shore to generate a change in the deflection of ebb-tidal currents at the mouth of the inlet, the asymmetry of the ebb-tidal delta changes (e.g., September 2015 vs. June 2016 in Figure 5.3). As a result, the primary ebb channel is reoriented, the ebb delta configuration is altered, and new erosional and depositional patterns along the inlet beaches are brought about. This is further evidence of the short-term nature of the variations in the system.

Moreover, the orientation and position of the ebb channel within the inlet can have a significant influence on the morphodynamics of the barrier's spits (e.g., Figure 5.4). Indeed, an oblique channel, preferentially directed towards a barrier shore will tend to erode it, especially in low wave conditions as there is less sand input from the shoals migration that are attenuated. To

illustrate this, the circular oblique channel, tilted by the major eastern storm in April 2017, appeared to significantly erode the updrift barrier towards which it is directed throughout period III (until January 2018)(Figure 5.4). During this period, the waves conditions showed lower Pch than most of the other periods, particularly regarding western waves, with a balance number of hours (Figures 4.29 and 4.30). These low waves settings leaded to a dominance of the tidal currents that promoted the erosion of the updrift barrier (e.g., orange triangles in Figure 5.4) associated with the updrift and seaward migration of the inlet during period III (Figure 4.21f,g).

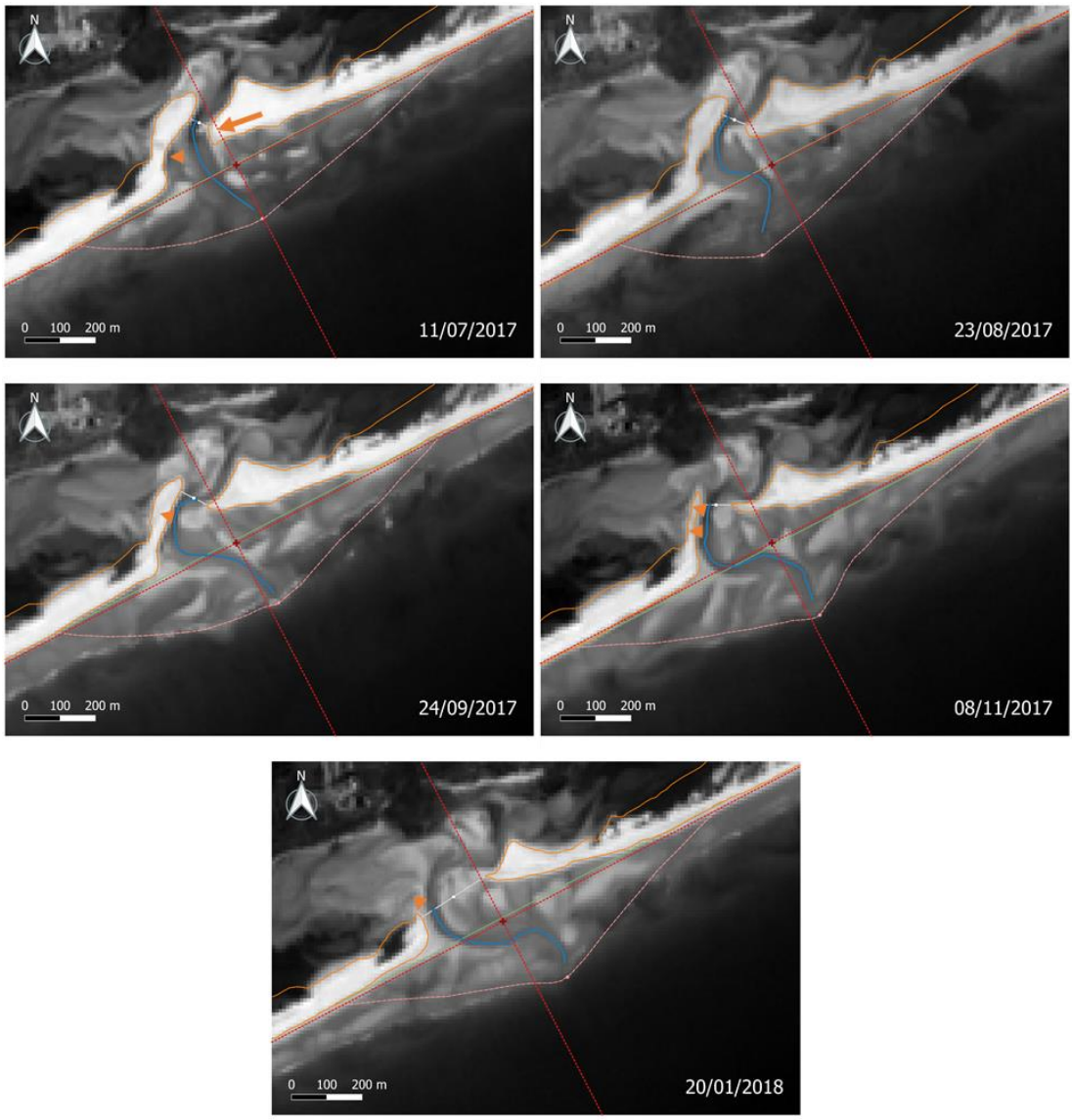

Figure 5.4 - Schematic representation of an example of barrier erosion due to oblique and arcuate ebb channel inside the inlet (orange arrow: barrier growing, orange triangles: barriers erosion)

After the Emma western storm of March 2018 (period J) placed the channel in the middle of the inlet, the latter seemed to stabilize with growing barriers during period IV (until May 2019) thanks to a channel oriented in such a way that it cannot significantly erode the spits of the barriers. Thus, it allows the barriers to develop in a rather balanced way during period V, leading them to a quite stable hoof shape bordering a well anchored and straight channel (as can be observed in Figure 5.5 corresponding to the last image of our dataset). This balanced development during period V could be associated to a balanced waves influence showing low Pch with almost equal values for western and eastern waves (Figure 4.29).

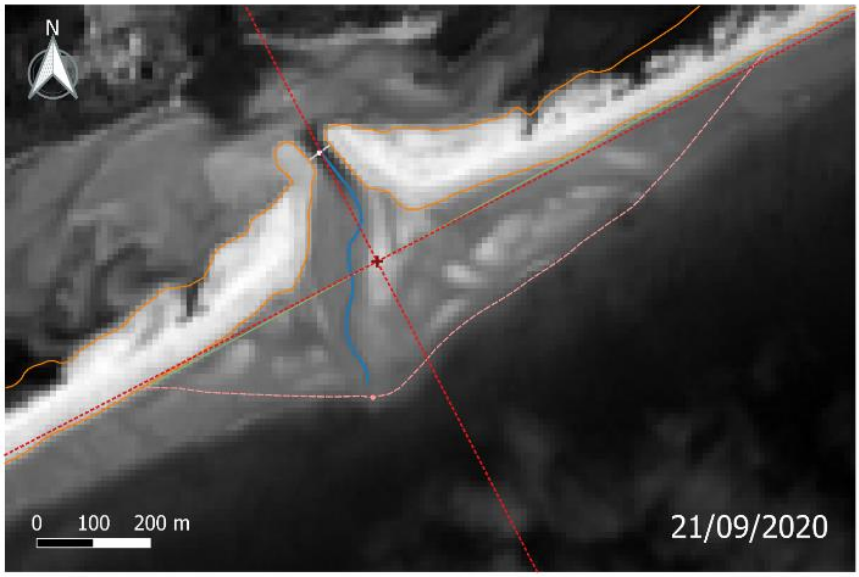

Figure 5.5 - Example of stabilized inlet bordered by hoof-shaped barriers

5.4. Storm influence on morphodynamic behavior

In the case of the Cacela inlet and ebb-tidal delta, storms do not seemed to have a typical influence. Indeed, due to their strong bidirectional influence (SW or SE) and to the different morphological settings when they happen, they acted in different ways on the systems without showing drastic impacts. The three major storms noted in the hydrodynamic analysis seemed to represent some behaviors of the influence they can have on this system.

The first one, happening in April 2017 and coming from the East (South-East) with a maximum power of 1.60 $x10^5$ W/m, impacted the inlet by pushing updrift and landward (predominantly) most of the shoals (red dashed arrows in Figure 5.6) but also the barriers spits particularly. In fact,

the updrift barrier was a bit pushed and tilted updrift, inside the basin, while the downdrift barrier was elongated updrift leading to an offset morphology of the spit on the inlet (Figure 5.6). These evolutions of the barrier spits have reduced the opening of the inlet and tilted the upper part of the ebb channel. Thus, the channel was no longer in equilibrium with the barriers and began to significantly erode the updrift barrier until January 2018 (period III).

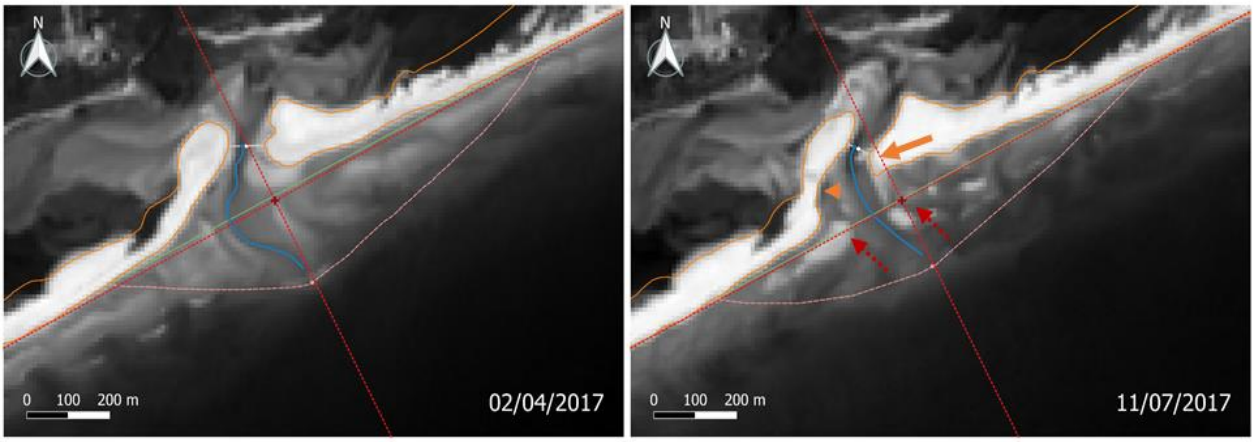

Figure 5.6 - Schematic representation of the impact of the April 2017 eastern storm (orange arrow: barrier growing, orange triangle: barrier erosion, red dashed arrows: shoals displacement)

The most powerful and quite well-known Emma storm (Malvarez, 2021), happening over February-March 2018 and coming from the West (South-West) with a maximum power of 2.87 $x10^5$ W/m, impacted the inlet by pushing downdrift (predominantly) and landward most of the sediments (red arrows in Figure 5.7). In fact, most of the shoals were displaced inside or close to the inlet and the channel was placed on its center (blue arrow in Figure 5.7). This relocation seemed to have stabilized the inlet and the barriers spit by stabilizing the channel, quite anchored in the middle of well-developed shoals and spit platforms. Indeed, the ebb channel, that was eroding the updrift barrier previously due to its arcuate shape longing the updrift barrier, was relocated in a more direct path to the ocean avoiding the erosion of the inlet shores. Moreover, it seemed to have stabilized the entire system (Cacela inlet and ebb-tidal delta) that showed less variations regarding its features after this storm (Figure 4.21). This system looked like it was in a standing period without any change from March to May 2018 but it seems to undergone an important recovery from May to July 2018 that slightly continues until May 2019 (Figure 4.21).

Thus, the recovery time from these two major storms appeared to have been between 5 months and about 1 year.

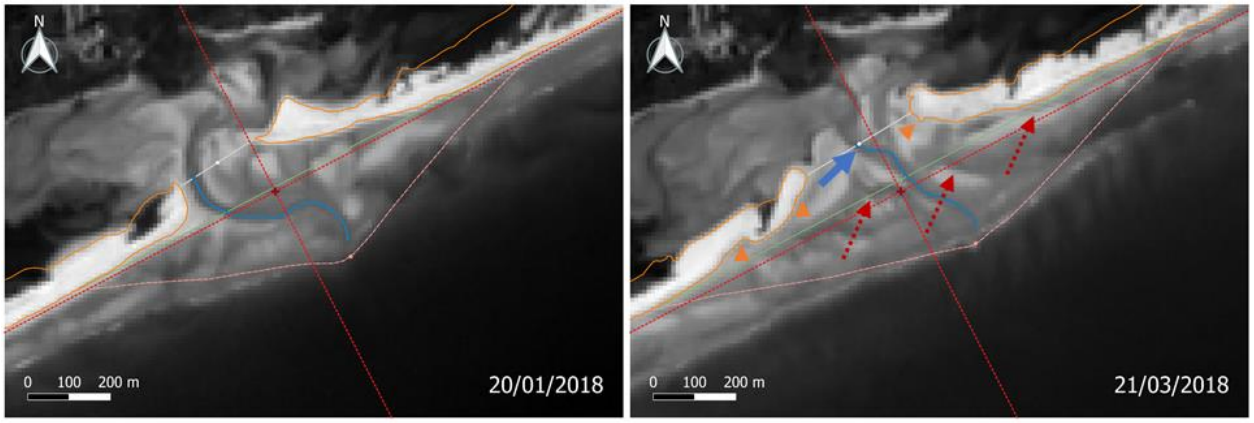

Figure 5.7 - Schematic representation of the impact of the March 2018 Emma western storm (orange triangles: barriers erosion, red dashed arrows: shoals displacement, blue arrow: ebb channel shifting)

The third one, happening in December 2019 and coming from the west with a maximum power of 1.87 x10^5 W/m, seemed to have no clear impact on the system (Figure 5.8). In fact, apart from a slight erosion of the directly exposed updrift beach and an unclear migration of shoals on the downdrift platform, there are no drastic changes observed. This might mean that the system already recovered (which would be very fast compared to the others), or that storms with those settings do not clearly impact it.

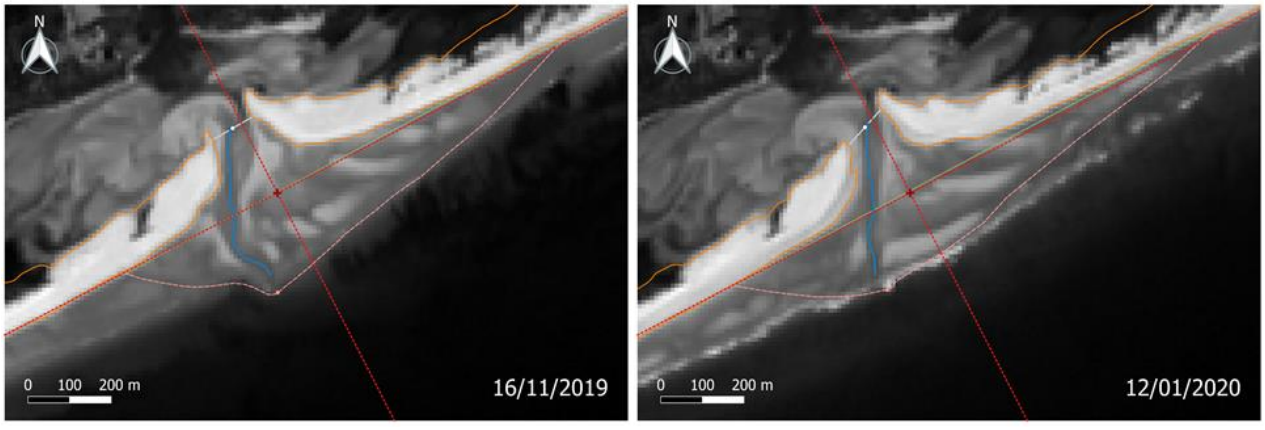

Figure 5.8 - Images before and after the December 2019 western storm showing no major impact

To conclude on storms influence, the angle of incidence and the power could have an importance for the storm to impact the system. Eastern storms, coming mostly from the SE, can have a clear impact as they face sub-perpendicularly the Cacela-Cabanas system and they are competing sub-

perpendicularly with the general littoral drift. Western storms, coming mostly from the SW, would need a very high power to impact the system as they are very oblique to its main orientation and its general morphology is generated mostly by western waves conditions. They can also act as a stabilator for the inlet when the upper channel is oblique and has an updrift barrier eroding tendency as during Emma storm. This raises the question that if the channel had not been relocated by this important storm, how long would it have continued to erode the updrift barrier? To further investigate, it would be interesting to study a larger set of storms with smaller and more precise study periods. Like that the origins and power of the storms could be analyzed in a relevant and robust way to understand their impact on the ebb-tidal delta, the inlet and the barriers.

5.5. Comparison with the inlet before its artificial relocation in 2011

The results obtained for the Cacela Inlet from September 2015 to September 2020 were compared with those found in the literature concerning the evolution of the former nearest inlet (Lacém Inlet) before its relocation in 2011 in order to discuss its behavior after its artificial opening.

Prior to 2011, Lacém Inlet exhibited an almost constant eastward migration with values between 3 and 215 m/year (Kombiadou, 2019). This migration was primarily due to significant accretion on the updrift barrier, imbalanced by erosion of the downdrift barrier and leading to a reduction of the inlet threatening to close (Figure 5.9). Its width varied greatly between significant values of 165 and 2000 m (Kombiadou, 2019) showing an inlet geometrically unstable that supported the migration through strong updrift barrier constructional processes (Figure 5.9) (Vila-Concejo et al., 2006). In addition, its cross-shore migration was landward from 1952 to 1986 reversing to a seaward progradation from 1986 to 2014 (Kombiadou, 2019). Furthermore, the Cacela Peninsula showed many breaching episodes mainly due to energetic events such as in winter 1995-1996 (Matias et al., 1999).

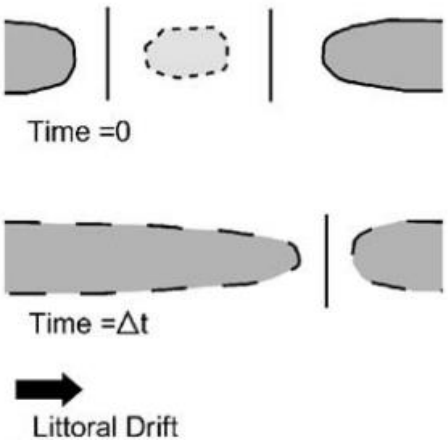

Figure 5.9 - Low energy typical inlet migration pattern determined for Ria Formosa natural inlet and characterized for Cacela Inlet (Vila-Concejo et al., 2002)

Since 2015, our results for Cacela Inlet showed a balanced along-shore migration varying between - 344 m/year westward and + 349 m/year eastward (averaged at + 3.64 m/year) with an inlet remaining roughly at its artificial opening position. The cross-shore migration showed a less balanced variation varying between -295 m/year seaward and + 483 m/year landward with an average of + 28.57 m/year thus seeming to have a slight landward trend. These migrations were explained by the inconstant and non-uniform evolution of the barriers which develop downdrift and landward (within the basin) or updrift and seaward (initial aligned positions). This evolution allows the mouth to keep an opening between 45 and 295 m (between 45 and 150 m for 90% of the values).

Thus, the evolution of the inlet from 1952 to 2011 is reminiscent of the Inlet migration and spit breaching model developed by FitzGerald (2000), while the evolution of the inlet from September 2015 to September 2020 is reminiscent of the Outer channel shifting or even Stable inlet models.

Although the timeframes are very different and 5 years is less representative for the evolution of the Cacela ebb-tidal delta, the stabilization of the inlet after its relocation can be supposed.

5.6. Limits of the study and future improvements

Through this study, the different mechanisms and short-term evolutions of the parameters of the Cacela Inlet and ebb-tidal delta could be hypothesized. However, it is necessary to keep a critical eye on the considered assumptions and obtained results.

Firstly, the resolution of the images does not allow to obtain very precise results because of the small scale of the studied system. Indeed, the resolution of band 3 of the Sentinel-2 images is 10 m while this system does not exceed 1300 m wide and 500 m long including many parameters confined to small areas such as the inlet. Thus, the various delineations made for the qualitative analysis of this system are often ambiguous and are a matter of morphological interpretation such as the definition of barriers or shoals, which sometimes are grouped together. Moreover, the variations of the quantified parameters are often on the order of ten meters (7 m of variability along-shore or 0.12 m/day for the rate, and 12 m of variability cross-shore or 0.20 m/day for the rate), which is near or even under the resolution of the images. Among the variations of all the parameters, it is the along-shore migration of the inlet that presents the minimum variation estimated at - 0.4 m on average between images (or + 0.01 m/day for the rate), and the along-shore migration of the tip that presents the maximum variation of - 10 m on average between images (or + 0.3 m/day for the rate). Moreover, the small amount of data over our study time does not allow us to determine other reliable statistical errors related to the mean for example. Thus, although some of the results show significant changes that can be interpreted during specific events or periods, the set of results below these errors only allows to hypothesize about the stability or general evolution of certain periods and the relationship between them. To support these results, very high-resolution imagery of about 1 m (very expensive) or bathymetric data of the area could be carried out although it would be difficult to have a time series of the later. Such data would allow to know with a high resolution the areas submitted to erosion or deposition of sediment and quantify the migration of the morphologies, the loss or gain of sediments, the area of the delta or the cross-sectional area of the inlet.

Secondly, the variations of the data set are short term or even very short term (shorter than the selected time interval) with different changes throughout the timeframe. Indeed, for the qualitative analysis of shoals for example, a time step of 6 months is not sufficient to observe notable changes, cyclicities or seasonality. It is necessary to reduce the time step to about 2 months to begin to observe some on the images. For quantitative analysis, these characteristics are not observable with a 6 months' time step either and a 2 months' time step is just enough to observe some of them without being able to draw accurate conclusions. To support these results

and hypotheses, it would be important to reduce the time step below 2 months and/or to extend the timeframe to more than 5 years as this system evolves differently from year to year and some mechanisms could last between 5 and 10 years such as shoals' formation until welding to the barriers (FitzGerald, 2000). However, this is not possible with the availability of Sentinel-2 images that start at the launch of the first satellite in 2015 and depend on cloud cover and tide level to be analyzed. The use of other satellite images or aerial photos taken on a smaller time scale or over a longer period could then support these results, although this system is only analyzable from the opening of the inlet in 2011.

Then, the choice of some parameters brings results that can sometimes be ambiguous. Indeed, the qualitative observation of barriers or shoals does not allow a precise study of these parameters and would require a support of more high-resolution data. Moreover, the ebb channel evolving almost constantly in different meandering forms and being deflected at different positions on the Cacela ebb-tidal delta, the separation in two of its orientation does not allow either to have a precise idea on its evolution. A separation into several subparts of the ebb channel could add precision to its evolution on the Cacela ebb-tidal delta. Secondly, measures related to the inlet such as its opening may have errors because they depend on the delayed and non-uniform evolution of the barrier ends. A measurement of the opening at the average barrier alignment could support the measurement of the minimum opening between barriers.

Finally, regarding the hydrodynamics of the system, the wave data are modelized data and not obtained in situ, which can lead to some differences when compared to the actual waves at the same location (here the values are quite minimized compared to in situ ones). However, the closest buoy is located off-shore the Ria Formosa tip and undergoes way more western waves occurrence. Thus, to improve those data, in situ data close to the system should be taken. Moreover, as the Cacela ebb-tidal delta has a strong tidal influence, tidal data should be analyzed and particularly the tidal currents and the tidal prism controlling many ebb-tidal delta parameters and behaviors. To calculate it, basin area measurements and/or inlet cross-sectional area time series would need to be collected. Thus, by computing its ratio on the littoral drift, it could give information about the dominant sediment bypassing for example (Lenstra, 2019).

6. Conclusion

Based on Sentinel-2 satellite images and data from a numerical model, this study has produced a first morphological characterization of the Cacela inlet and ebb-tidal delta system that was linked to the wave regime from September 2015 to September 2020. This was done first through the analysis of the different barriers, inlet and ebb tidal delta features morphology and morphodynamics. Then through the characterization and the connection with the wave's conditions and particularly to the waves power and angle of incidence.

Although this system showed a large variability that was not described at other (often larger) ebb-tidal delta, the Cacela inlet and ebb-tidal delta were defined as a system with mixed energy influences showing characteristic morphological features produced by both tidal currents and wave forcing. Its general morphology presented an ebb-tidal almost constantly composed of well-developed channel margin linear bars testifying the influence of the tides on the system. Those bars were bordering an ebb channel mainly oriented N-S on its upper (landward) part and deflected on its lower (seaward) part (mostly NW-SE with an important variability from W-E to NE-SW orientations). The waves influence was mainly expressed by a general asymmetry in the ebb-tidal delta composed of well-developed swash bars forming, aggregating and merging with the downdrift barrier in almost one year. This asymmetry as well as the shoals morphodynamics was explained by the combination of the eastward longshore drift and normalized power (Pch) of eastern waves, larger than for western waves, that also reach the coast more frontally than western waves (due to the NE-SW coastline orientation). A consistent wave seasonality was observed with the development of large and dynamic shoals in winter due to the influence of waves; in summer, these shoals were more scattered in summer due to the dominance of tides under low waves conditions. The position of the lower (seaward) part of the main ebb channel rotates significantly clockwise and anti-clockwise during periods of 2 to 6 months, similarly to the sediment bypass models of "outer channel shifting" and "stable inlet" of FitzGerald (2000). The inlet evolution was related to the barriers morphodynamics, which is strongly influenced by the ebb delta shoals/channel behaviors. Indeed, it showed a general downdrift and landward migration inside the back-barrier basin under the combination of large wave conditions from the South-East and the South-West that favours bars welding. Conversely, its position shifts updrift

and seaward under low wave conditions or when the ebb channel was tilted inside the inlet. This tilted channel was observed after the eastern storm of April 2017 that leaded to a long period of erosion of the updrift barrier spit. Then, the channel has straightened and shifted at the centre of the wide inlet, due to the western storm of March 2018 (Emma, the largest storm during the study period). This natural relocation seemed to have quite stabilized the system, that has not shown major morphological changes since, including the occurrence of a west storm in December 2019. The exception was the lower (seaward) part of the channel that undergone more continuous and large rotations, indicating that sediment continues to bypass according to the "outer channel shifting" and "stable inlet" models.

Overall, this study shows that the large and unusual morphological variability of the Cacela ebb tidal delta was hardly related to wave activity, except for some large storm events. Amongst those, the Emma storm stands as it triggered or promoted the presently observed stability of the inlet position. This stability contrasts with the high (downdrift) migration of Lacém Inlet (the former Cacela inlet before its artificial relocation in 2011), and indicates successful management regarding inlet sustainability. In future studies, the permanence of the inlet position should be confirmed, and the ebb delta morphodynamics should be evaluated based on additional data (satellite images, aerial photographs, bathymetry) a short time interval (every month for example).

References

Almeida, L. P. , Vousdoukas, M. V., Ferreira, Ó., Rodrigues, B. A. & Matias, A. (2012). Thresholds for storm impacts on an exposed sandy coastal area in southern Portugal. Geomorphology, 143, 3-12.

Azizian, A. (2017). Application of QGIS in Water Sciences and Engineering (In Persian).

Balouin, Y., Morris, B. D., Davidson, M. A. & Howa, H. (2004). Morphology evolution of an ebb-tidal delta following a storm perturbation: assessments from remote sensed video data and direct surveys. Journal of Coastal Research, 202, 415-423.

Bergsma, E. W. & Almar, R. (2020). Coastal coverage of ESA' Sentinel 2 mission. Advances in Space Research, 65(11), 2636-2644.

Bergsma, E. W., Almar, R., Garlan, T. & Kestenare, E. (2020). Global wave-driven beach evolution; consequences for observation strategies. Non-peer reviewed EarthArXiv preprint.

Bertin, X., Li, K., Roland, A. & Bidlot J.-R. (2015). The contribution of short-waves in storm surges: two case studies in the Bay of Biscay. Continental Shelf Research, 96, 1-15.

Boothroyd, J. C. (1985). Tidal inlets and tidal deltas. R.A. Davis (Editor), Coastal Sedimentary Environments, Springer, New York, 2nd Edition, 445-532.

Costa, M., Silva, R. & Vitorino, J. (2001). Contribuição para o estudo do clima de agitação marítima na costa portuguesa (in Portuguese). II Jornadas Portuguesas de Engenharia Costeira e Portuária.

Costa, C.L. (1994). Final report of sub-project A "Wind wave climatology of the Portuguese coast". Instituto Hidrográfico, Report PO-WAVES 6/94-A, 80.

Davies, J.L. (1964). A morphogenic approach to world shorelines. Zeitschrift für Geomorphologie, 8, 27-42.

Davis, R. A. & Hayes, M. O. (1984). What is a wave-dominated coast? Marine Geology, 60(1-4), 313-329.

Davis, R. A. (2013). A new look at barrier-inlet morphodynamics. Journal of Coastal Research, 69, 1-12.

De Swart, H.E. & Zimmerman, J.T.F. (2009). Morphodynamics of tidal inlet systems. Annual Review of Fluid Mechanics, 41(1), 203-229.

Dias, J., Ferreira, Ó., Matias, A., Vila-Concejo, A. & Sa-Pires, C. (2003). Evaluation of soft protection techniques in barrier islands by monitoring programs: case studies from Ria Formosa (Algarve - Portugal). Journal of Coastal Research, 35, 117-131.

Ferreira, Ó., Matias, A. & Pacheco, A. (2016). The east coast of Algarve: a barrier island dominated coast. Thalassas, 32, 75-85.

Fisher, J.J. & Simpson, E.J. (1982). Tidal deltas. Schwartz, M.L. (Editor), Beaches and Coastal Geology, Encyclopedia of Earth Sciences Series, Springer, New-York, 817-818.

Fitzgerald, D.M. (1984). Interactions between the ebb-tidal delta and landward shoreline: Price Inlet, South Carolina. Journal of Sedimentary Research, 54(4), 1303-1318.

FitzGerald, D.M., Kraus, N.C. & Hands, E.B. (2000). Natural mechanisms of sediment bypassing at tidal inlets. U.S. Army Corps of Engineers, Coastal Engineering Technical Note CHETN-IV-30, U.S. Army Engineer Research and Development Center, Coastal and Hydraulics Laboratory, Vicksburg, 1-10.

FitzGerald, D.M. (2005). Tidal Inlets. Schwartz, M.L. (Editor), Encyclopedia of Coastal Science, Encyclopedia of Earth Sciences Series, Springer, Dordrecht, 958-964.

FitzGerald, D., Buynevich, I. & Hein, C. (2011). Morphodynamics and facies architecture of tidal inlets and tidal deltas. Davis, Jr. R., Dalrymple, R. (Editors), Principles of Tidal Sedimentology, Springer, Dordrecht, 301-333.

Gao, J. (2009). Bathymetric mapping by means of remote sensing: methods, accuracy and limitations. Progress in Physical Geography, 33(1), 103-116.

Garcia, T., Ferreira, Ó., Matias, A. & Dias, J.A. (2010). Overwash vulnerability assessment based in long-term washover evolution. Natural Hazards, 54, 225-244.

Garel, E. & Ferreira, Ó. (2015). Multi-year high-frequency physical and environmental observations at the Guadiana Estuary. Earth System Science Data, 7(2), 299-309

Gatti, A. & Galoppo, A. (2018). Sentinel-2 Products Specification Document, 14.5, 510.

Gibeaut, J.C. & Davis, R.A. (1991). Computer simulation modeling of tidal inlets. Kraus, N.C., Gingerich, K.J. & Kriebel, D.L. (Editors), Coastal sediments 1991, American Society of Civil Engineers, Seattle, 1389-1403.

Hayes, M.O. (1975). Morphology of sand accumulation in estuaries: an introduction to the symposium. Cronin, L.E. (Editor), Estuarine research, Vol II, Academic Press, New York, 3-22.

Hayes, M.O. (1979). Barrier island morphology as a function of tidal and wave regime. Leatherman, S.P. (Editor), Barrier Island—From the Gulf of St. Lawrence to the Gulf of Mexico, Academic Press, New York, 1-71.

Hayes, M.O. & FitzGerald, D. (2013). Origin, evolution, and classification of tidal Inlets. Journal of coastal research, 69, 14-33.

Hicks, D., & Hume, T.M. (1996). Morphology and size of ebb tidal deltas at natural inlets on open-sea and pocket-bay coasts, North Island, New Zealand. Journal of coastal research, 12(1), 47-63.

Holmes, P. (2001). Coastal processes: waves. The University of the West Indies, Professional development programme: coastal infrastructure design, construction and maintenance, A course in coastal defense systems I, Chapter 5.

Hughes, S.A. (2002). Equilibrium Cross Sectional Area at Tidal Inlets. Journal of Coastal Research, 18(1), 160-174.

Kombiadou, K., Matias, A., Carrasco, A.R., Ferreira, Ó., Costas, S. & Vieira, G. (2018). Towards assessing the resilience of complex coastal systems: examples from Ria Formosa (South Portugal). Journal of Coastal Research, 85, 646-650.

Kombiadou, K., Matias, A., Costas, S., Carrasco, A.R., Ferreira, Ó. & Plomaritis, T. (2019). Assessment of natural and anthropic drivers to the evolution of Ria Formosa barrier island system. Wang, P., Rosati, J.D. & Vallee, M. (Editors), Coastal Sediments 2019, World Scientific, Tampa/St. Petersburg, 57-70.

Kombiadou, K., Matias, A., Ferreira, Ó., Carrasco, A.R., Costas, S. & Plomaritis, T. (2019). Impacts of human interventions on the evolution of the Ria Formosa barrier island system (S. Portugal). Geomorphology, 343, 129-144.

Kombiadou, K., Matias, A., Costas, S., Carrasco, A.R., Plomaritis, T. & Ferreira, Ó. (2020). Barrier island resilience assessment: applying the ecological principles to geomorphological data. Catena, 194, 104-755.

Kraus, N.C. (2009). Engineering of tidal inlets and morphologic consequences. Kim, Y.C. (Editor), Handbook of Coastal and Ocean Engineering, World Scientific, Los Angeles, 1267-1300.

Kumar, K.V., Palit, A. & Bhan, S.K. (1997). Bathymetric mapping in Rupnarayan-Hooghly river confluence using IRS data. International Journal of Remote Sensing, 18(11), 2269-2270.

Lenstra, K.J.H., Ridderinkhof, W. & Vegt, M. (2019). Unraveling the Mechanisms That Cause Cyclic Channel-Shoal Dynamics of Ebb-Tidal Deltas: A Numerical Modeling Study. Journal of Geophysical Research: Earth Surface, 124(12), 2778-2797.

Li, W. & Gong, P. (2016). Continuous monitoring of coastline dynamics in western Florida with a 30-year time series of Landsat imagery. Remote Sensing of Environment, 179, 196-209.

Malvarez, G., Ferreira, O., Navas, F., Cooper, J.A.G., Gracia-Prieto, F.J. & Talavera, L. (2021). Storm impacts on a coupled human-natural coastal system: Resilience of developed coasts. Science of The Total Environment, 768, 144987.

Matias, A., Ferreira, O. & Dias, J. (1999). Preliminary results of the Cacela Peninsula (southern Portugal) replenishment. Boletín Instituto Español de Oceanografia, 15, 283-288.

Oliveira, T., Neves, M., Fidalgo, R. & Esteves, R. (2018). Variability of wave parameters and Hmax/Hs relationship under storm conditions offshore the Portuguese continental coast. Ocean Engineering, 153, 10-22.

Pawlowicz, R., Beardsley, B. & Lentz, S. (2002). Classical tidal harmonic analysis including error estimates in MATLAB using T_TIDE. Computers and Geosciences, 28(8), 929-937.

Pessanha, L.E.V. & Pires, H.O. (1981). Elementos sobre o clima de agitação marítima na costa sul do Algarve. Internal report, Instituto de Meteorologia e Geofísica, Lisboa, Portugal.

Petti, M., Bosa, S., Pascolo, S. & Uliana, E. (2020). An integrated approach to study the morphodynamics of the Lignano tidal inlet. Journal of Marine Science and Engineering, 8, 77.

Pires, H.O. (1998). Project INDIA. Preliminary report on wave climate at Faro. Instituto de Meteorologia, IST, Lisboa, Portugal.

Sha, L.P. & Van Den Berg, J.H. (1993). Variation in Ebb-Tidal Delta Geometry along the Coast of the Netherlands and the German Bight. Journal of Coastal Research, 9(3), 730-746.

Stiller, D., Ottinger, M. & Leinenkugel, P. (2019). Spatio-temporal patterns of coastal aquaculture derived from Sentinel-1 time series data and the full Landsat archive. Remote Sensing, 11(14), 1707.

Styles, R., Brown, M.E., Brutsché, K.E., Li, H., Beck, T.M. & Sánchez, A. (2016). Long-term morphological modeling of barrier island tidal inlets. Journal of Marine Science and Engineering, 4(4), 65.

Sun, C., Fagherazzi, S. & Liu, Y. (2018). Classification mapping of salt marsh vegetation by flexible monthly NDVI time-series using Landsat imagery. Estuarine, Coastal and Shelf science, 213, 61-80.

Vila-Concejo, A., Matias, A., Ferreira, Ó., Duarte, C. & Dias, J. (2002). Recent evolution of the natural inlets of a barrier island system in southern Portugal. Journal of Coastal Research, 36, 741-752.

Vila-Concejo, A., Ferreira, Ó., Morris, B.D., Matias, A., & Dias, J. (2004). Lessons from inlet relocation: examples from Southern Portugal. Coastal Engineering, 51(10), 967-990.

Vila-Concejo, A., Matias, A., Pacheco, A., Ferreira, Ó. & Dias, J. (2006). Quantification of inlet-related hazards in barrier island systems. An example from the Ria Formosa (Portugal). Continental Shelf Research, 26, 1045-1060.

Warne, D.K. (1978). Landsat as an aid in the preparation of hydrographic charts. Photogrammetric Engineering and Remote Sensing, 44(8), 1011-1016.

Zhang, H., Li, D., Wang, J., Zhou, H., Guan, W., Lou, X. & Ren, L. (2020). Long timeseries remote sensing analysis of the periodic cycle evolution of the inlets and ebb-tidal delta of Xincun Lagoon, Hainan Island, China. Journal of Photogrammetry and Remote Sensing, 165, 67-85.

Webography

Copernicus Open Access Hub. European Commission. European Spatial Agency. Copernicus program. URL: https://scihub.copernicus.eu/dhus/#/home (access date: 25/01/2021).

Puertos del Estado. Oceanography. Forecast, real-time weather and climate. URL: Prediccion de oleaje, nivel del mar ; Boyas y mareografos | puertos.es (access date: 10/05/2021)

Sentinel Online. User Guides. Sentinel-2 MSI. Resolutions. URL: https://sentinel.esa.int/web/sentinel/user-guides/sentinel-2-msi/resolutions#:~:text=The%20revisit%20frequency%20of%20each,in%20a%20satellite%20sensor%20array. (access date: 14/01/2021).

Sentinel Online. Missions. Sentinel-2. Data Products. URL: https://sentinel.esa.int/web/sentinel/missions/sentinel-2/data-products (access date: 14/01/2021).

Appendices

Appendix 1 - Digitized parameters of the Cacela Inlet and ebb-tidal delta over the selected Sentinel 2 satellite images from September 2015 to September 2020

Legend:

- Reference point (origin) for migration analysis
- Along-shore / Cross-shore axis
- Barriers
- Inlet width
- Main ebb channel
- Ebb-tidal delta maximum width
- Ebb-tidal delta extension
- Mean inlet position
- Channel position at inlet
- Ebb-tidal delta tip position

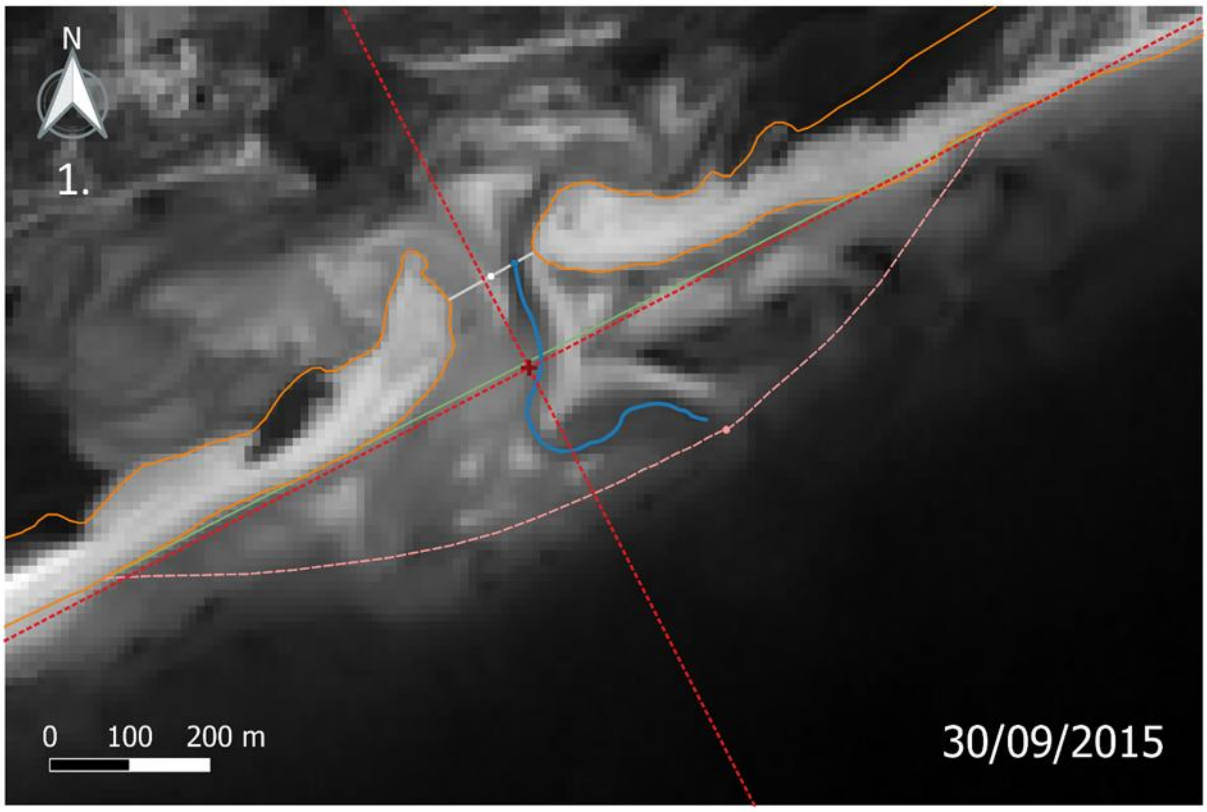

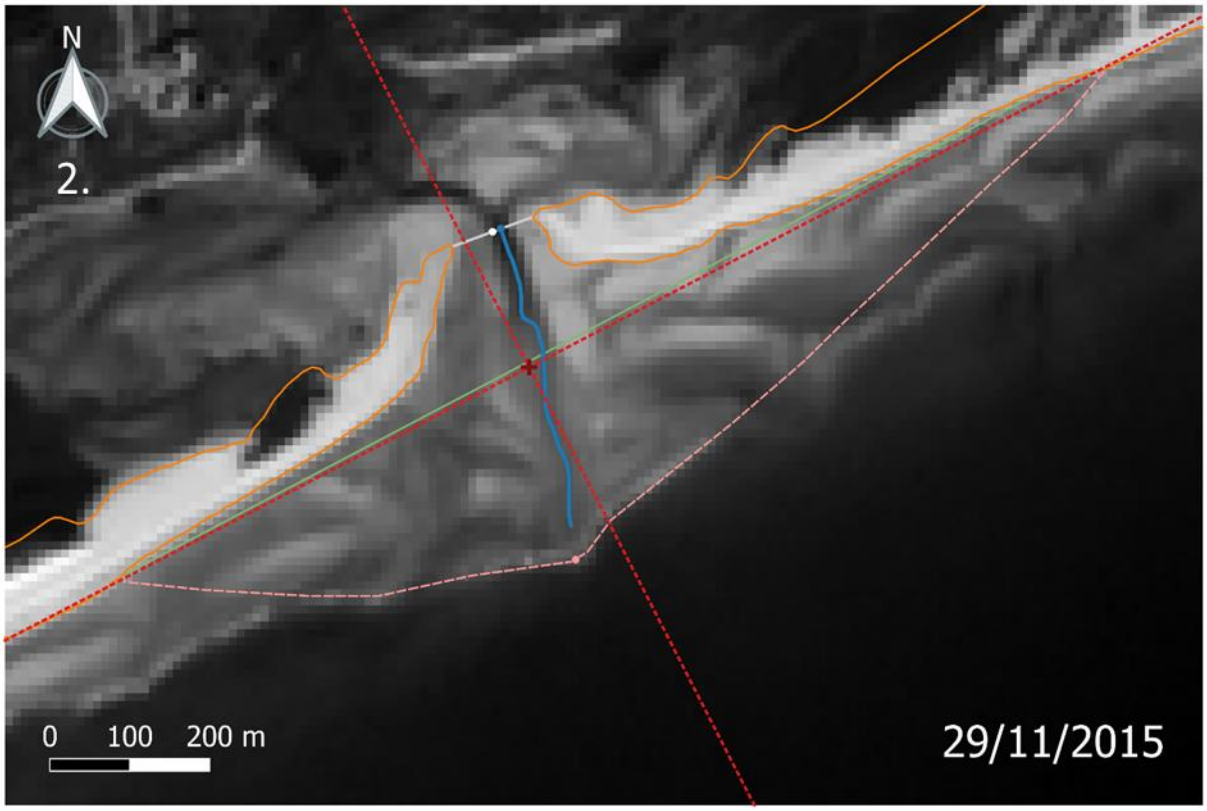
N
2.
0 100 200 m
29/11/2015

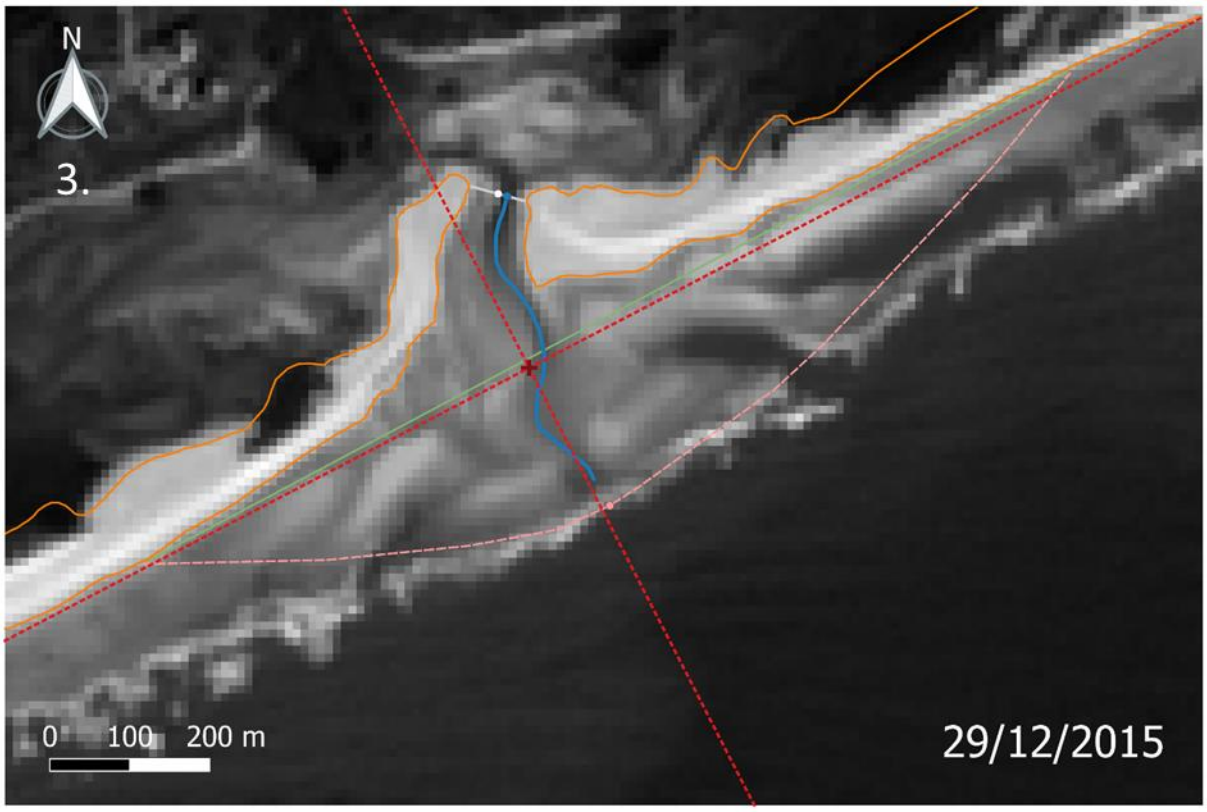
N
3.
0 100 200 m
29/12/2015

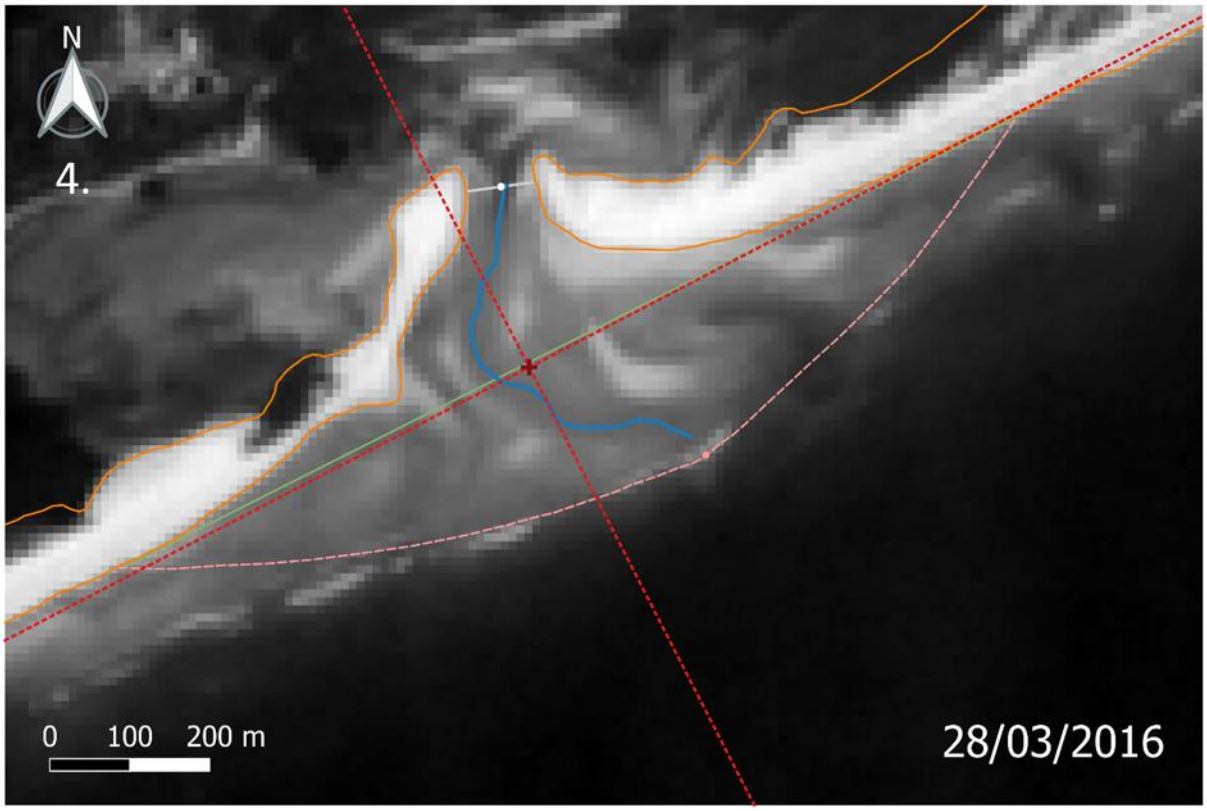
N
4.
0 100 200 m
28/03/2016

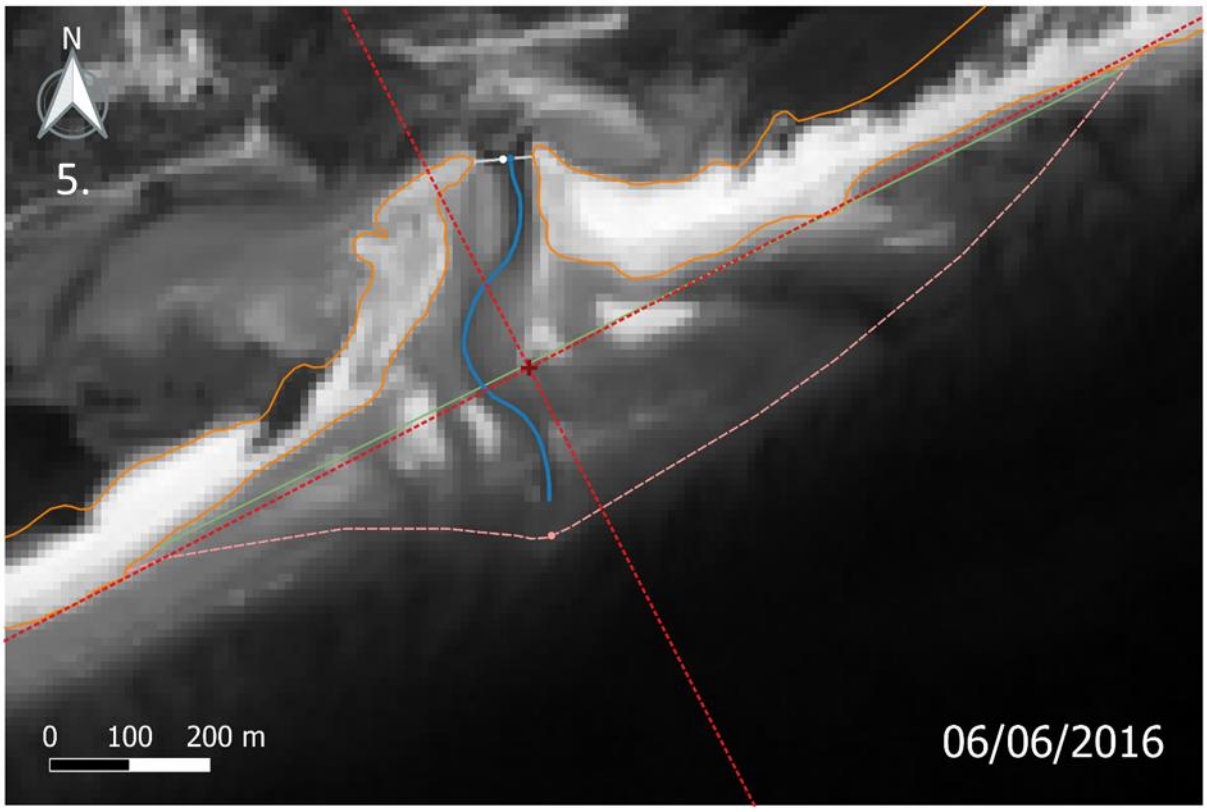
N
5.
0 100 200 m
06/06/2016

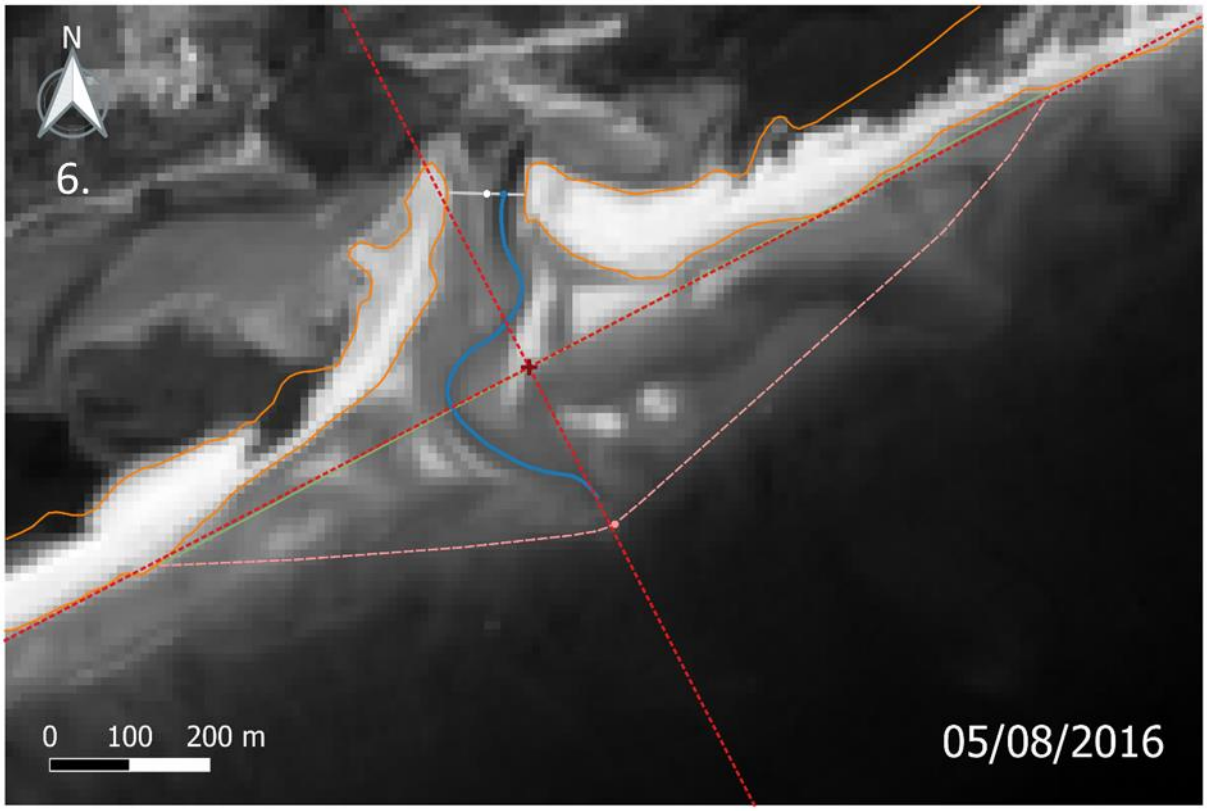
N
6.
0 100 200 m
05/08/2016

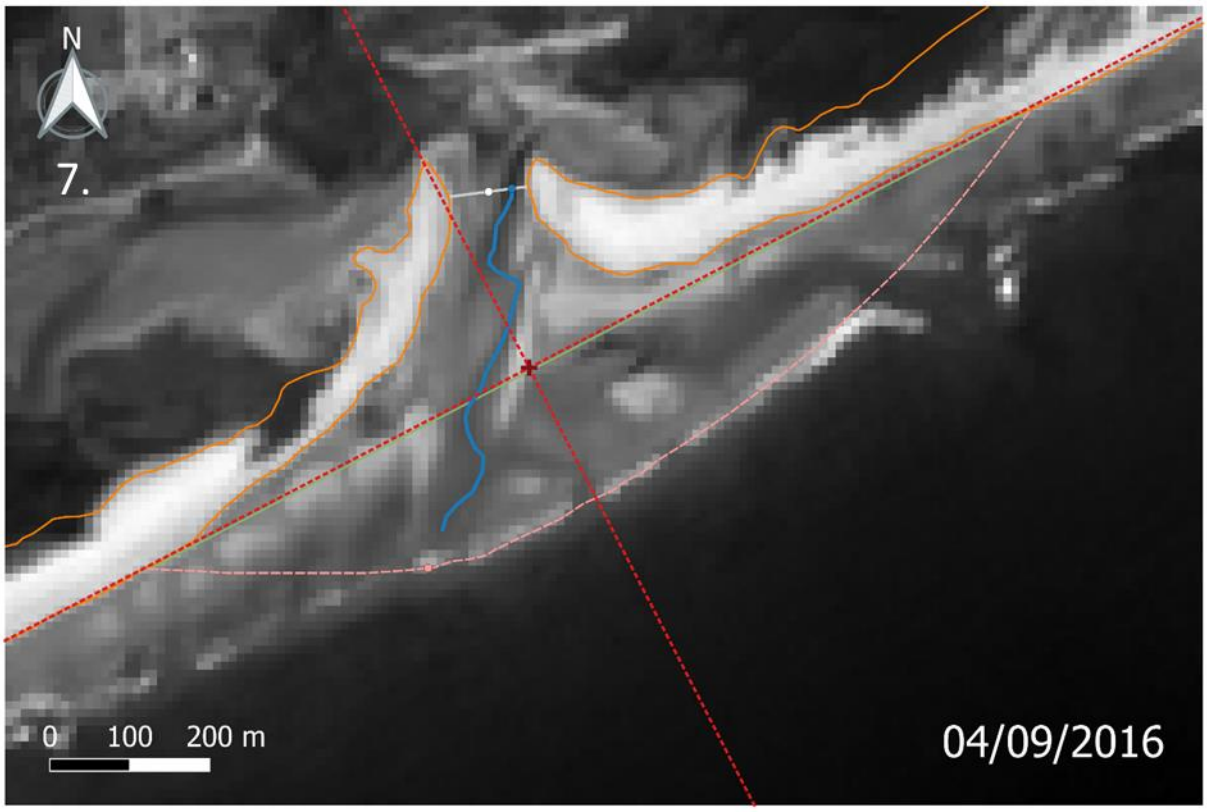
N
7.
0 100 200 m
04/09/2016

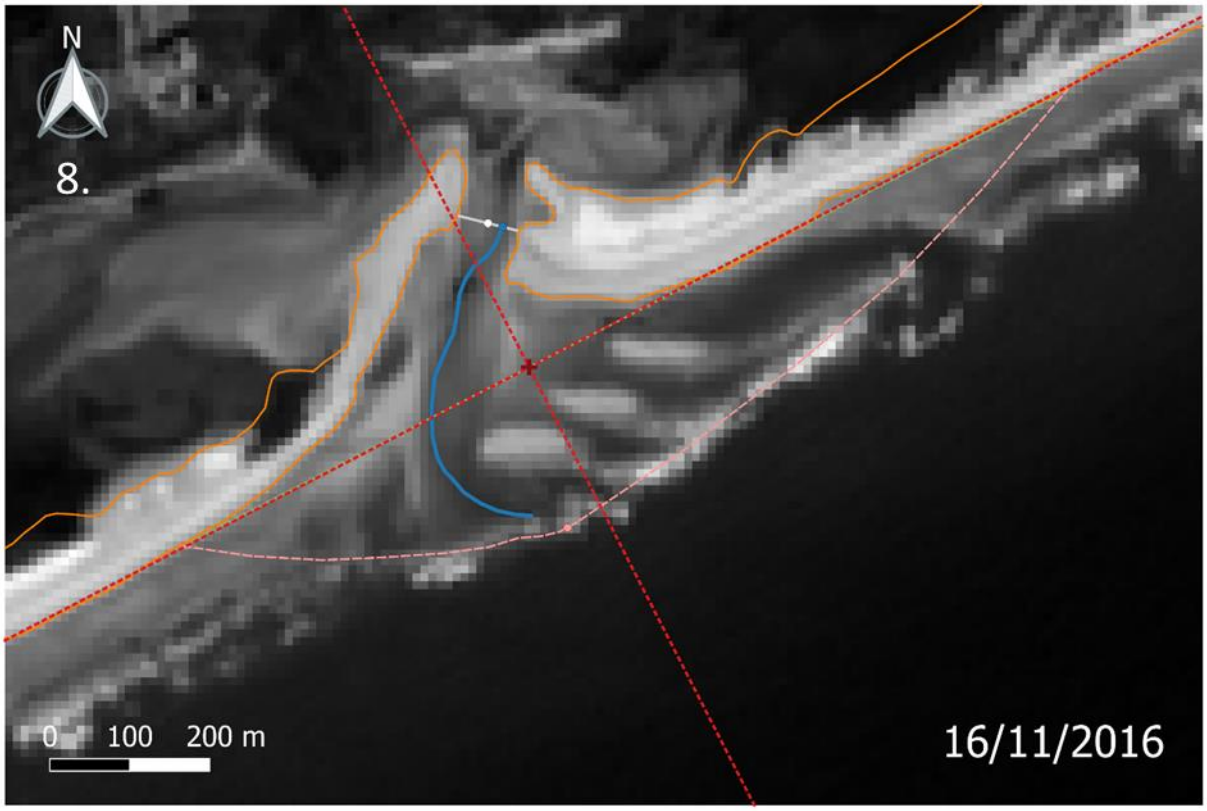
N
8.
0 100 200 m
16/11/2016

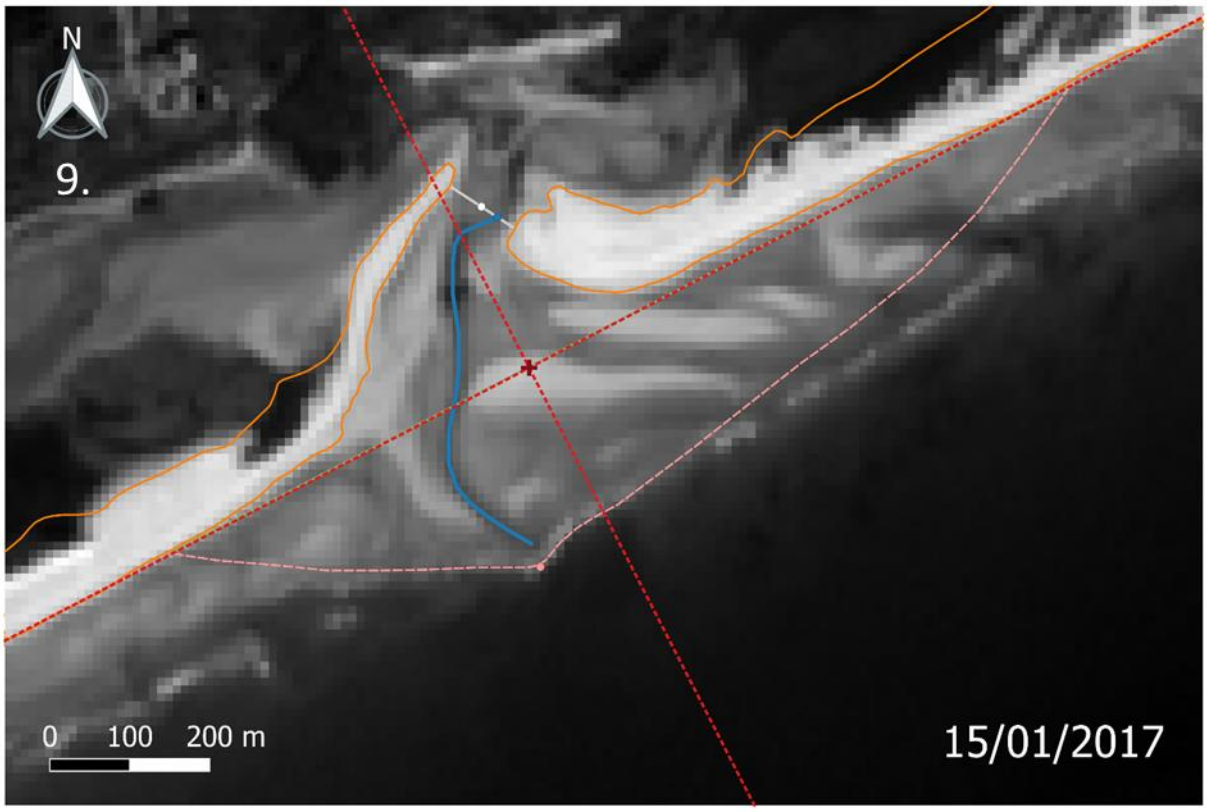
N
9.
0 100 200 m
15/01/2017

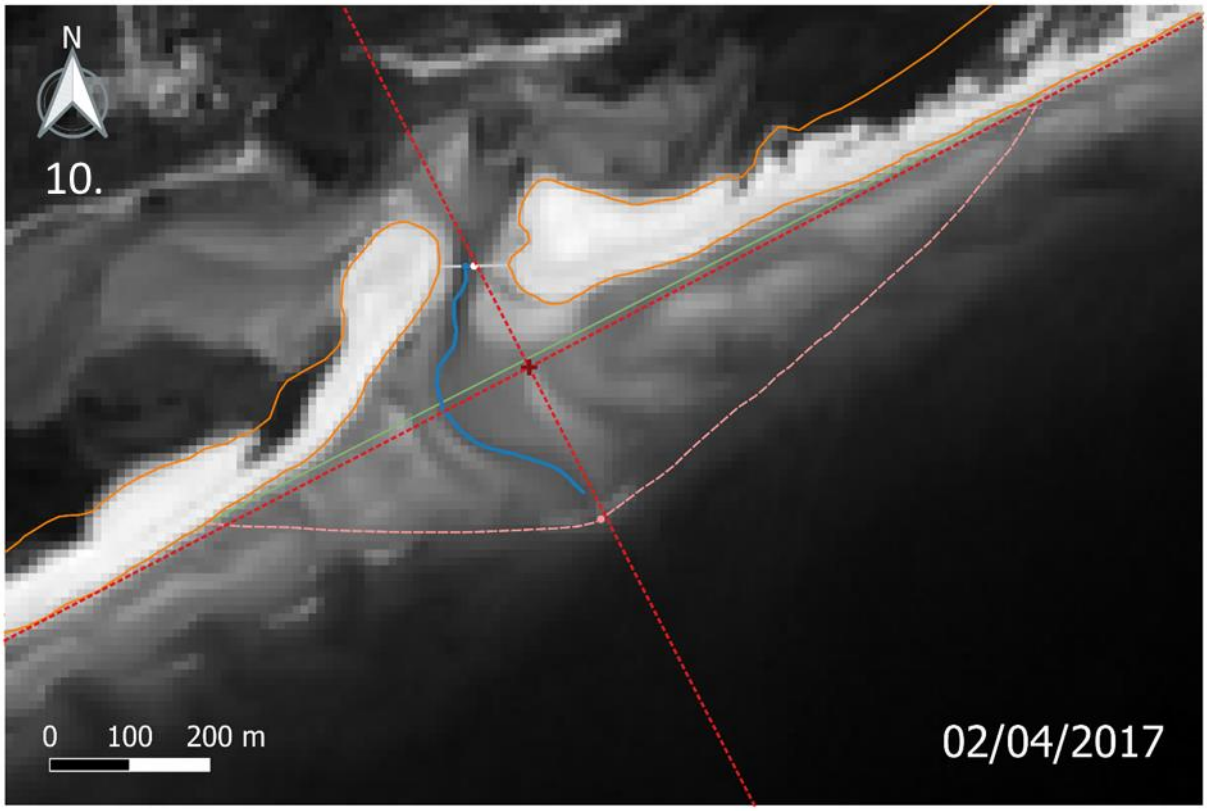
N
10.
0 100 200 m
02/04/2017

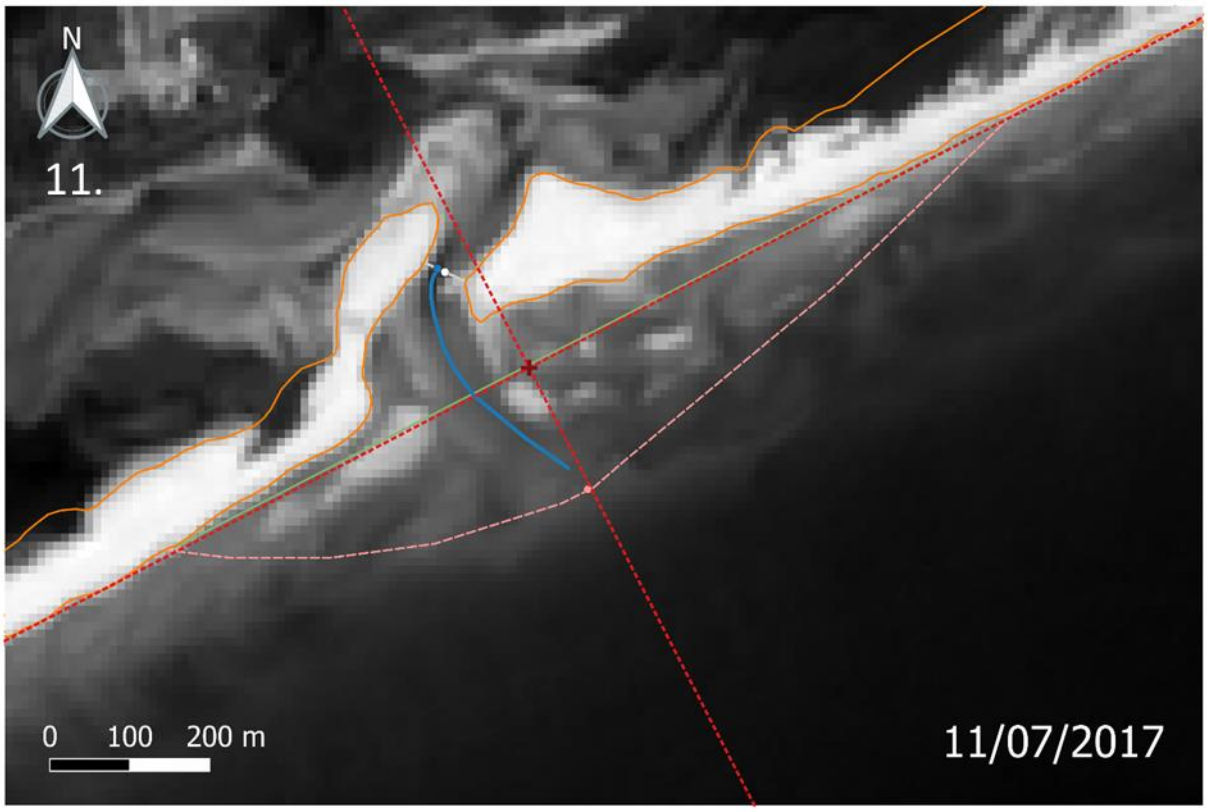
N
11.
0 100 200 m
11/07/2017

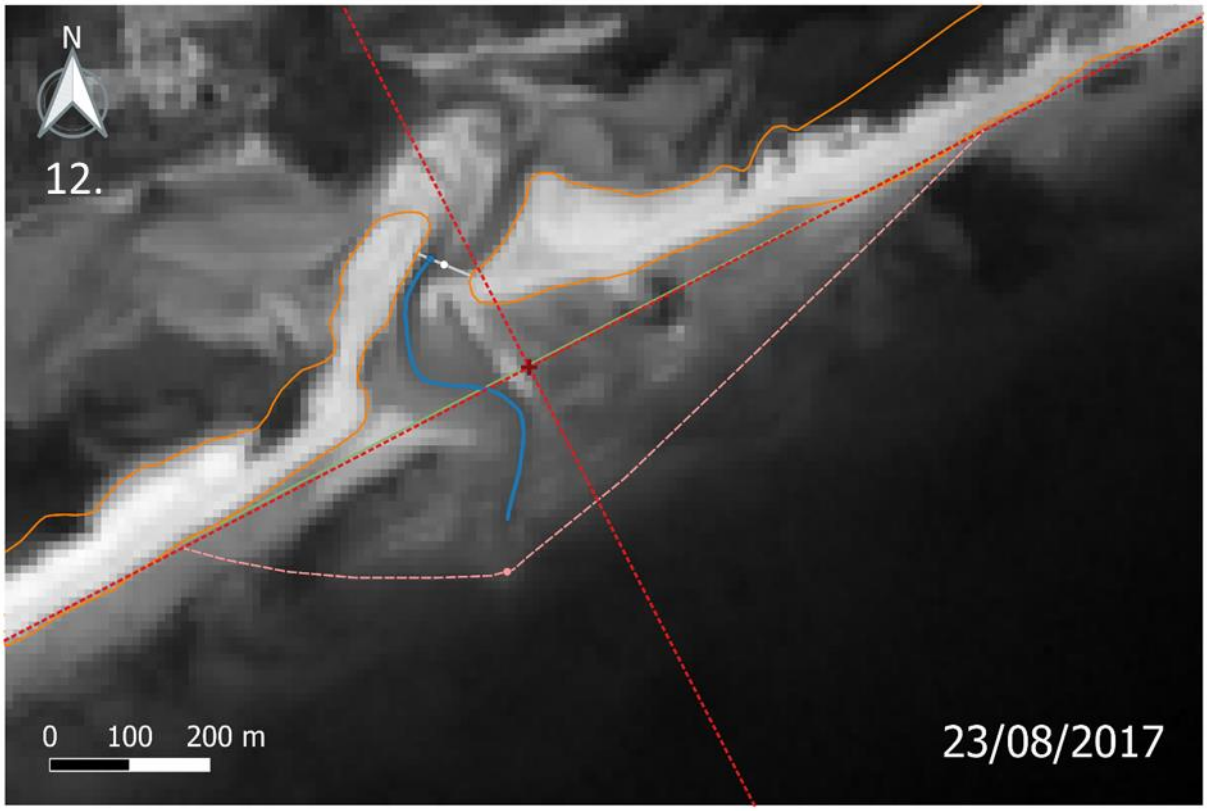
N
12.
0 100 200 m
23/08/2017

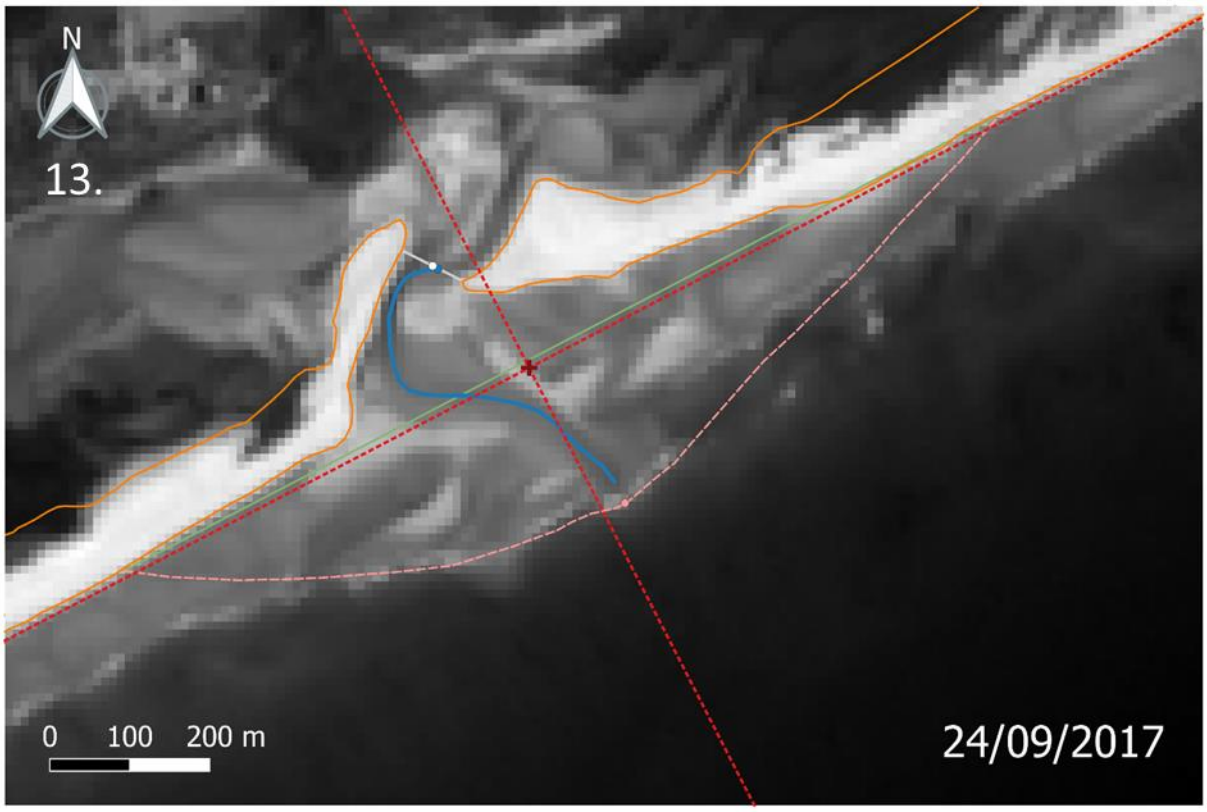
N
13.
0 100 200 m
24/09/2017

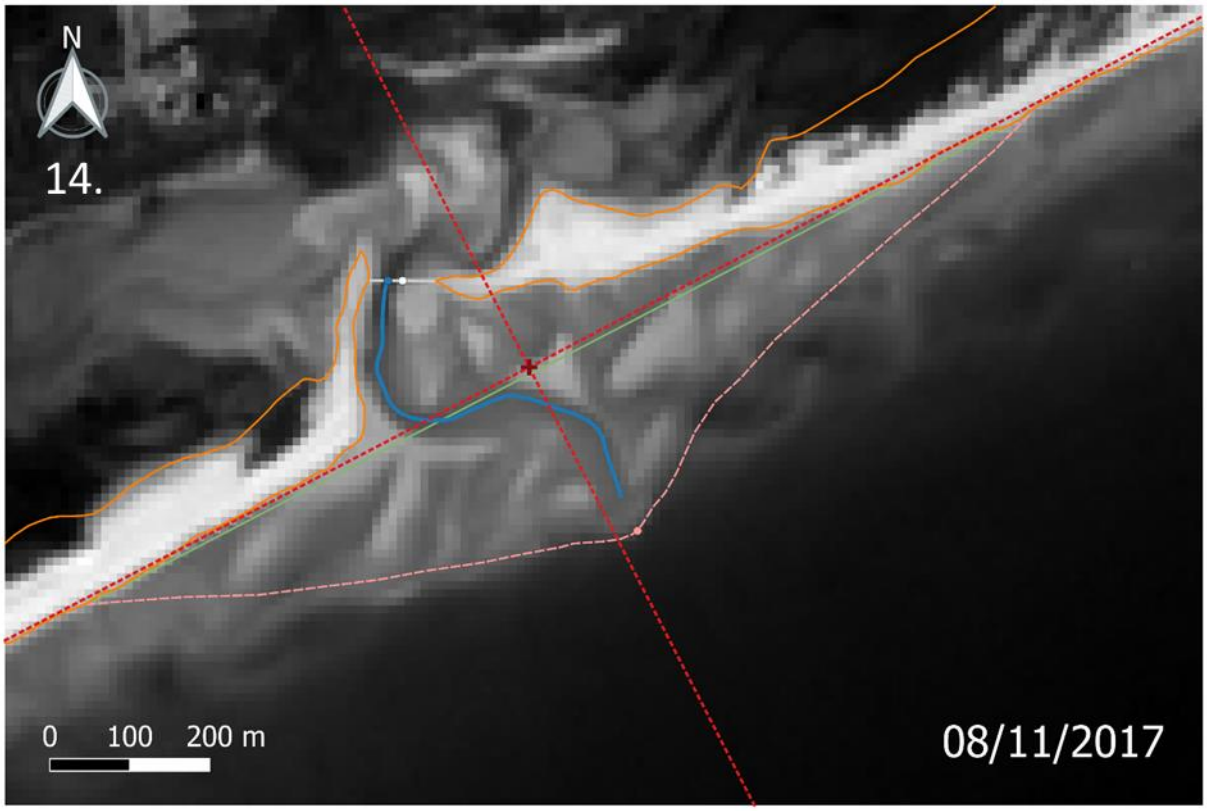
N
14.
0 100 200 m
08/11/2017

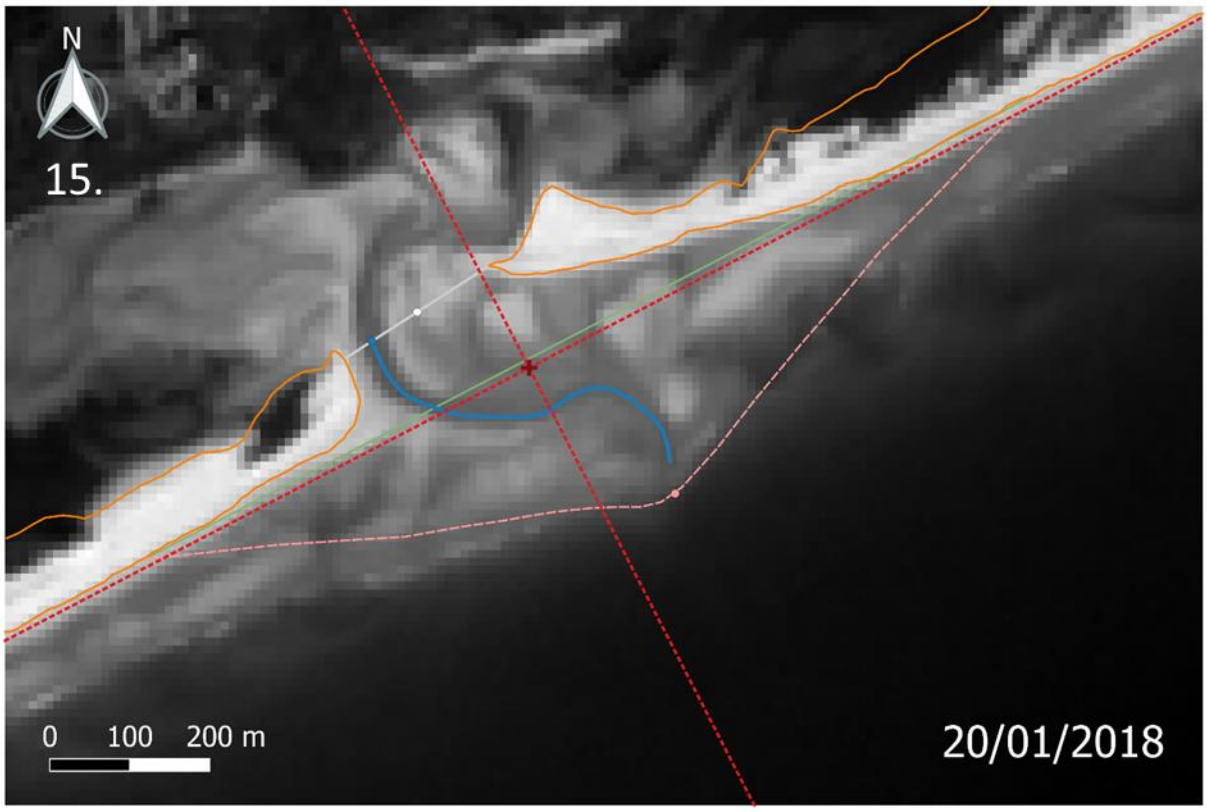
N
15.
0 100 200 m
20/01/2018

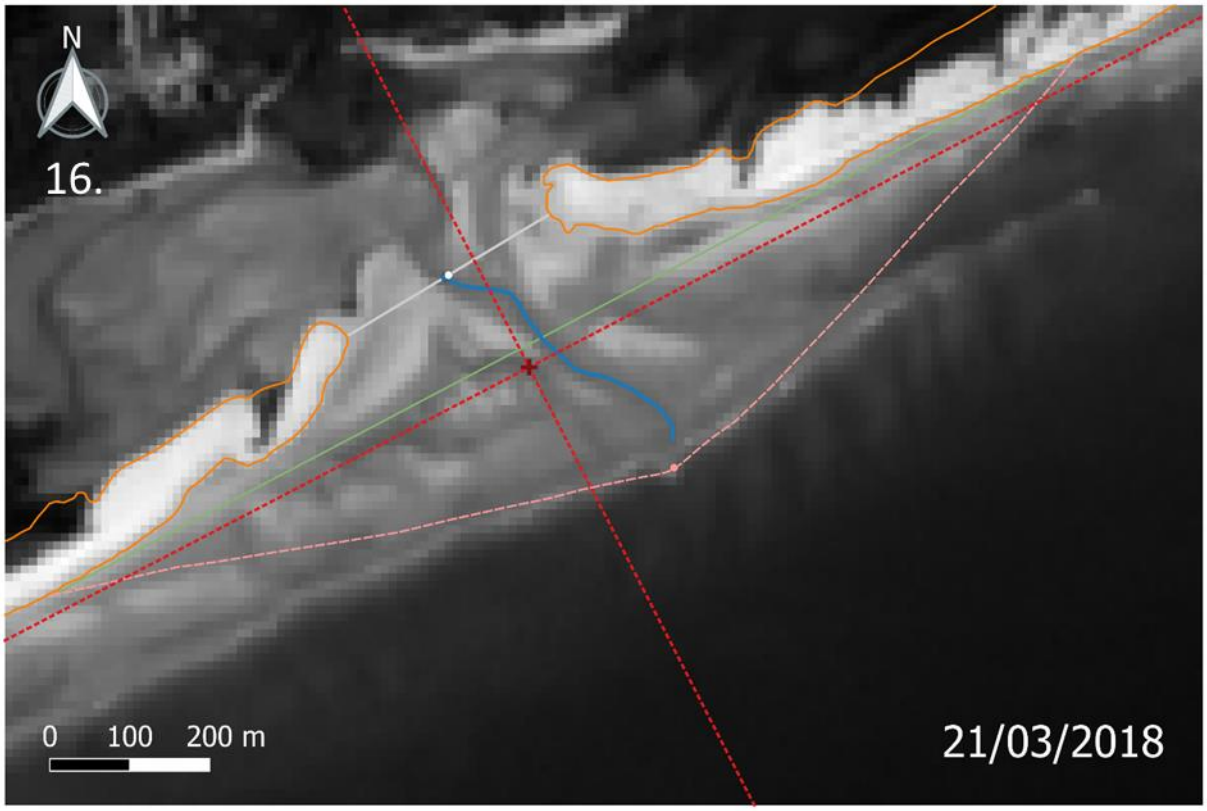
N
16.
0 100 200 m
21/03/2018

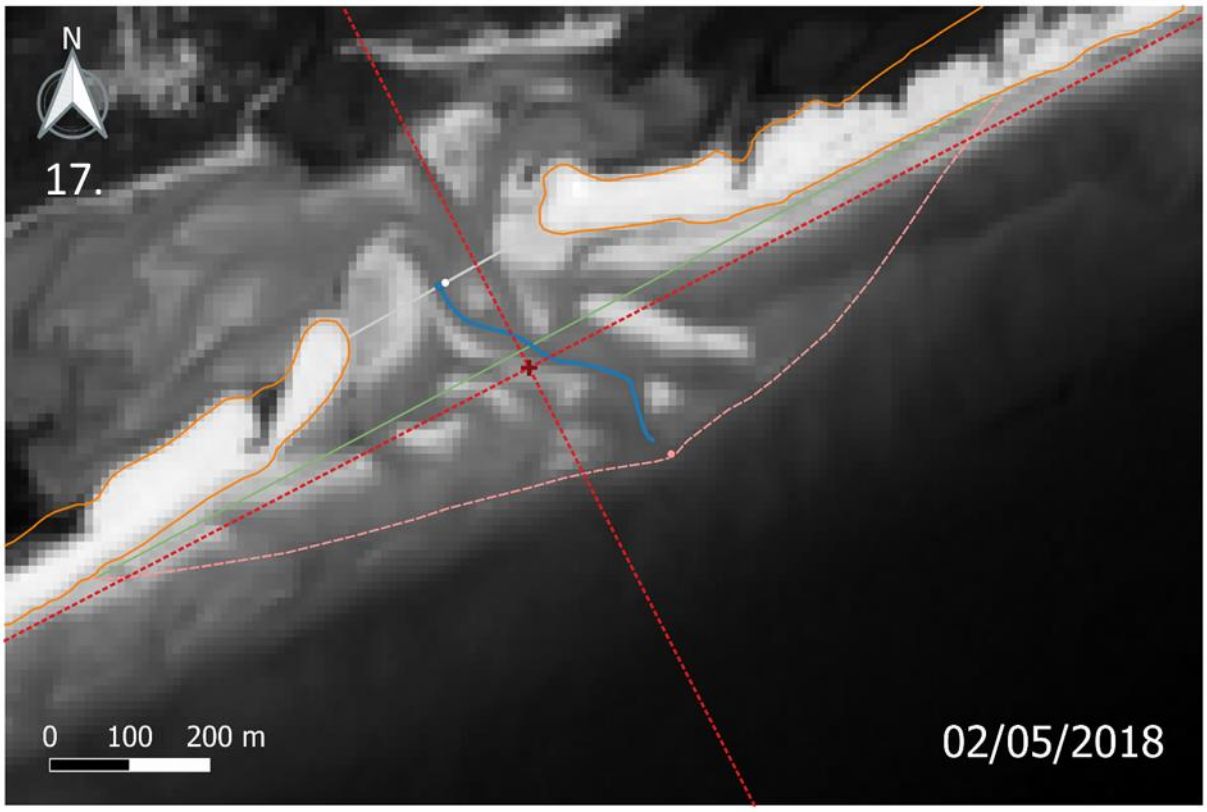
N
17.
0 100 200 m
02/05/2018

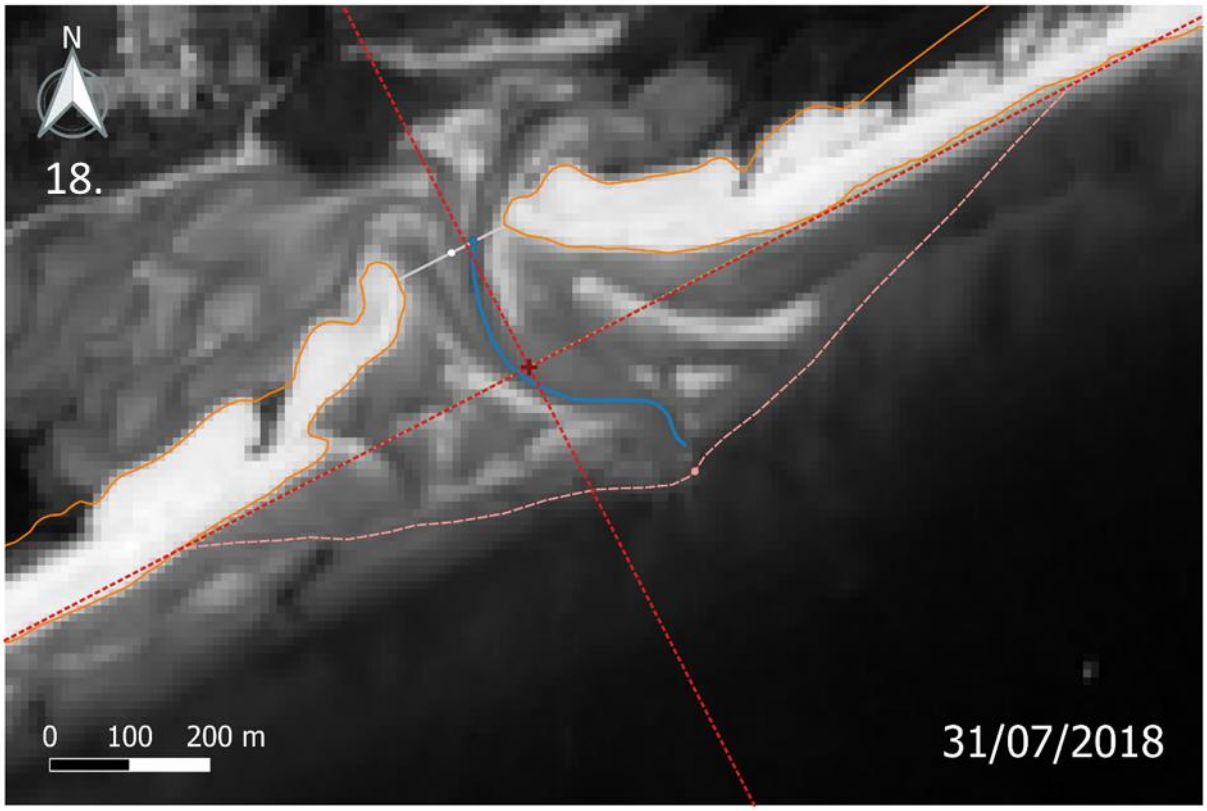
N
18.
0 100 200 m
31/07/2018

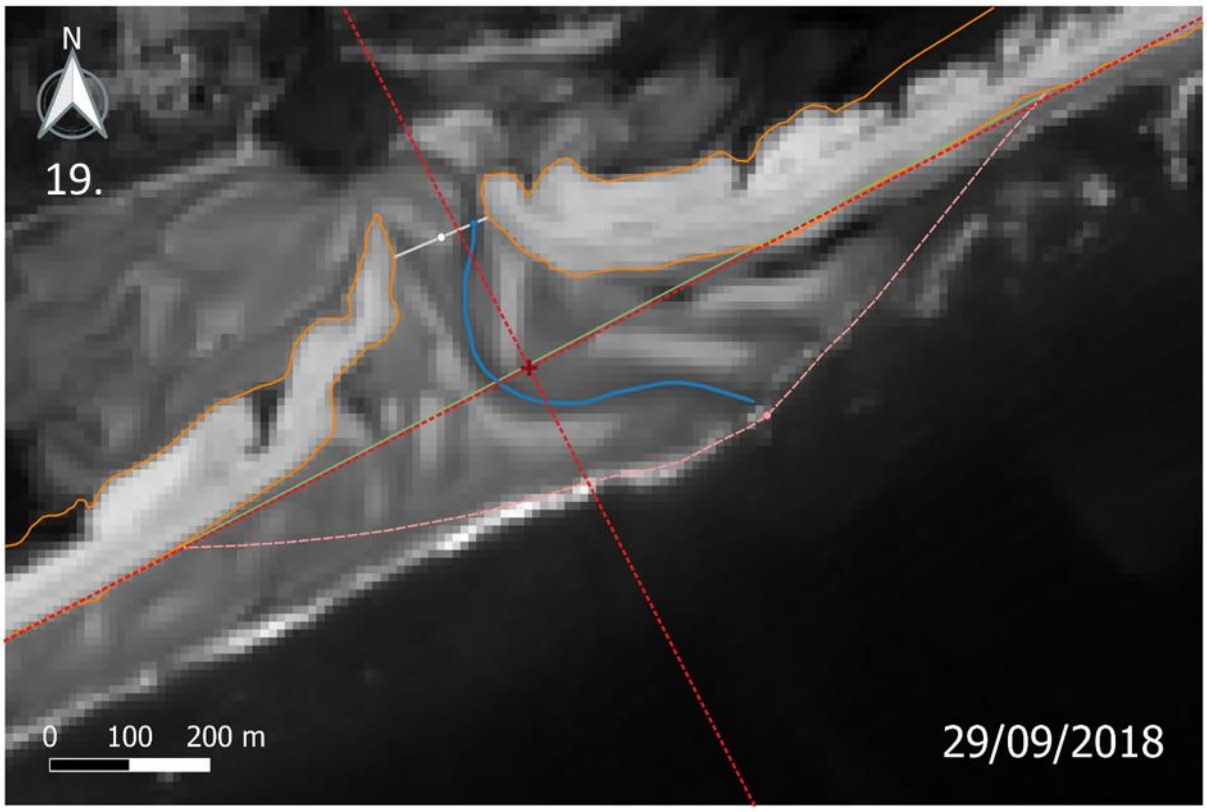
N
19.
0 100 200 m
29/09/2018

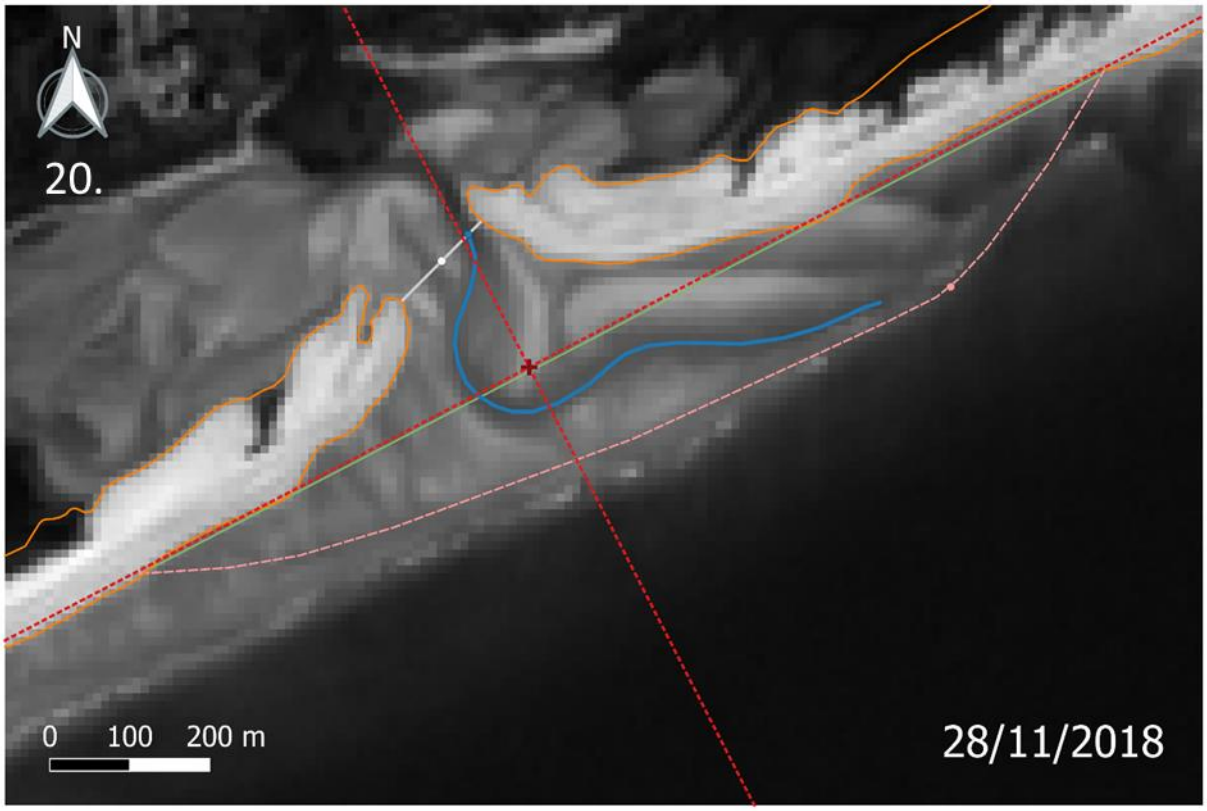
N
20.
0 100 200 m
28/11/2018

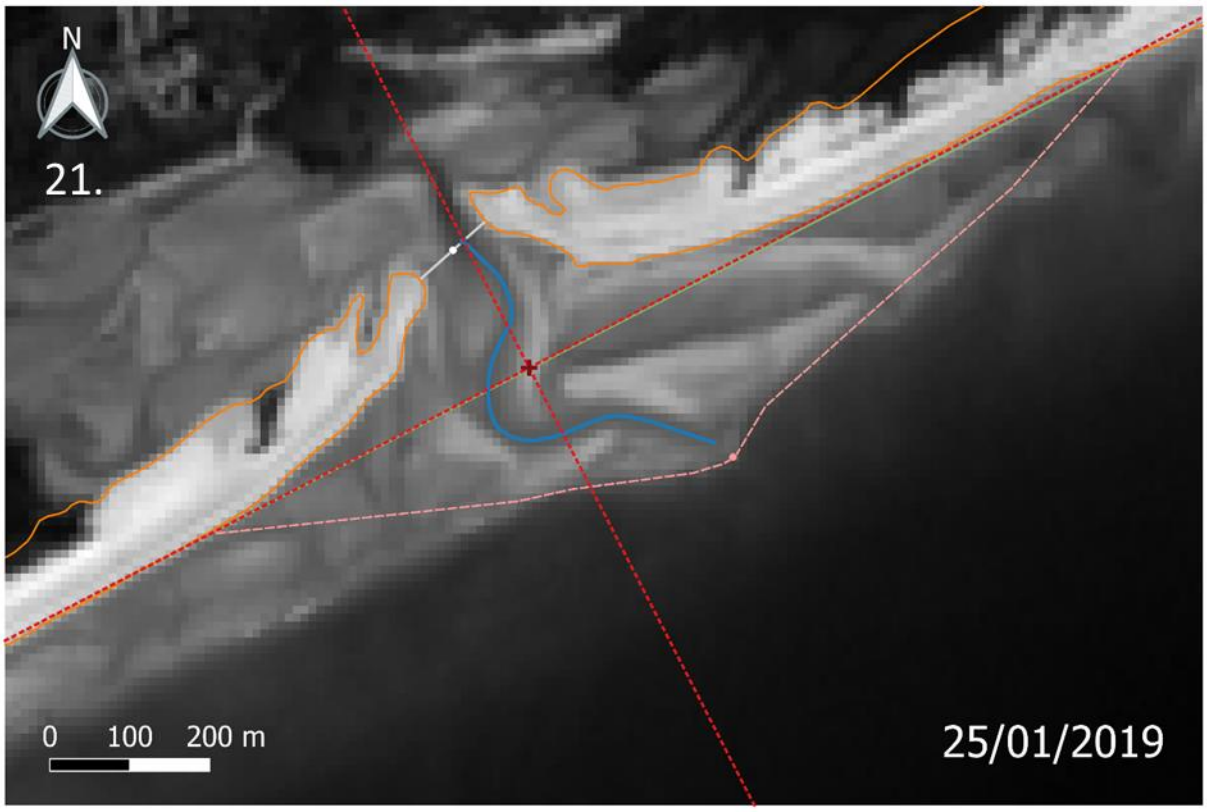
N
21.
0 100 200 m
25/01/2019

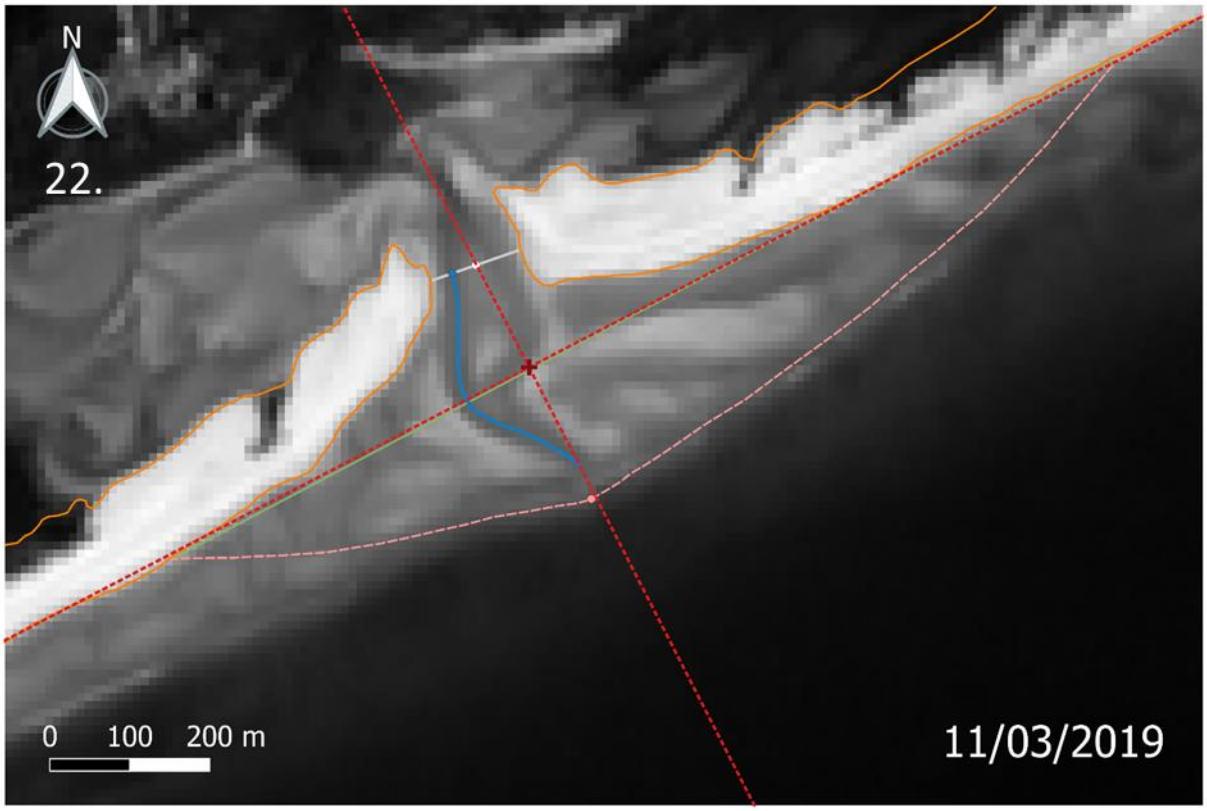
N
22.
0 100 200 m
11/03/2019

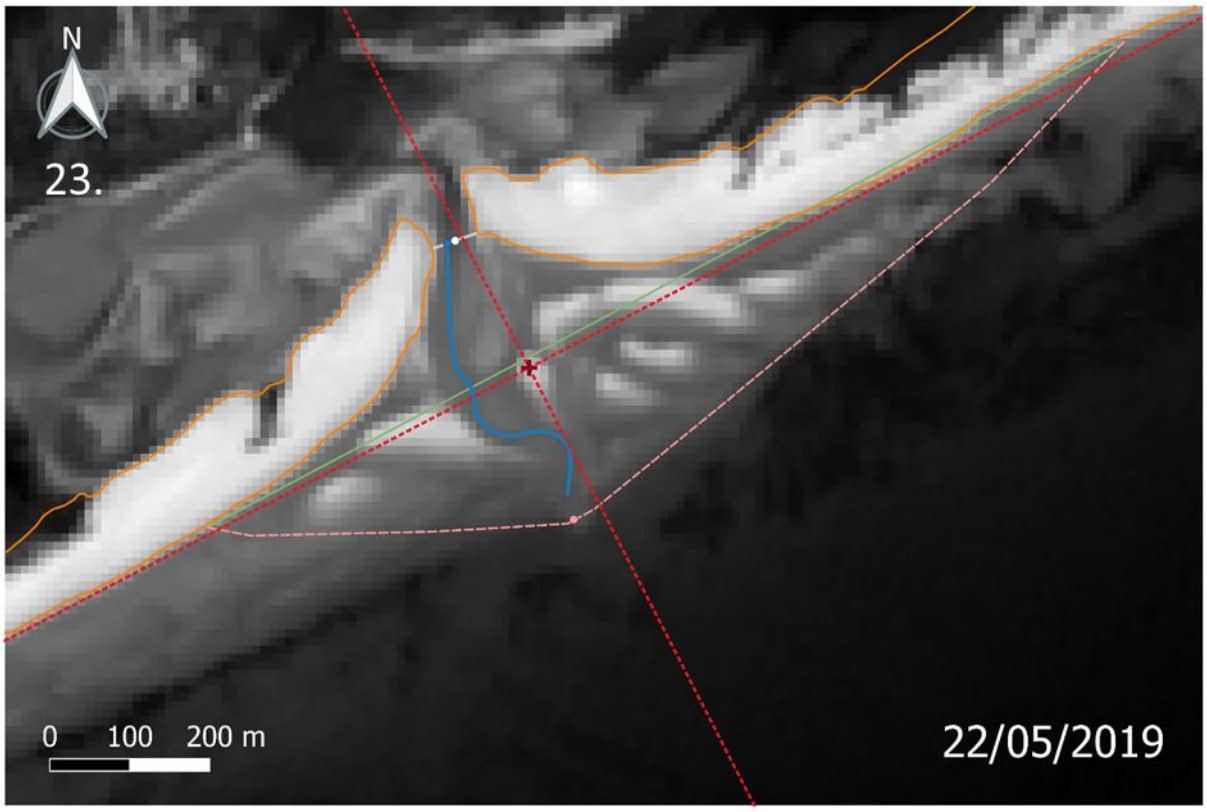
N
23.
0 100 200 m
22/05/2019

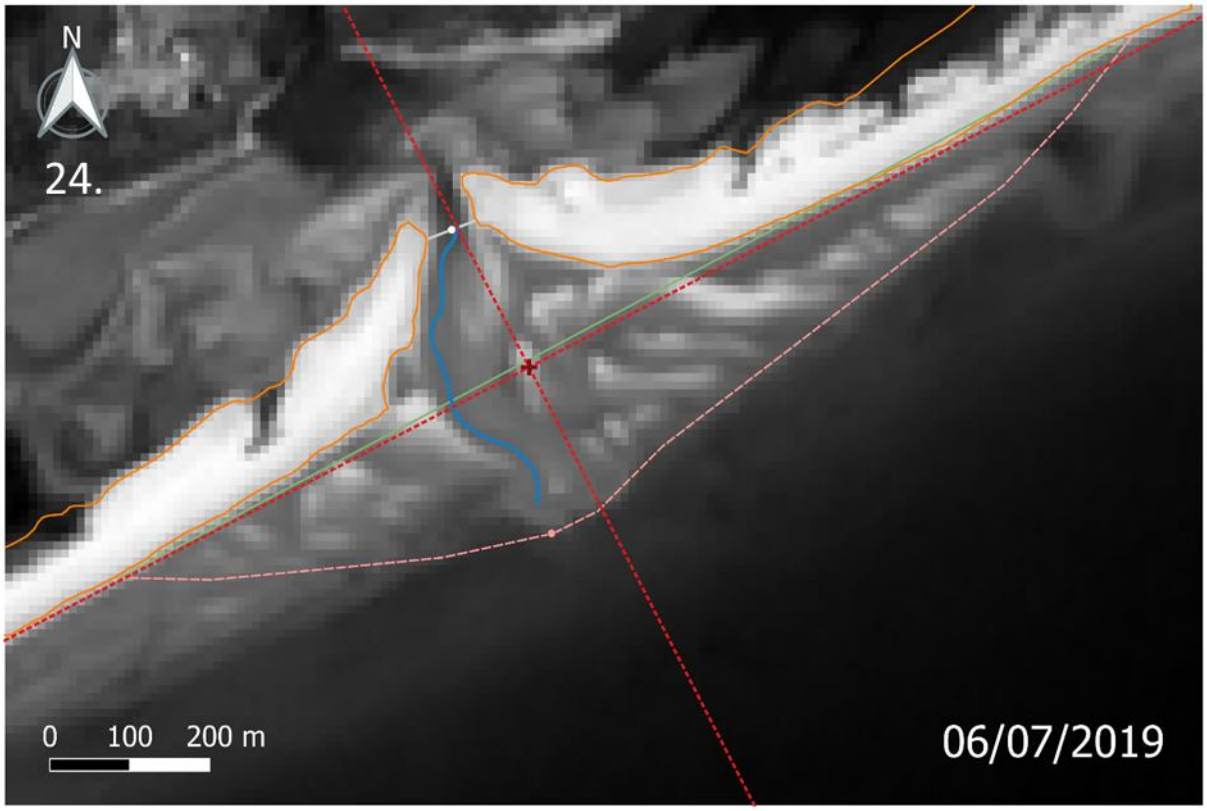
N
24.
0 100 200 m
06/07/2019

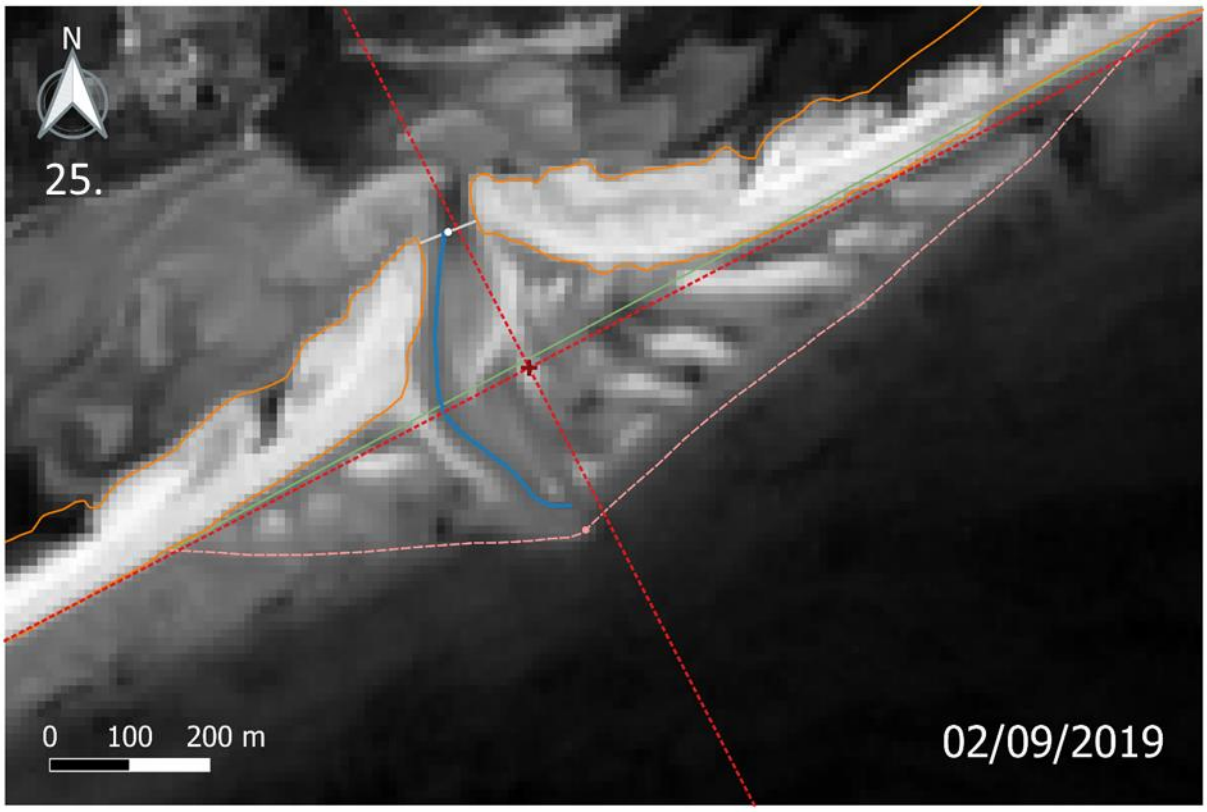
N
25.
0 100 200 m
02/09/2019

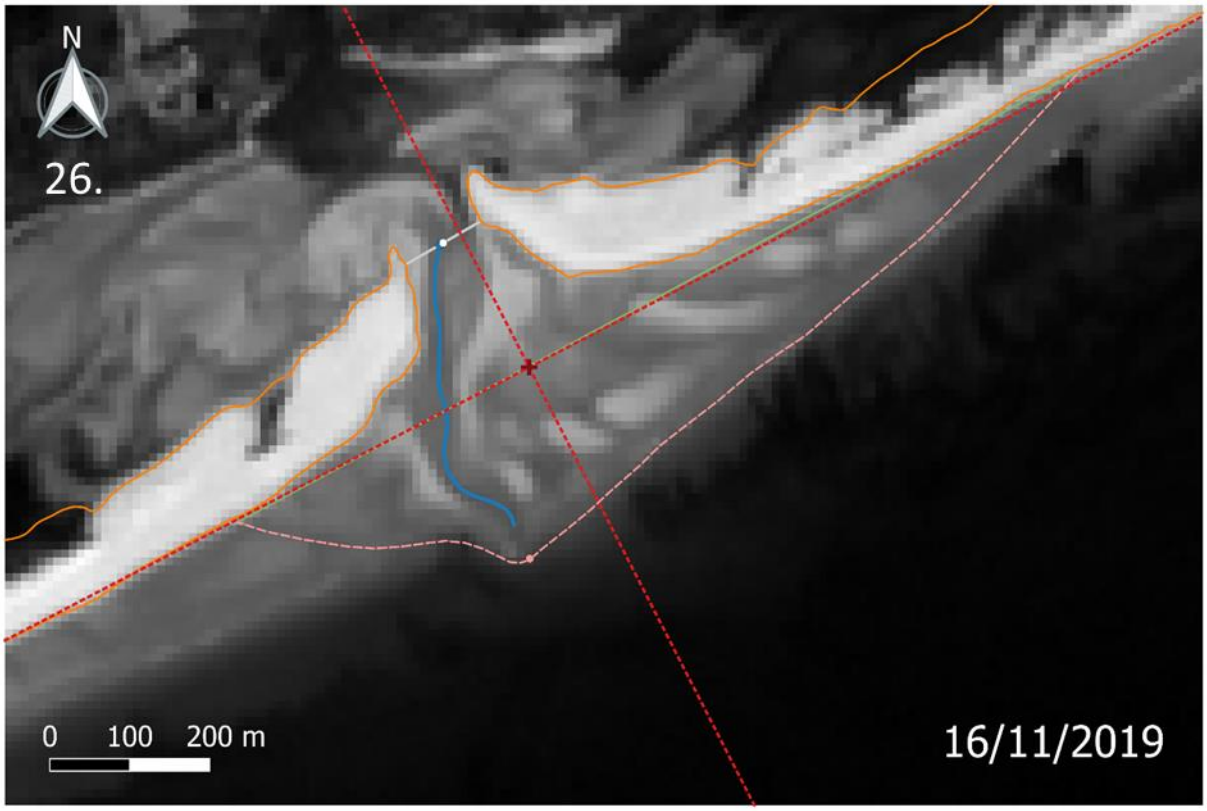
N
26.
0 100 200 m
16/11/2019

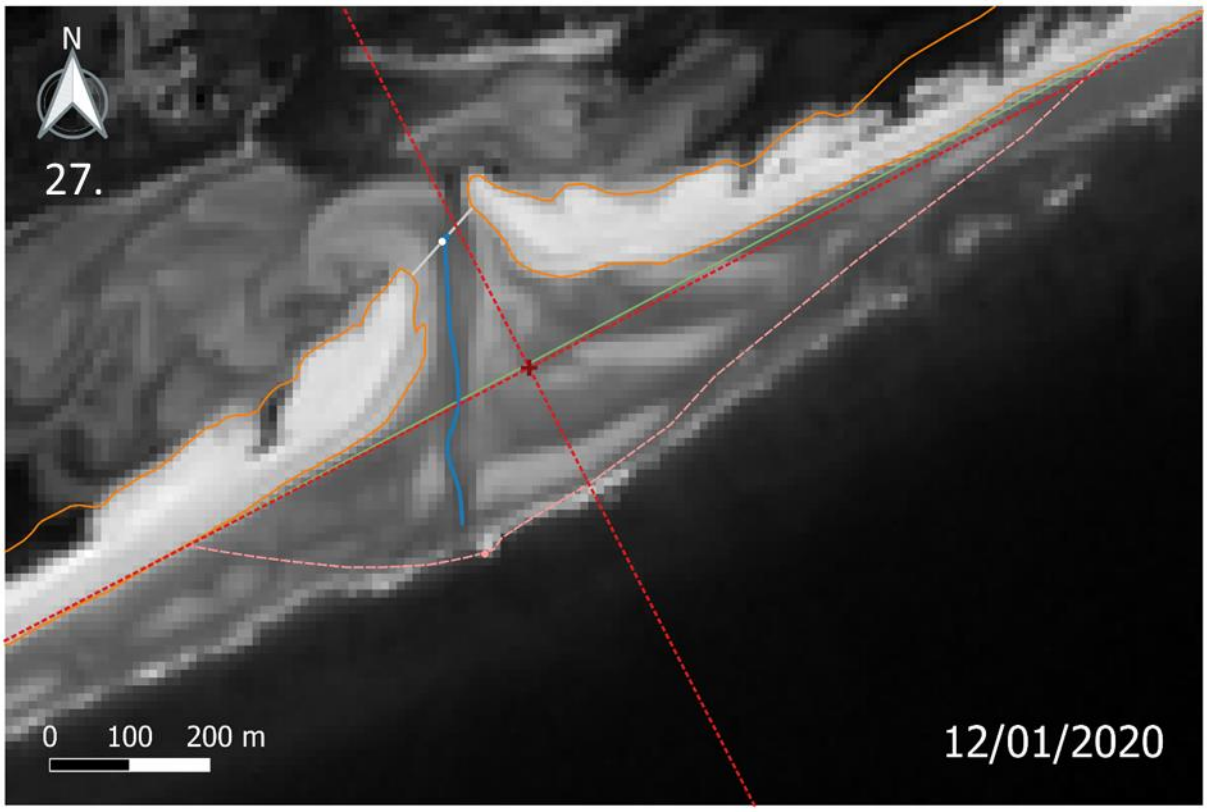
N
27.
0 100 200 m
12/01/2020

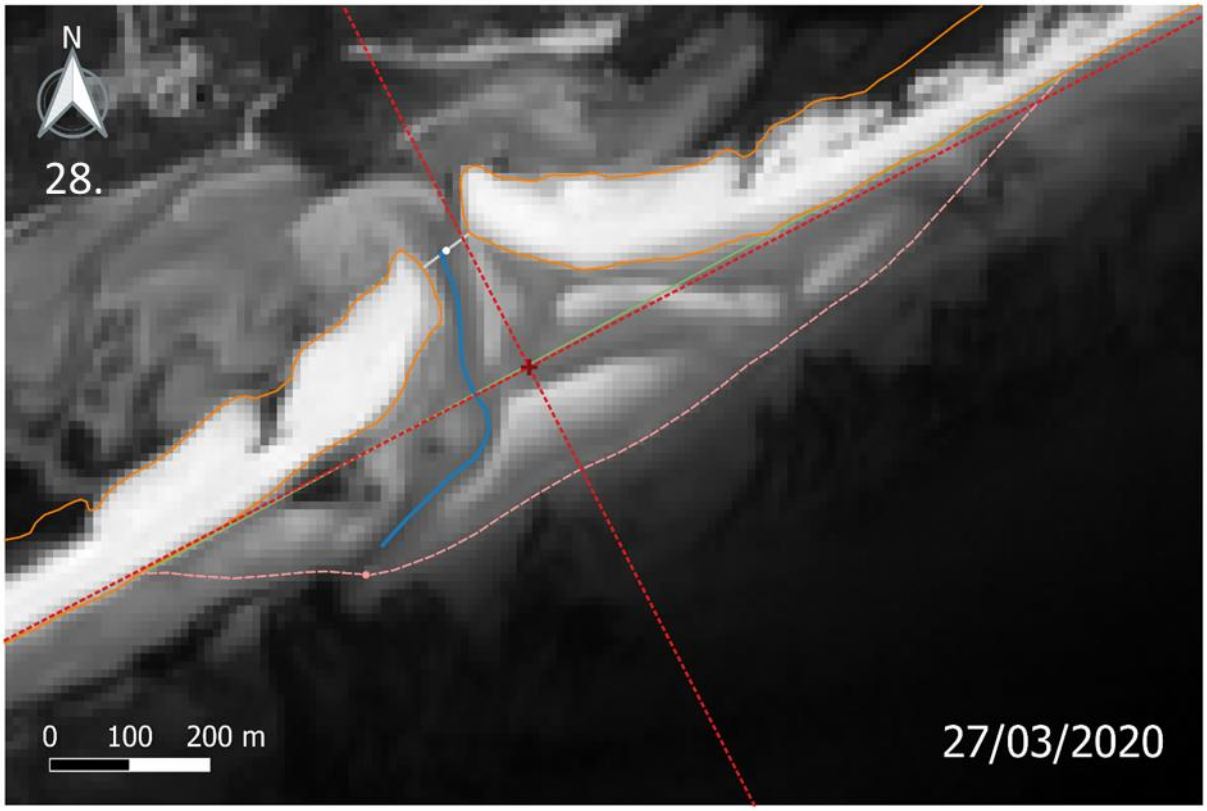
N
28.
0 100 200 m
27/03/2020

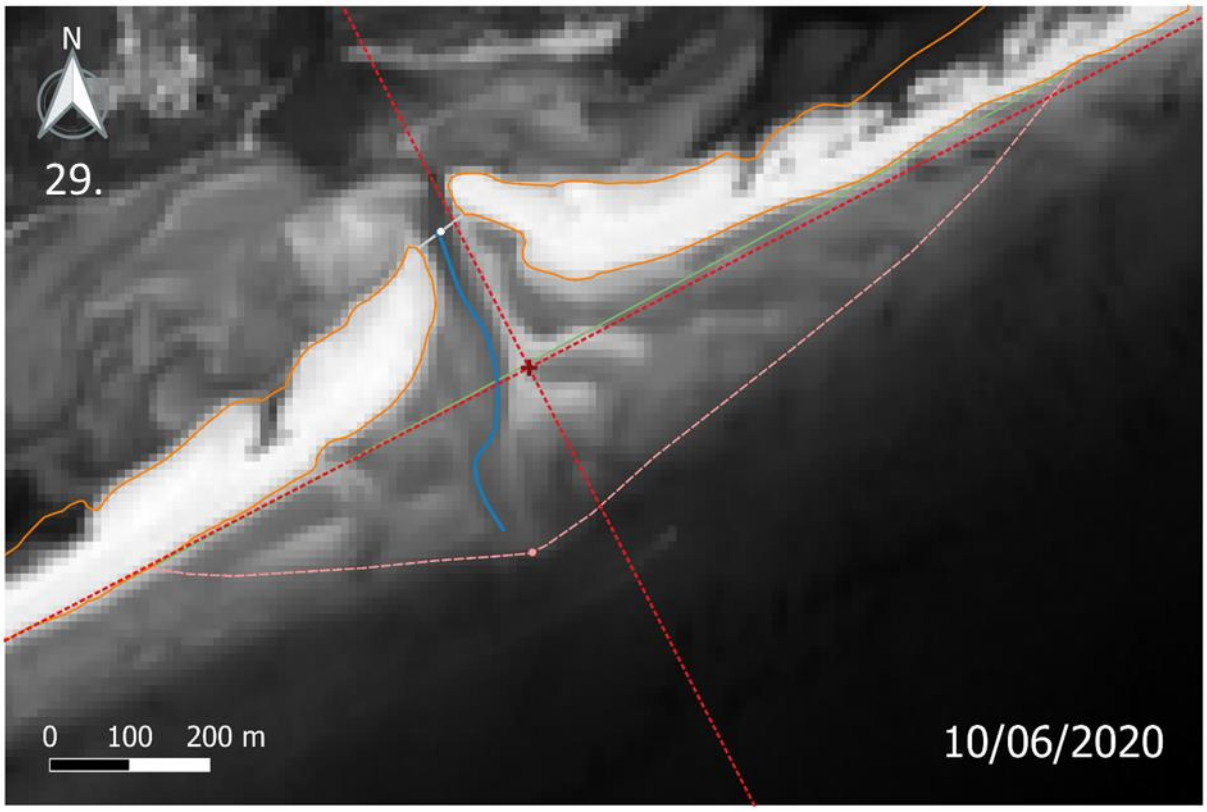
N
29.
0 100 200 m
10/06/2020

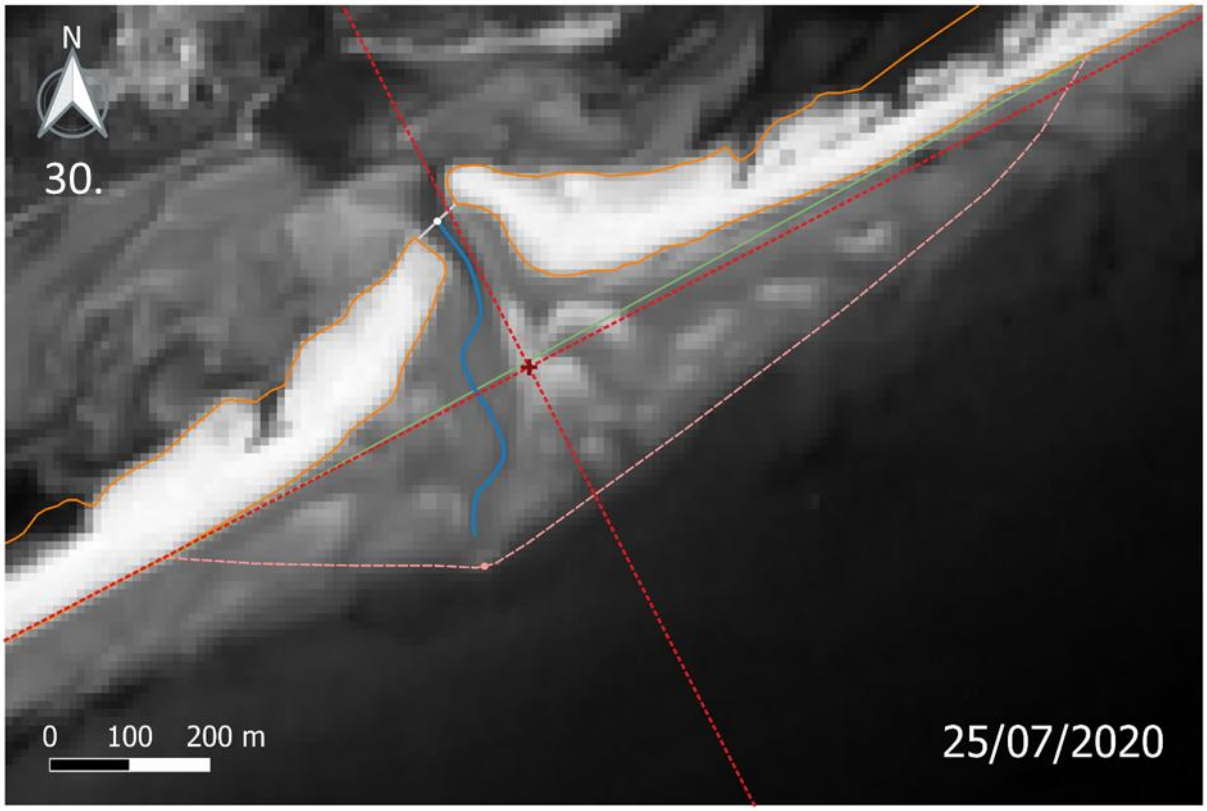
N
30.
0 100 200 m
25/07/2020

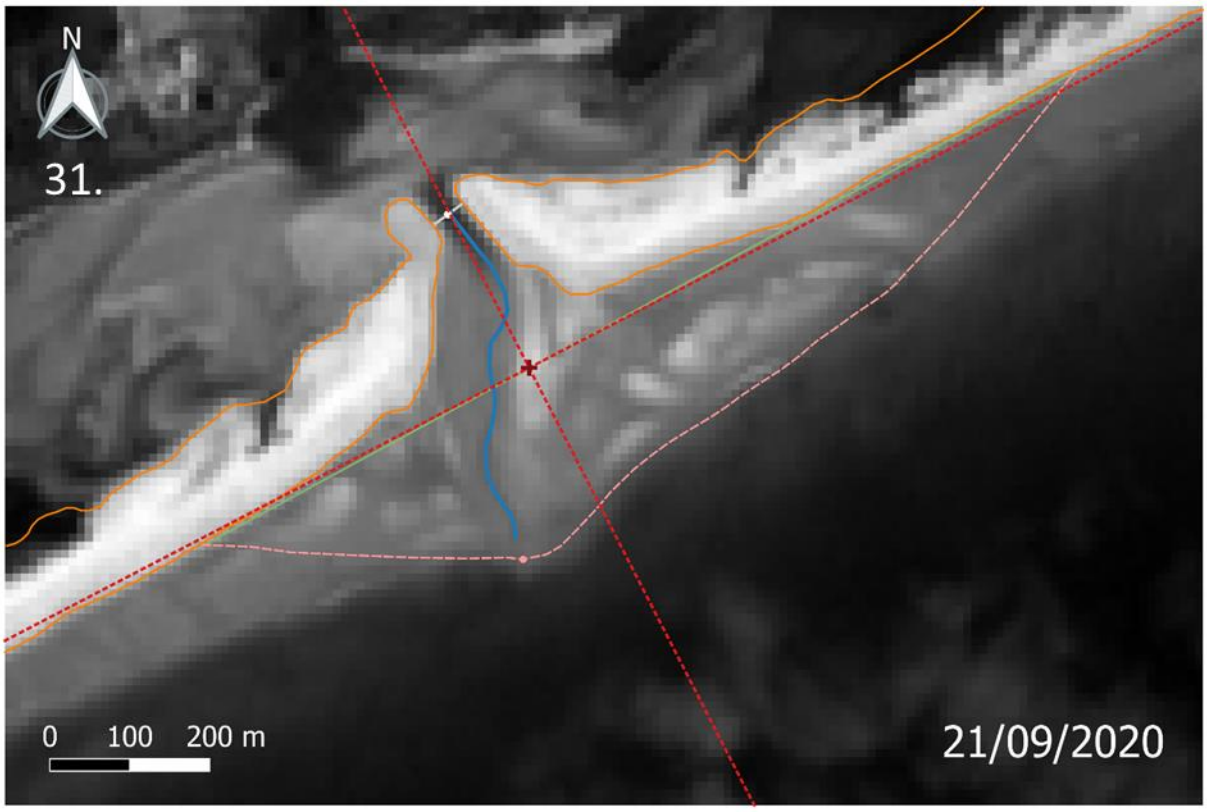
N
31.
0 100 200 m
21/09/2020

Appendix 2 - Cacela ebb-tidal delta main ebb channel orientations for the selected images from September 2015 to September 2020

Legend: Dark grey: first image selection, light grey: second image selection, red: straight N-S orientation, light red: deflected N-S orientation, green: straight NW-SE orientation, light green: deflected NW-SE orientation, blue: straight W-E orientation, light blue: deflected W-E orientation, yellow: straight NE-SW orientation, light yellow: deflected NE-SW orientation

Date	30/09/2015	29/11/2015	29/12/2015	28/03/2016	06/06/2016	05/08/2016	04/09/2016	16/11/2016
Channel upper orientation (close to the inlet) (° from the North)	163	163	165	186	187	192	191	200
Channel lower orientation (across the delta) (° from the North)	110	170	160	108	151	122	191	132
Channel evolution across the delta	Deflected to the east	Straight to the south	Slightly deflected to the south-east	Deflected to the east	Slightly deflected to the south-east	Deflected to the south-east	Straight to the south	Deflected to the south-east
								

Date	15/01/2017	02/04/2017	11/07/2017	23/08/2017	24/09/2017	08/11/2017	20/01/2018	21/03/2018
Channel upper orientation (close to the inlet) (° from the North)	194	190	164	157	170	162	136	122
Channel lower orientation (across the delta) (° from the North)	150	121	126	171	122	115	104	129
Channel evolution across the delta	Slightly deflected to the south-east	Deflected to the south-east	Deflected to the south-east	Deflected to the south	Deflected to the south-east	Deflected to the south-east	Slightly deflected to the east	Straight to the south-east
								

Date	02/05/2018	31/07/2018	29/09/2018	28/11/2018	25/01/2019	11/03/2019	22/05/2019	06/07/2019
Channel upper orientation (close to the inlet) (° from the North)	122	161	171	177	171	174	169	183
Channel lower orientation (across the delta) (° from the North)	128	115	95	77	101	122	138	141
Channel evolution across the delta	Straight to the south-east	Deflected to the south-east	Deflected to the east	Deflected to the east	Deflected to the east	Deflected to the south-east	Deflected to the south-east	Slightly deflected to the south-east
								

Date	02/09/2019	16/11/2019	12/01/2020	27/03/2020	10/06/2020	25/07/2020	21/09/2020
Channel upper orientation (close to the inlet) (° from the North)	182	177	176	166	160	168	166
Channel lower orientation (across the delta) (° from the North)	130	149	178	213	177	178	171
Channel evolution across the delta	Deflected to the south-east	Slightly deflected to the south-east	Straight to the south	Deflected to the south-west	Almost straight to the south	Slightly deflected to the south	Slightly deflected to the south
							

Appendix 3 - Table of the parameters of the Cacela Inlet and ebb-tidal delta for the selected images from September 2015 to September 2020

Date	30/09/2015	29/11/2015	29/12/2015	28/03/2016	06/06/2016	05/08/2016	04/09/2016	16/11/2016
Inlet width (m)	123	107	74	87	75	98	99	78
Inlet mean x position (x_UTM29N)(m)	629508	629510	629517	629521	629524	629503	629506	629505
Inlet mean y position (y_UTM29N)(m)	4113062	4113117	4113165	4113173	4113208	4113164	4113168	4113127
Inlet mean x position according reference point (m)	-48	-46	-39	-35	-33	-53	-51	-51
Inlet mean y position according reference point (m)	115	169	218	226	261	217	220	180
Inlet mean along-shore position (m)	11	38	66	73	92	54	57	38
Inlet mean cross-shore position (m)	124	171	211	216	246	217	219	183
Channel at inlet mean x position (x_UTM29N)(m)	629538	629521	629529	629525	629533	629525	629535	629523
Channel at inlet mean y position (y_UTM29N)(m)	4113078	4113120	4113162	4113173	4113209	4113164	4113171	4113123
Channel at inlet mean x position according reference point (m)	-18	-35	-27	-31	-24	-32	-22	-33
Channel at inlet mean y position according reference point (m)	131	173	215	226	262	216	224	175
Channel at inlet mean along-shore position (m)	44	49	75	77	100	72	85	52
Channel at inlet mean cross-shore position (m)	125	170	203	215	243	206	209	171
Delta tip mean x position (x_UTM29N)(m)	629803	629615	629657	629778	629584	629664	629430	629605
Delta tip mean y position (y_UTM29N)(m)	4112870	4112707	4112775	4112838	4112737	4112751	4112696	4112747
Delta tip mean x position according reference point (m)	247	58	101	221	28	108	-127	48
Delta tip mean y position according reference point (m)	-77	-240	-172	-109	-210	-196	-251	-201
Delta tip mean along-shore position (m)	183	-60	10	146	-72	4	-228	-50
Delta tip mean cross-shore position (m)	-183	-240	-200	-200	-199	-224	-164	-200

Date	15/01/2017	02/04/2017	11/07/2017	23/08/2017	24/09/2017	08/11/2017	20/01/2018	21/03/2018
Inlet width (m)	95	86	56	72	84	85	215	295
Inlet mean x position (x_UTM29N)(m)	629497	629488	629451	629450	629435	629398	629416	629455
Inlet mean y position (y_UTM29N)(m)	4113149	4113074	4113067	4113075	4113075	4113055	4113017	4113062
Inlet mean x position according reference point (m)	-60	-69	-105	-106	-121	-158	-140	-101
Inlet mean y position according reference point (m)	202	127	120	128	128	108	70	115
Inlet mean along-shore position (m)	40	-2	-38	-35	-48	-90	-92	-36
Inlet mean cross-shore position (m)	206	144	155	163	169	169	127	149
Channel at inlet mean x position (x_UTM29N)(m)	629517	629477	629442	629433	629442	629379	629359	629451
Channel at inlet mean y position (y_UTM29N)(m)	4113136	4113074	4113071	4113083	4113071	4113055	4112980	4113060
Channel at inlet mean x position according reference point (m)	-40	-80	-115	-124	-114	-177	-197	-105
Channel at inlet mean y position according reference point (m)	188	126	124	135	124	108	33	113
Channel at inlet mean along-shore position (m)	52	-12	-44	-47	-44	-107	-159	-41
Channel at inlet mean cross-shore position (m)	185	149	163	177	163	178	121	149
Delta tip mean x position (x_UTM29N)(m)	629570	629646	629630	629529	629676	629692	629739	629738
Delta tip mean y position (y_UTM29N)(m)	4112698	4112757	4112795	4112692	4112778	4112743	4112790	4112822
Delta tip mean x position according reference point (m)	14	90	74	-27	120	136	183	182
Delta tip mean y position according reference point (m)	-249	-190	-152	-256	-169	-204	-157	-126
Delta tip mean along-shore position (m)	-103	-8	-5	-143	28	26	89	103
Delta tip mean cross-shore position (m)	-227	-210	-169	-214	-206	-244	-224	-195

Date	02/05/2018	31/07/2018	29/09/2018	28/11/2018	25/01/2019	11/03/2019	22/05/2019	06/07/2019
Inlet width (m)	280	151	128	143	109	117	60	67
Inlet mean x position (x_UTM29N)(m)	629451	629459	629446	629447	629461	629490	629464	629459
Inlet mean y position (y_UTM29N)(m)	4113054	4113090	4113111	4113080	4113094	4113075	4113106	4113119
Inlet mean x position according reference point (m)	-105	-97	-110	-110	-95	-67	-93	-97
Inlet mean y position according reference point (m)	107	143	163	133	147	128	159	172
Inlet mean along-shore position (m)	-44	-20	-22	-36	-16	0	-8	-6
Inlet mean cross-shore position (m)	143	172	196	168	175	144	184	197
Channel at inlet mean x position (x_UTM29N)(m)	629443	629487	629487	629480	629474	629460	629454	629464
Channel at inlet mean y position (y_UTM29N)(m)	4113049	4113104	4113128	4113113	4113106	4113065	4113103	4113121
Channel at inlet mean x position according reference point (m)	-113	-70	-69	-76	-83	-96	-103	-93
Channel at inlet mean y position according reference point (m)	102	157	181	166	159	117	156	174
Channel at inlet mean along-shore position (m)	-53	11	22	9	0	-31	-19	-2
Channel at inlet mean cross-shore position (m)	143	171	192	182	179	149	185	197
Delta tip mean x position (x_UTM29N)(m)	629734	629764	629854	630084	629812	629634	629612	629584
Delta tip mean y position (y_UTM29N)(m)	4112839	4112817	4112888	4113048	4112836	4112783	4112757	4112740
Delta tip mean x position according reference point (m)	178	208	298	528	255	78	56	28
Delta tip mean y position according reference point (m)	-108	-130	-59	101	-112	-165	-190	-208
Delta tip mean along-shore position (m)	108	124	236	514	175	-7	-39	-71
Delta tip mean cross-shore position (m)	-178	-211	-191	-156	-217	-182	-194	-197

Date	02/09/2019	16/11/2019	12/01/2020	27/03/2020	10/06/2020	25/07/2020	21/09/2020
Inlet width (m)	77	108	115	72	73	65	45
Inlet mean x position (x_UTM29N)(m)	629455	629449	629447	629453	629446	629441	629454
Inlet mean y position (y_UTM29N)(m)	4113117	4113103	4113105	4113093	4113118	4113130	4113139
Inlet mean x position according reference point (m)	-101	-108	-109	-104	-111	-115	-102
Inlet mean y position according reference point (m)	170	155	158	146	171	183	192
Inlet mean along-shore position (m)	-11	-23	-23	-24	-19	-17	-1
Inlet mean cross-shore position (m)	198	188	190	177	202	215	217
Channel at inlet mean x position (x_UTM29N)(m)	629451	629444	629452	629448	629443	629441	629456
Channel at inlet mean y position (y_UTM29N)(m)	4113116	4113100	4113111	4113090	4113116	4113130	4113140
Channel at inlet mean x position according reference point (m)	-105	-112	-104	-108	-113	-115	-100
Channel at inlet mean y position according reference point (m)	169	153	164	142	169	183	193
Channel at inlet mean along-shore position (m)	-15	-29	-16	-30	-22	-17	1
Channel at inlet mean cross-shore position (m)	198	187	193	176	202	215	218
Delta tip mean x position (x_UTM29N)(m)	629627	629557	629501	629352	629560	629500	629549
Delta tip mean y position (y_UTM29N)(m)	4112744	4112708	4112714	4112688	4112716	4112699	4112707
Delta tip mean x position according reference point (m)	71	1	-55	-204	4	-56	-7
Delta tip mean y position according reference point (m)	-203	-239	-233	-259	-231	-249	-240
Delta tip mean along-shore position (m)	-31	-110	-157	-301	-103	-165	-118
Delta tip mean cross-shore position (m)	-213	-212	-181	-135	-206	-194	-209

Appendix 4 - Table with the parameters change and rate of change of the Cacela Inlet and ebb-tidal delta between the selected images from September 2015 to September 2020

Date	30/09/2015 to 29/11/2015	29/11/2015 to 29/12/2015	29/12/2015 to 28/03/2016	28/03/2016 to 06/06/2016	06/06/2016 to 05/05/2016	05/08/2016 to 04/09/2016	04/09/2016 to 16/11/2016	16/11/2016 to 15/01/2017
Upper channel orientation change between images (°)	0	2	21	1	5	-1	9	-6
Upper channel orientation rate of change between image (°/day)	0,00	0,07	0,23	0,01	0,08	-0,03	0,12	-0,10
Lower channel orientation change between images (°)	60	-10	-52	43	-29	69	-59	18
Lower channel orientation rate of change between image (°/day)	1,00	-0,33	-0,58	0,61	-0,48	2,30	-0,81	0,30
Inlet width change between images (m)	-15	-34	13	-12	23	2	-21	17
Inlet width rate of change between images (m/day)	-0,25	-1,12	0,14	-0,16	0,38	0,05	-0,29	0,28
Inlet along-shore change between images (m)	27	29	7	19	-38	4	-19	3
Inlet along-shore rate of change between images (m/day)	0,45	0,96	0,08	0,27	-0,64	0,12	-0,27	0,04
Inlet cross-shore change between images (m)	48	40	5	30	-30	2	-35	23
Inlet cross-shore rate of change between images (m/day)	0,79	1,32	0,06	0,43	-0,49	0,07	-0,49	0,38
Channel at inlet along-shore change between images (m)	4	26	2	23	-28	13	-33	0
Channel at inlet along-shore rate of change between images (m/day)	0,07	0,88	0,02	0,33	-0,47	0,42	-0,45	0,00
Channel at inlet cross-shore change between images (m)	45	33	12	28	-36	2	-38	15
Channel at inlet cross-shore rate of change between images (m/day)	0,76	1,11	0,13	0,40	-0,61	0,08	-0,52	0,24
Delta tip along-shore change between images (m)	-243	69	136	-218	77	-233	178	-53
Delta tip along-shore rate of change between images (m/day)	-4,04	2,31	1,51	-3,11	1,28	-7,76	2,44	-0,88
Delta tip cross-shore change between images (m)	-57	40	0	0	-25	60	-37	-27
Delta tip cross-shore rate of change between images (m/day)	-0,95	1,35	0,00	0,01	-0,41	2,01	-0,50	-0,45

Date	15/01/2017 to 02/04/2017	02/04/2017 to 11/04/2017	11/07/2017 to 23/08/2017	23/08/2017 to 24/09/2017	24/09/2017 to 08/11/2017	08/11/2017 to 20/01/2018	20/01/2018 to 21/03/2018	21/03/2018 to 02/05/2018
Upper channel orientation change between images (°)	-4	-26	-7	13	-8	-26	-14	0
Upper channel orientation rate of change between image (°/day)	-0,05	-0,26	-0,16	0,41	-0,18	-0,36	-0,23	0,00
Lower channel orientation change between images (°)	-29	5	45	-49	-7	-11	25	-1
Lower channel orientation rate of change between image (°/day)	-0,38	0,05	1,05	-1,53	-0,16	-0,15	0,42	-0,02
Inlet width change between images (m)	-9	-30	16	11	1	130	80	-16
Inlet width rate of change between images (m/day)	-0,11	-0,30	0,37	0,35	0,02	1,78	1,34	-0,38
Inlet along-shore change between images (m)	-43	-36	3	-13	-42	-2	56	-8
Inlet along-shore rate of change between images (m/day)	-0,55	-0,36	0,07	-0,41	-0,94	-0,02	0,93	-0,18
Inlet cross-shore change between images (m)	-62	11	8	6	0	-42	22	-6
Inlet cross-shore rate of change between images (m/day)	-0,81	0,11	0,18	0,19	0,00	-0,58	0,37	-0,14
Channel at inlet along-shore change between images (m)	-64	-32	-3	3	-63	-52	118	-12
Channel at inlet along-shore rate of change between images (m/day)	-0,83	-0,32	-0,06	0,09	-1,40	-0,72	1,97	-0,28
Channel at inlet cross-shore change between images (m)	-36	14	14	-15	15	-57	28	-6
Channel at inlet cross-shore rate of change between images (m/day)	-0,47	0,14	0,33	-0,46	0,34	-0,78	0,46	-0,14
Delta tip along-shore change between images (m)	95	3	-137	171	-2	63	14	5
Delta tip along-shore rate of change between images (m/day)	1,23	0,03	-3,20	5,33	-0,05	0,87	0,23	0,12
Delta tip cross-shore change between images (m)	17	41	-45	8	-39	20	29	17
Delta tip cross-shore rate of change between images (m/day)	0,23	0,41	-1,04	0,26	-0,86	0,27	0,48	0,42

Date	02/05/2018 to 31/07/2018	31/07/2018 to 29/09/2018	29/09/2018 to 28/11/2018	28/11/2018 to 25/01/2019	25/01/2019 to 11/03/2019	11/03/2019 to 22/05/2019	22/05/2019 to 06/07/2019	06/07/2019 to 02/09/2019
Upper channel orientation change between images (°)	39	10	6	-6	3	-5	14	-1
Upper channel orientation rate of change between image (°/day)	0,43	0,17	0,10	-0,10	0,07	-0,07	0,31	-0,02
Lower channel orientation change between images (°)	-13	-20	-18	24	21	16	3	-11
Lower channel orientation rate of change between image (°/day)	-0,14	-0,33	-0,30	0,41	0,47	0,22	0,07	-0,19
Inlet width change between images (m)	-129	-23	15	-34	8	-57	7	10
Inlet width rate of change between images (m/day)	-1,43	-0,38	0,25	-0,58	0,18	-0,79	0,15	0,18
Inlet along-shore change between images (m)	24	-2	-14	19	16	-8	2	-5
Inlet along-shore rate of change between images (m/day)	0,26	-0,03	-0,23	0,33	0,36	-0,11	0,04	-0,08
Inlet cross-shore change between images (m)	29	24	-27	6	-31	40	13	0
Inlet cross-shore rate of change between images (m/day)	0,32	0,40	-0,46	0,11	-0,68	0,55	0,30	0,01
Channel at inlet along-shore change between images (m)	64	11	-13	-9	-31	12	17	-13
Channel at inlet along-shore rate of change between images (m/day)	0,71	0,19	-0,21	-0,16	-0,69	0,17	0,38	-0,23
Channel at inlet cross-shore change between images (m)	29	21	-10	-4	-30	37	11	1
Channel at inlet cross-shore rate of change between images (m/day)	0,32	0,35	-0,16	-0,06	-0,67	0,51	0,25	0,02
Delta tip along-shore change between images (m)	16	113	278	-340	-182	-31	-33	40
Delta tip along-shore rate of change between images (m/day)	0,18	1,88	4,63	-5,86	-4,04	-0,43	-0,73	0,69
Delta tip cross-shore change between images (m)	-34	21	35	-62	35	-12	-3	-16
Delta tip cross-shore rate of change between images (m/day)	-0,37	0,35	0,59	-1,06	0,78	-0,17	-0,06	-0,27

Date	02/09/2019 to 16/11/2019	16/11/2019 to 12/01/2020	12/01/2020 to 27/03/2020	27/03/2020 to 10/06/2020	10/06/2020 to 25/07/2020	25/07/2020 to 21/09/2020
Upper channel orientation change between images (°)	-5	-1	-10	-6	8	-2
Upper channel orientation rate of change between image (°/day)	-0,07	-0,02	-0,13	-0,08	0,18	-0,03
Lower channel orientation change between images (°)	19	29	35	-36	1	-7
Lower channel orientation rate of change between image (°/day)	0,25	0,51	0,47	-0,48	0,02	-0,12
Inlet width change between images (m)	30	7	-43	1	-8	-19
Inlet width rate of change between images (m/day)	0,41	0,13	-0,58	0,01	-0,18	-0,33
Inlet along-shore change between images (m)	-12	0	-1	6	2	16
Inlet along-shore rate of change between images (m/day)	-0,16	0,00	-0,01	0,07	0,04	0,28
Inlet cross-shore change between images (m)	-10	3	-13	25	13	2
Inlet cross-shore rate of change between images (m/day)	-0,13	0,05	-0,18	0,33	0,28	0,04
Channel at inlet along-shore change between images (m)	-14	12	-14	8	5	18
Channel at inlet along-shore rate of change between images (m/day)	-0,18	0,22	-0,18	0,11	0,10	0,31
Channel at inlet cross-shore change between images (m)	-11	6	-17	26	13	3
Channel at inlet cross-shore rate of change between images (m/day)	-0,14	0,10	-0,22	0,34	0,29	0,04
Delta tip along-shore change between images (m)	-79	-47	-144	198	-61	47
Delta tip along-shore rate of change between images (m/day)	-1,05	-0,82	-1,93	2,64	-1,36	0,81
Delta tip cross-shore change between images (m)	0	32	45	-71	12	-15
Delta tip cross-shore rate of change between images (m/day)	0,00	0,56	0,61	-0,95	0,27	-0,25

Appendix 5 - Table with the parameters change and rate of change of the Cacela Inlet and ebb-tidal delta for the selected periods from September 2015 to September 2020

Date	Period I	Period II	Period III	Period J	Period S	Period IV	Period V
Total upper channel orientation change (°)	24	7	-58	-14	0	47	-3
Mean upper channel orientation rate of change between image (°/day)	0,08	0,02	-0,10	-0,23	0,00	0,10	0,02
Total Lower channel orientation change (°)	41	-1	-46	25	-1	10	33
Mean lower channel orientation rate of change between image (°/day)	0,18	0,33	-0,19	0,42	-0,02	0,05	0,07
Total inlet width change (m)	-48	20	120	80	-16	-219	-15
Mean inlet width rate of change (m/day)	-0,35	0,10	0,35	1,34	-0,38	-0,46	-0,03
Total inlet along-shore change (m)	81	-51	-132	56	-8	35	7
Mean inlet along-shore rate of change (m/day)	0,44	-0,18	-0,37	0,93	-0,18	0,10	0,02
Total inlet cross-shore change (m)	123	-40	-79	22	-6	41	33
Mean inlet cross-shore rate of change (m/day)	0,65	-0,13	-0,15	0,37	-0,14	0,04	0,09
Total channel at inlet along-shore change (m)	56	-48	-211	118	-12	34	20
Mean channel at inlet along-shore rate of change (m/day)	0,33	-0,12	-0,54	1,97	-0,28	0,00	0,07
Total channel at inlet cross-shore change (m)	118	-58	-65	28	-6	43	32
Mean channel at inlet cross-shore rate of change (m/day)	0,60	-0,20	-0,15	0,46	-0,14	0,05	0,09
Total delta tip along-shore change (m)	-255	-30	192	14	5	-146	-79
Mean delta tip along-shore rate of change (m/day)	-0,83	-1,23	0,70	0,23	0,12	-0,61	-0,22
Total delta tip cross-shore change (m)	-16	-28	3	29	17	-16	-15
Mean delta tip cross-shore rate of change (m/day)	0,10	0,16	-0,12	0,48	0,42	0,02	-0,01

Appendix 6 - Basic statistics of the results obtained for the Cacela Inlet and ebb-tidal delta for the selected images from September 2015 to September 2020

Basic statistic parameters	Mean	Maximum	Minimum
Upper channel orientation (° from the North)	170	200	122
Upper channel orientation change between images (°)	0	39	-26
Upper channel orientation rate of change between image (°/day)	0,01	0,43	-0,36
Lower channel orientation (° from the North)	139	213	77
Lower channel orientation change between images (°)	2	69	-59
Lower channel orientation rate of change between image (°/day)	0,07	2,30	-1,53
Inlet width (m)	108	295	45
Inlet width change between images (m)	-3	130	-129
Inlet width rate of change between images (m/day)	-0,03	1,78	-1,43
Inlet mean along-shore position (m)	-5	92	-92
Inlet along-shore change between images (m)	0	56	-43
Inlet along-shore rate of change between images (m/day)	0,01	0,96	-0,94
Inlet mean cross-shore position (m)	182	246	124
Inlet cross-shore change between images (m)	3	48	-62
Inlet cross-shore rate of change between images (m/day)	0,08	1,32	-0,81
Channel at inlet mean along-shore position (m)	-1	100	-159
Channel at inlet along-shore change between images (m)	-1	118	-64
Channel at inlet along-shore rate of change between images (m/day)	-0,01	1,97	-1,40
Channel at inlet mean cross-shore position (m)	181	243	121
Channel at inlet cross-shore change between images (m)	3	45	-57
Channel at inlet cross-shore rate of change between images (m/day)	0,07	1,11	-0,78
Delta tip mean along-shore position (m)	-1	514	-301
Delta tip along-shore change between images (m)	-10	278	-340
Delta tip along-shore rate of change between images (m/day)	-0,30	5,33	-7,76
Delta tip mean cross-shore position (m)	-199	-135	-244
Delta tip cross-shore change between images (m)	-1	60	-71
Delta tip cross-shore rate of change between images (m/day)	0,04	2,01	-1,06

Appendix 7 - Table of the cumulative and parameterized wave powers computed between the selected images from wave climate at SIMAR point 5024022 between September 2015 and September 2020

Date	30/09/2015 to 29/11/2015	29/11/2015 to 29/12/2015	29/12/2015 to 28/03/2016	28/03/2016 to 06/06/2016	06/06/2016 to 05/05/2016	05/08/2016 to 04/09/2016	04/09/2016 to 16/11/2016	16/11/2016 to 15/01/2017
Cumulative wave power in total (W/m)	6,65E+06	6,07E+06	8,06E+06	7,41E+06	2,68E+06	2,55E+06	5,33E+06	9,56E+06
Number of hours in total (h)	1427	716	2145	1678	1436	719	1749	1434
Parameterized wave power in total (W/m/h)	9,96E+03	1,64E+04	1,00E+04	9,33E+03	4,24E+03	5,38E+03	6,51E+03	1,33E+04
Cumulative eastern waves power (W/m)	3,09E+06	4,22E+06	2,47E+06	1,51E+06	2,40E+06	2,48E+06	2,84E+06	5,41E+06
Cumulative eastern waves power proportion (%)	46	69	31	20	90	98	53	57
Number of hours of eastern occurrence (h)	507	457	358	299	615	486	678	717
Parameterized eastern waves power (W/m/h)	6,09E+03	9,23E+03	6,91E+03	5,05E+03	3,91E+03	5,11E+03	4,18E+03	7,55E+03
Parameterized eastern waves power proportion (%)	61	56	69	54	92	95	64	57
Cumulative western waves power (W/m)	3,56E+06	1,86E+06	5,59E+06	5,90E+06	2,73E+05	6,28E+04	2,49E+06	4,15E+06
Cumulative western waves power proportion (%)	54	31	69	80	10	2	47	43
Number of hours of western occurrence (h)	920	259	1787	1379	821	233	1071	717
Parameterized western waves power (W/m/h)	3,87E+03	7,17E+03	3,13E+03	4,28E+03	3,32E+02	2,69E+02	2,33E+03	5,78E+03
Parameterized western waves power proportion (%)	39	44	31	46	8	5	36	43

Date	15/01/2017 to 02/04/2017	02/04/2017 to 11/04/2017	11/07/2017 to 23/08/2017	23/08/2017 to 24/09/2017	24/09/2017 to 08/11/2017	08/11/2017 to 20/01/2018	20/01/2018 to 21/03/2018	21/03/2018 to 02/05/2018
Cumulative wave power in total (W/m)	1,07E+07	1,47E+07	9,01E+05	4,29E+05	3,32E+06	4,70E+06	2,30E+07	4,65E+06
Number of hours in total (h)	1823	2395	1029	767	1076	1724	1426	1005
Parameterized wave power in total (W/m/h)	1,26E+04	1,23E+04	1,86E+03	1,22E+03	4,79E+03	5,39E+03	2,56E+04	1,33E+04
Cumulative eastern waves power (W/m)	5,09E+06	1,32E+07	7,71E+05	2,56E+05	3,04E+06	1,63E+06	2,23E+06	2,11E+06
Cumulative eastern waves power proportion (%)	48	89	86	60	92	35	10	45
Number of hours of eastern occurrence (h)	647	1198	475	304	812	827	356	209
Parameterized eastern waves power (W/m/h)	7,87E+03	1,10E+04	1,62E+03	8,42E+02	3,74E+03	1,97E+03	6,27E+03	1,01E+04
Parameterized eastern waves power proportion (%)	62	89	87	69	78	37	24	76
Cumulative western waves power (W/m)	5,59E+06	1,56E+06	1,29E+05	1,73E+05	2,76E+05	3,07E+06	2,07E+07	2,54E+06
Cumulative western waves power proportion (%)	52	11	14	40	8	65	90	55
Number of hours of western occurrence (h)	1176	1197	554	463	264	897	1070	796
Parameterized western waves power (W/m/h)	4,76E+03	1,31E+03	2,33E+02	3,75E+02	1,05E+03	3,42E+03	1,94E+04	3,19E+03
Parameterized western waves power proportion (%)	38	11	13	31	22	63	76	24

Date	02/05/2018 to 31/07/2018	31/07/2018 to 29/09/2018	29/09/2018 to 28/11/2018	28/11/2018 to 25/01/2019	25/01/2019 to 11/03/2019	11/03/2019 to 22/05/2019	22/05/2019 to 06/07/2019	06/07/2019 to 02/09/2019
Cumulative wave power in total (W/m)	1,50E+06	2,46E+06	7,18E+06	3,31E+06	8,72E+06	9,99E+06	2,49E+06	1,78E+06
Number of hours in total (h)	2147	1437	1435	1377	1079	1725	1078	1391
Parameterized wave power in total (W/m/h)	1,86E+03	3,10E+03	9,42E+03	4,63E+03	1,57E+04	1,18E+04	5,79E+03	2,67E+03
Cumulative eastern waves power (W/m)	5,82E+05	2,26E+06	1,90E+06	2,38E+06	6,32E+06	7,54E+06	1,67E+06	1,08E+06
Cumulative eastern waves power proportion (%)	39	92	26	72	72	75	67	61
Number of hours of eastern occurrence (h)	440	813	541	769	582	836	359	607
Parameterized eastern waves power (W/m/h)	1,32E+03	2,78E+03	3,50E+03	3,10E+03	1,09E+04	9,01E+03	4,64E+03	1,78E+03
Parameterized eastern waves power proportion (%)	71	90	37	67	69	77	80	67
Cumulative western waves power (W/m)	9,14E+05	1,98E+05	5,29E+06	9,31E+05	2,40E+06	2,46E+06	8,27E+05	6,99E+05
Cumulative western waves power proportion (%)	61	8	74	28	28	25	33	39
Number of hours of western occurrence (h)	1707	624	894	608	497	889	719	784
Parameterized western waves power (W/m/h)	5,35E+02	3,18E+02	5,91E+03	1,53E+03	4,82E+03	2,76E+03	1,15E+03	8,91E+02
Parameterized western waves power proportion (%)	29	10	63	33	31	23	20	33

Date	02/09/2019 to 16/11/2019	16/11/2019 to 12/01/2020	12/01/2020 to 27/03/2020	27/03/2020 to 10/06/2020	10/06/2020 to 25/07/2020	25/07/2020 to 21/09/2020
Cumulative wave power in total (W/m)	3,49E+06	1,10E+07	6,79E+06	1,00E+07	2,34E+06	3,38E+06
Number of hours in total (h)	1787	1343	1798	1781	1066	1377
Parameterized wave power in total (W/m/h)	4,17E+03	1,51E+04	7,43E+03	1,18E+04	4,41E+03	4,88E+03
Cumulative eastern waves power (W/m)	1,47E+06	1,88E+06	4,91E+06	4,85E+06	1,74E+06	2,02E+06
Cumulative eastern waves power proportion (%)	42	17	72	48	74	60
Number of hours of eastern occurrence (h)	593	568	937	684	529	715
Parameterized eastern waves power (W/m/h)	2,48E+03	3,31E+03	5,24E+03	7,09E+03	3,28E+03	2,82E+03
Parameterized eastern waves power proportion (%)	59	22	71	60	74	58
Cumulative western waves power (W/m)	2,02E+06	9,12E+06	1,88E+06	5,18E+06	6,08E+05	1,36E+06
Cumulative western waves power proportion (%)	58	83	28	52	26	40
Number of hours of western occurrence (h)	1194	775	861	1097	537	662
Parameterized western waves power (W/m/h)	1,69E+03	1,18E+04	2,19E+03	4,72E+03	1,13E+03	2,06E+03
Parameterized western waves power proportion (%)	41	78	29	40	26	42

Appendix 8 - Table of the cumulative and parameterized wave powers computed for the selected periods from wave climate at SIMAR point 5024022 between September 2015 and September 2020

Date	Period I	Period II	Period III	Period J	Period S	Period IV	Period V
Cumulative wave power in total (W/m)	2,82E+07	2,01E+07	3,47E+07	2,30E+07	4,65E+06	3,32E+07	4,13E+07
Number of hours in total (h)	5966	5338	8814	1426	1005	9200	11621
Parameterized wave power in total (W/m/h)	1,14E+04	7,37E+03	6,36E+03	2,56E+04	1,33E+04	7,74E+03	7,03E+03
Cumulative eastern waves power (W/m)	1,13E+07	1,31E+07	2,39E+07	2,23E+06	2,11E+06	2,10E+07	1,96E+07
Cumulative eastern waves power proportion (%)	40	65	69	10	45	63	47
Number of hours of eastern occurrence (h)	1621	2496	4263	356	209	3981	4992
Parameterized eastern waves power (W/m/h)	6820	5187	4505	6268	10106	5096	3831
Parameterized eastern waves power proportion (%)	60	70	71	24	76	66	54
Cumulative western waves power (W/m)	1,69E+07	6,98E+06	1,08E+07	2,07E+07	2,54E+06	1,22E+07	2,17E+07
Cumulative western waves power proportion (%)	60	35	31	90	55	37	53
Number of hours of western occurrence (h)	4345	2842	4551	1070	796	5219	6629
Parameterized western waves power (W/m/h)	4,61E+03	2,18E+03	1,86E+03	1,94E+04	3,19E+03	2,65E+03	3,20E+03
Parameterized western waves power (%)	40	30	29	76	24	34	46

Appendix 9 - Table of the basic statistics of the wave parameters computed between the selected images from wave climate at SIMAR point 5024022 between 2015 and 2020

Date	Mean	Maximum	Minimum
Significant wave height (m)	0,60	5,12	0,02
Spectral peak period (s)	6,23	25,97	1,80
Mean wave direction at peak frequency (°)	195	360	0
Wave power (W/m)	4,08E+03	2,87E+05	4,02
Cumulative wave power (W/m)	6,17E+06	3,39E+07	3,19E+05
Parameterized wave power (W/m/h)	8,50E+03	3,04E+04	1,08E+03
Eastern significant wave height (m)	0,73	3,99	0,02
Eastern spectral peak period (s)	5,78	23,61	1,80
Eastern mean wave direction at peak frequency (°)	123	179	0,00
Wave power (W/m)	5,14E+03	1,60E+05	4,16
Cumulative eastern waves power (W/m)	3,11E+06	1,32E+07	2,56E+05
Parameterized eastern waves power (W/m/h)	5,09E+03	1,10E+04	8,42E+02
Western significant wave height (m)	0,51	5,12	0,02
Western spectral peak period (s)	6,53	25,97	1,80
Western mean wave direction at peak frequency (°)	244	360	181,00
Wave power (W/m)	3,34E+03	2,87E+05	4,02
Cumulative western waves power (W/m)	3,06E+06	2,07E+07	6,28E+04
Parameterized western waves power (W/m/h)	3,41E+03	1,94E+04	2,33E+02

Appendix 10 - Linear Wave Theory equations and wave power computation

To calculate the wave power using the available parameters the following development of the equations of the Linear Wave Theory depicted by Holmes (2001) was performed. Here, P is the mean power transmitted per unit width of crest (W/m), ρ is the fluid density (about 1025 kg/m^3), g is the gravitational acceleration (about 9.81 m/s²), H is the wave height (m), Cg is the wave group velocity (m/s), n is the refractive index, C is the wave phase velocity, d is the water depth (m), L is the wave length (m) and T is the wave period (s).

$$P = \frac{\rho g H^2}{8} \times Cg$$

$$\leftrightarrow P = \frac{\rho g H^2}{8} \times n \times C$$

$$\leftrightarrow P = \frac{\rho g H^2}{8} \times \frac{1}{2}\left[1 + \frac{\frac{4\pi d}{L}}{sinh\frac{4\pi d}{L}}\right] \times \frac{L}{T}$$

In deep water $n \approx \frac{1}{2}$ and $L \approx \frac{gT^2}{2\pi} \approx 1.56T^2$ so,

$$P = \frac{\rho g H^2}{8} \times \frac{1}{2} \times \frac{1.56T^2}{T}$$

$$\leftrightarrow P = \frac{\rho g H^2}{8} \times \frac{1.56T}{2}$$

$$\leftrightarrow P = \frac{1.56\rho g H^2 T}{16}$$